SISSA **ISAS**

SCUOLA INTERNAZIONALE SUPERIORE DI STUDI AVANZATI
INTERNATIONAL SCHOOL FOR ADVANCED STUDIES

Low–intermediate luminosity AGNs: from their X-ray emission to their SMBHs

Thesis submitted for the degree of
Doctor Philosophiæ

CANDIDATE:
Lucia Ballo

SUPERVISORS:
Prof. Stefano Cristiani
Prof. Luigi Danese
Prof. Annalisa Celotti

October 2006

Presentation of this thesis

The paradigm of the coevolution between Active Galactic Nuclei (AGNs) and their host galaxies is becoming well assessed in modern astrophysics. Observational results collected in the last years on two of the most challenging topics, galaxy formation and evolution on one hand and the cosmic accretion history of supermassive black holes on the other hand, firmly assess a close link between supermassive black holes and the spheroidal component of their host galaxies, implying probably a lockstep evolution along the cosmic time. Stimulated by this growing body of observations, theoreticians are tuning more and more complete and sophisticated models. The emerging picture is a complex one, following however the simple prescriptions of a cold dark matter hierarchical model of Universe. Events of major mergers, predicted to assemble early protogalaxies, might be seen as triggers of both intense episodes of star formation and gas inflow towards the central regions (fueling supermassive black holes). In turn, the feedback from supermassive black holes is able to act as a mechanism to regulate star formation.

This is a coherent scenario, that however needs to be confirmed. Several questions are still open. How do the emission properties of AGNs (in particular the accretion mechanism) evolve? What are the physical mechanisms that regulate the evolution of both galaxies and black holes in their center? What are the typical timescales on which they are acting? What is the evolutionary link between high–redshift powerful quasars and low–luminosity nearby AGNs?

Important hints to better understand how the AGNs evolve come from the study of the cosmic X-ray background (XRB). Deep X-ray surveys demontrates that AGNs in the intermediate-redshift domain ($z \sim 0.7 - 1$) are the major contributors to the XRB; so this is the range of redshift where an important fraction of the mass accreted. On the other hand, we know that this is also corresponding to the redshift range where the decline in the cosmic star formation rate began. One of the most debated topics concerns the interplay between active accretion and bursts of star formation. Similar mechanisms, probably minor

mergers and interactions, could fuel both the phenomena. This in turns is reflected on the possible evolution of the obscuration with cosmic time, if it is associated not (only) to the putative torus surrounding the nucleus, but it is related to starforming episodes.

In the present PhD project we focus on the accretion properties of AGNs at these intermediate redshifts: in Part I we present our estimate of black hole masses and Eddington ratios for a sample of X-ray selected AGNs with spectroscopic or photometric redshift between 0.4 and 1. The redshift range, together with the $2-10$ keV X-ray luminosities spanned ($10^{42} \lesssim L_{\rm X} \lesssim 4\times10^{43}$ ergs s^{-1}), allows us to study a significant subsample of the main contributors to the $2-10$ keV X-ray background. Nuclear and bulge optical magnitudes in four bands have been measured via a two–dimensional decomposition. We estimated the mass of the central object using the black hole mass vs. R-band bulge luminosity relation, while the intrinsic (*i.e.*, de-absorbed) nuclear X-ray emission coupled with the nuclear optical magnitudes are used to derive the bolometric luminosity of the AGN. From this analysis we find that in our sample, *(a)* the X-ray–to–optical spectral indices are larger than in optically selected QSOs: $\langle\alpha_{\rm ox}\rangle \sim -1.1$ (as expected due to the X-ray selection); *(b)* the X-ray bolometric corrections are generally small, with a median value $k_{\rm X} \simeq 12$, suggesting a decrease with the nuclear luminosity; *(c)* the Eddington ratios are rather low, about a factor of 10 below the values found at higher redshift and luminosity; *(d)* the central black holes have rather large masses, $10^6 \lesssim M_{\rm BH} \lesssim 3\times10^8\ M_\odot$; we observe a scarcity of black holes with mass $M_{\rm BH} \leq 10^6\ M_\odot$ accreting near the Eddington limit: this result could be ascribed to a decline in their number density, or it could suggest a substantial accretion at higher redshift ($z \gtrsim 1$) also for these smaller black holes.

Our findings on black hole masses, nuclear bolometric luminosities and Eddington ratios indicate that this sample of X-ray selected low–luminosity AGNs is made up of already formed objects, showing a renewal of low–level activity in a gas–poor environment.

In Part II we consider individual sources with luminosity similar to that of the sample of Part I and we perform an in-depth study to better understand the mechanisms powering the AGN during a re-ignition phase and the connection with star formation activity, the previously outlined topics.

First we performed a detailed study of the X-ray emission of the merging system Arp 299, in which there is evidence for the concomitant presence of starburst activity and AGN. This local, peculiar object with strong IR emission is in the above framework an optimal test case for a detailed study on the effects driven by interaction and inflowing of gas during merging phenomena. The analysis of hard X-ray high-resolution observations

allow us to have a completely new vision of Arp 299, a system composed by two distinct galaxies. Unlike the results obtained in all other energy bands, with *Beppo*SAX first and then with *Chandra* and XMM-*Newton* we were able to clearly uncover the presence of an obscured powerful AGN in the merging system, identifying the galaxy hosting the active nucleus. At the same time, the analysis of the XMM-*Newton* data revealed a strong He-like Fe Kα line emission also in the second galaxy. The quality of the analysed data is insufficient to clarify if this feature has a thermal origin or if it is indicative of the presence of a second AGN.

Finally, we use X-ray high resolution spectroscopy as a way to study the physical processes occurring just near the AGN engine, a different tool but as fundamental as the previous ones. In this case, we use the fluorescent line of Fe Kα, the most prominent feature in the X-ray spectrum, as an available direct probe of the inner accretion disk and central black hole, down to a few gravitational radii. This approach is used to study the X-ray observations of AX J0447-0627, an optical type 1 AGN showing in its X-ray spectrum a complex structure in the $4 - 8$ keV rest frame energy range with a very high observed equivalent width, ~ 2 keV. Being the accretion disk the most probable explanation for its origin, this feature allows to put firm constraints to the physics of the disk itself.

The XMM-*Newton* observations of AX J0447-0627 revealed the presence of a bright and prominent set of lines in the $4 - 8$ keV rest frame energy range. This result resolved the contrast between optical classification (AX J0447-0627 is a type 1 AGN) and hard X-ray colors, which are due to unresolved spectral features rather than to absorption effects. This is a strong caveat to confront with in statistical studies based on coarser indicators as the hardness ratios. The present XMM-*Newton* data could be explained with a physical model comprising a power law continuum, a narrow Fe Kα line from neutral material and a He-like Fe Kα relativistic line from a ionized accretion disk, though we cannot exclude the possibility of two relativistic emission lines (Fe Kα and Fe Kβ) and no narrow component. From a statistical point of view a phenomenological model involving the presence of five narrow emission lines produced by a medium far away from the central source is adequate to describe the X-ray spectrum of AX J0447-0627; however, for two of these emission lines there are no clear associations with well known and expected elements.

Table of Contents

List of Figures

List of Tables

Citations to Previously Published Works

Part of the contents of this thesis is already appeared in the following papers:

Published:

- *The XMM-*Newton *view of the relativistic spectral features in AX J0447-0627*
  R. Della Ceca, **L. Ballo**, V. Braito, T. Maccacaro, 2005, ApJ, 627, 706
- *Arp 299: a second merging system with two active nuclei?*
  L. Ballo, V. Braito, R. Della Ceca, L. Maraschi, F. Tavecchio, M. Dadina, 2004, ApJ, 600, 634

Submitted:

- *Black Hole Masses and Eddington Ratios of AGNs at* $0.4 < z < 1$*. Evidence of retriggering for significant contributors of the XRB*
  L. Ballo, S. Cristiani, G. Fasano, F. Fontanot, P. Monaco, M. Nonino, E. Pignatelli, P. Tozzi, E. Vanzella, A. Fontana, E. Giallongo, A. Grazian & L. Danese, ApJ, submitted

INTRODUCTION

1 AGN. Overview

Active Galactic Nuclei (AGNs) are among the most powerful sources of energy in the Universe. Although the objects grouped under this name present a variety of specific characteristics (reflected in a rather complex taxonomy), they are connected by the very large luminosity produced (up to 10^{48} ergs s^{-1} in bolometric, see, *e.g.*, Maraschi & Tavecchio 2003, corresponding to 1000 times the luminosity of a normal galaxy) in a very small volume (even the nearest AGNs are unresolved by diffraction-limited optics of the *Hubble Space Telescope* - *HST*). Moreover, they can be very luminous over the whole electromagnetic spectrum, from the radio to the X-ray and also the γ–ray band. Most of them show large amplitude variability on different timescales, even as short as few days or hours, decreasing to tens of seconds in X-rays.

Taking into account the observed variability, the causality relation implies that the region where most of their bolometric luminosity is produced is extremely compact, with a size of the order of light days or even less ($R \sim 10^{13} - 10^{16}$ cm). These properties on the whole strongly suggest that physical processes other than nuclear fusion powering stars are in action in these sources. The only mechanism efficient enough to explain the observational properties of AGNs is accretion of matter onto a compact object; to produce the observed luminosities, its mass must be of the order of $10^6 - 10^9\ M_\odot$ (to ensure that the Eddington luminosity[1] is higher than the bolometric one). This range of masses excludes a neutron star as accreting object; to obtain the luminosities typically observed, the presence of a *central supermassive black hole* seems to be required (Lynden Bell 1969; Rees et al. 1982; Rees 1984).

In this view, the black hole accretes matter from the inner region of the host

[1]Defined as the luminosity a body should have to balance the force generated by radiation pressure and the gravitational force: $L_{\rm Edd} = 1.3 \times 10^{38} M_{\rm BH}/[M_\odot]$ ergs s^{-1}; for higher luminosities, radiation pressure would prevent spherical accretion.

galaxy; because the infalling matter possesses angular momentum, the flow is organized in a disk structure (the so-called *accretion disk*) where the matter pulled toward the black hole loses angular momentum through viscous or turbulent torques. Its gravitational energy is then converted into radiation; the energy that has to be dissipated to reach the disk inner boundary is the maximum energy released by the accretion disk. The properties of the accretion disk could be described at the first order assuming the standard geometrically thin, optically thick disk proposed by Shakura & Sunyaev (1973): the total emission, extended from the optical to the X-ray band, is a convolution of blackbody spectra with different temperatures, emitted at different radii. The value of the maximum temperature in the disk depends on the black hole mass ($T_{\max} \propto M_{\rm BH}^{-1/4}$); for a black hole with mass of $\sim 10^8\ M_\odot$ the peak of the emission is in the UltraViolet (UV) band. To summarize, there is little doubt that all AGNs are very compact, non-stellar, and quite massive objects.

Despite these common features and basically simple origin for the primary energetic output, the Spectral Energy Distributions (SEDs) of AGNs are extremely complex, and a wide collection of different observational features has been pointed out. Depending on their spectral properties, their luminosity, and the selection criteria, AGNs have been classified in a large number of classes and subclasses. The two most important classification criteria are based on the characteristics of the optical emission lines and the importance of the radio emission.

- Historically, the first important division is made on the basis of the relative importance of the radio emission with respect to the optical one. Kellermann et al. (1989) found that the radio–to–optical ratio of AGNs, defined as $R = F_{5\,GHz}/F_{B\text{-band}}$, has a bimodal distribution, with two peaks at $R \sim 0.1-1$ and $R \sim 100-1000$ (but see for a different view, *e.g.*, Cirasuolo et al. 2003). AGNs populating these two peaks are called *radio-quiet*[2] and *radio-loud*, respectively; the boundary line is posed at $R = 10$. The radio-loud represent only $10\%-20\%$ of the AGN population; in most of these sources, radio observations have revealed directed outflows on scale from 10^{17} cm to several times 10^{24} cm, often with apparent superluminal velocities. The continuum from the InfraRed (IR) to the optical band of radio-loud and radio-quiet AGNs is very similar (*e.g.*, Elvis et al. 1986; Sanders et al. 1989; Francis et al. 1993), suggesting that the two classes have similar thermal components. The whole SED of radio-loud sources is flatter, and basically could be described as combination of a radio-quiet SED and

[2]Historically, the class of radio-quiet AGNs was divided in *quasars* and *Seyfert galaxies* depending on having nuclear luminosity larger or smaller than that of the host galaxy.

a non-thermal component extendend from radio to γ–ray (see Fig. 1). For a special class of radio-loud AGNs, known as *blazars*, this non-thermal radiation dominates the observed continuum, showing (in the ν vs νF_ν plane) a typical "double humped" shape (*e.g.*, Sambruna et al. 1996) which is characterized by an extreme variability, in particular at higher energies.

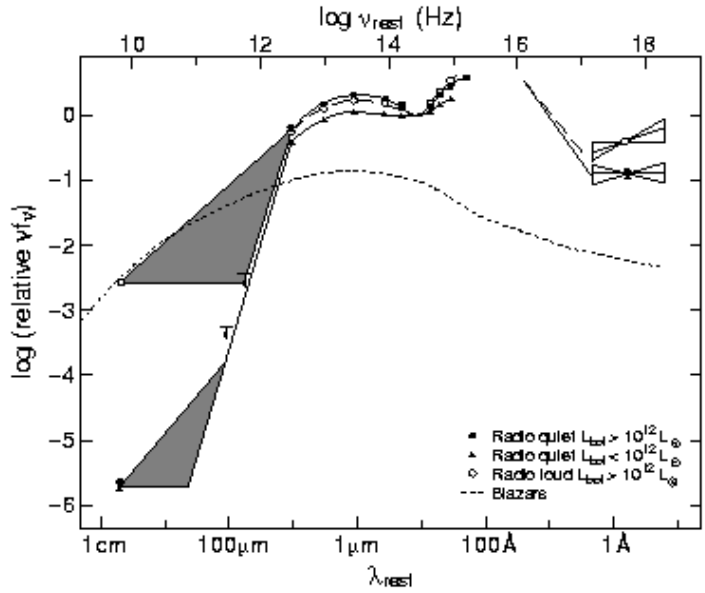

Figure 1 Average continuum distribution of radio-quiet and radio-loud QSOs from the sample of Sanders et al. (1989). Each data point represents the mean over the corresponding sample. The dashed regions in the radio band mark the spread of the radio spectral indexes for each sample.

- Two principal systems of optical emission lines can be identified in the spectra of AGNs (for a general review see, *e.g.*, Netzer 1990). Broad emission lines (mainly Lyα, [Mg II] and C IV), with typical Full Width at Half Maximum[3] FWHM $\gtrsim$ 2000 km s^{-1}, and variable (on time scale of days to weeks to months, depending on the ionization state; see the review by Peterson 1997) indicate the presence of gas characterized by high speed. The second system is composed by narrow (FWHM $\lesssim$ 1500 km s^{-1}) and time-constant lines. The application of photoionization models (althoughit is well known that they are far too simple) could provide constraints on the physical state of the emitting gas. In particular, for the first component the measure of the line

[3]The full width at half maximum of a line is the width measured at half level between the continuum and the peak of the line.

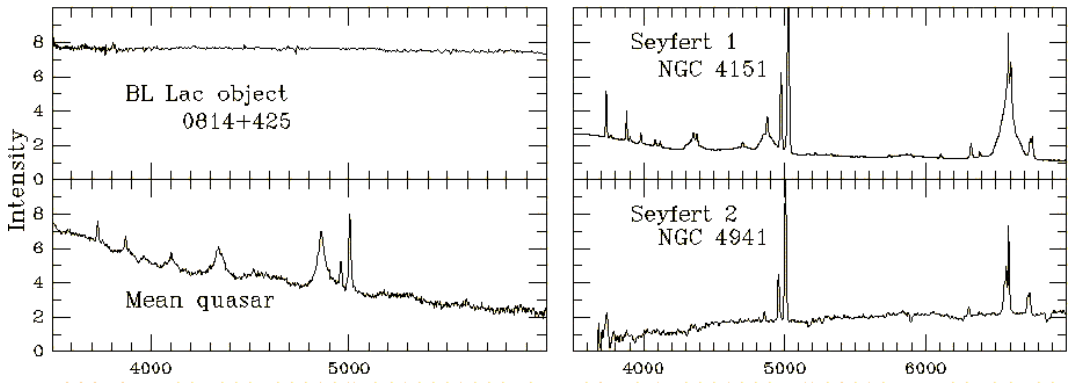

Figure 2 Typical examples of optical spectra for different classes of AGNs according to their optical classification (see text). The "mean quasar" spectrum is a composite from Francis et al. (1991), while the observations for $0814+425$ and NGC 4941 are described in Lawrence et al. (1996) and Keel (1983). Finally, the NGC 4151 spectrum is a composite of data tooken at Kitt Peak National Observatory (from 3300 Å to 4250 Å) and at Lick Observatory ($4250-8000$ Å). Courtesy of B. Keel.

ratios provides a measure of its density usually in the range $n \sim 10^8 - 10^{12}$ cm^{-3}; the variability time scale implies that the typical size for this region of gas is lower than $\sim 2 \times 10^{18}$ cm. In the second component, the presence of forbidden emission lines indicates that they are produced in low density regions, $n \sim 10^3 - 10^6$ cm^{-3}. Objects with broad permitted lines and narrow forbidden lines have been called *type 1 AGNs*; their SED is dominated by the UV excess, or *big blue bump*, while a second important component, the *IR bump*, emerges in the $\sim 1-300$ μm region. Conversely, the optical spectrum of a *type 2 AGN* shows only narrow lines; their continuum emission does not show a strong UV excess, while the IR component is strongly enhanced. In this classification, two special case can be pointed out: the *Broad Absorption Line QSOs* present optical spectra with strong absorption lines; the class of *BLLac objects* (a subclass of the blazars) is characterized by a strong non-thermal continuum and the particular weakness or absence (equivalent width[4] lower than 5 Å) of any optical emission line. To illustrate the optical classification, typical examples of the classes discussed above are shown in Fig. 2.

These two classification criteria, with the bolometric luminosity, allow to organize the variety of classes of AGN in the scheme shown in Table 1 (from Urry & Padovani 1995).

[4]The equivalent width of an emission line is the energy (or wavelength) range over which the continuum radiation contains a flux equal to that contained in the emission line.

Table 1. Classification of AGNs.

		Narrow lines	Broad lines	Non-thermal continuum
RADIO-QUIET	low luminosity	Sy 2 NELG [a]	Sy 1	
	high luminosity	IR quasar	QSO	
RADIO-LOUD	low luminosity FRI	NLRG [b]	BLRG [c]	BLLac
	high luminosity FRII	NLRG [b] BLRG	SSRQ [d]	FSRQ [e]

Note. — Adapted from Urry & Padovani (1995).

[a]Narrow Emission Line X-ray Galaxy

[b]Narrow Line Radio Galaxy

[c]Broad Line Radio Galaxy

[d]Steep Spectrum Radio Quasar

[e]Flat Spectrum Radio Quasar

1.1 Unification schemes

The spectral properties summarized above could be understood assuming the presence of three main components, listed in the following starting from the central region up to kpc scales (as in the scheme - not in scale - shown in Fig 3, *left panel*; see, *e.g.*, Holt et al. 1992).

– The *matter accreting onto a central supermassive black hole* produces the optical-UV blue bump; some broad optical lines may arise in this accretion disk. The same region is responsible for the X-ray emission, likely emitted through Inverse Compton scattering of the same UV photons by a population of extremely hot electrons surrounding the disk. This origin near the central engine makes the X-ray emission extremely useful to study the physics of the black hole-accretion disk system. Due to the interest of this topic for the present work, this point will be discussed more extensively in Part II.

– A *jet*, present in the radio-loud AGNs and often connecting the nucleus with radio lobes observed in radiogalaxies, accounts for their high level of the radio emission, as well as for the non-thermal emission typical of this class. Numerous hints suggest that in most

sources, the jet moves relativistically.

– The primary continuum is reprocessed by gas and matter forming the so-called *Broad Line Region* (BLR), a shell of gas clouds rapidly moving in the potential of the central engine. These gas clouds, photoionized by the nuclear radiation, emit the broad optical emission lines. As noted, the properties of the lines imply densities between 10^8 cm^{-3} and 10^{12} cm^{-3} and a localization of $\sim 0.1 - 1$ pc ($10^{17} - 10^{18}$ cm).

– At larger scales ($\lesssim 100$ pc) the *Narrow Line Region* (NLR) is composed by slow moving clouds of ionized matter producing the narrow optical lines.

As discussed above, despite the number of different properties shown by AGNs, the nuclear engine seems to be the same, *i.e.*, a supermassive black hole accreting gas. A great effort has been devoted to unify the different classes in a unique interpretative scheme. Important achievements of these studies led to the current *type 1/type 2 unification model* (Antonucci 1993) and to the *unification scheme for radio-loud AGNs* (Urry & Padovani 1995). Fig. 3, *right panel*, illustrates how these models work.

The key-element of the unification model is the presence of an anisotropic distribution of matter around the AGN, that causes *different appearance at different angle of view*. According to this model, the difference between type 1 and type 2 AGNs is due to the obscuration of the central region by dust in those sources in which the viewing direction

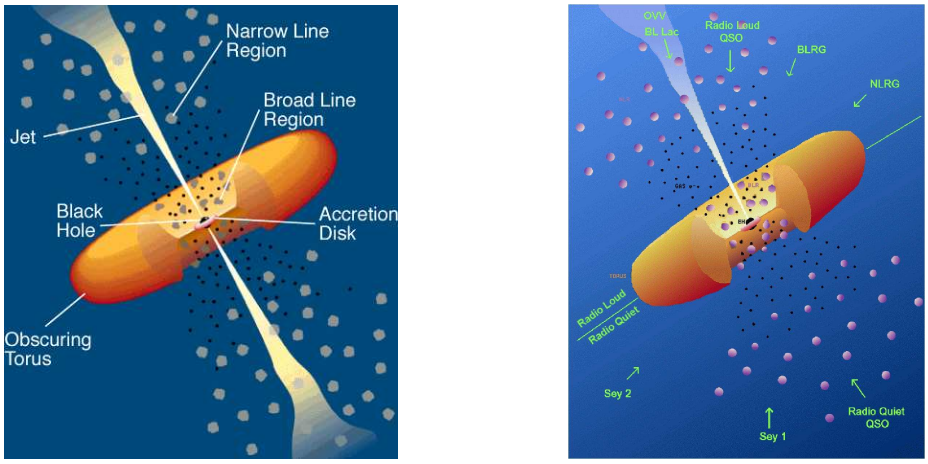

Figure 3 *Left panel*: schematic view of different components of a typical AGN, as discussed in the text. *Right panel*: a sketch showing the summary of AGN classification according to the unified model illustrated in the text and in Table 1. Adapted from Urry & Padovani (1995).

intercepts the torus (or the warped disk). This distribution of matter can be of ~ 1 pc or larger (its size is not well constrained by present data): so, the black hole, the accretion disk and the BLR turn out to be partially covered, while the NLR is outside the torus. When the obscuring torus is oriented face-on, both the nuclear continuum and the lines emitted by the BLR and the NLR are seen, and the object appears as a type 1 AGN. In contrast, when the torus intercepts the line of sight both the central core and the BLR are hidden: the intrinsic continuum is absorbed and reprocessed in the IR band, and the optical spectrum presents the only narrow line region; the object is classified type 2 AGN.

Confirmations of this picture come from spectropolarimetric studies of type 2 AGNs, X-ray observations and studies of the NLR.

- Broad emission lines has been discovered in the polarized spectrum of a number of Seyfert 2 galaxies; these features have been interpreted as scattered nuclear emission by electrons or dust in a medium located above the torus, implying obscuring material along the direct line of sight.
- X-ray observations of a number of type 2 AGNs show the presence of absorbing material with high column densities[5], $N_{\rm H} = 10^{22} - 10^{24}$ cm^{-2}.
- High resolution *HST* images of nearby type 2 galaxies revealed that the NLR is illuminated by an anisotropic radiation field. The conical pattern is a strong indication of the toroidal shape of the absorber.

Concerning radio-loud AGNs, the current unification scheme tries to unify radio galaxies with blazars, assuming that the latter are radio galaxies in which the jet points in a direction very close to the line of sight. Relativistic effects amplify the non-thermal continuum emitted by the matter in the jet, producing all the peculiar characteristics observed in these sources. As discussed in Urry & Padovani (1995), the principal ingredient of the radio-loud unification is then the *intrinsic anisotropy of the emission induced by the relativistic beaming*.

The last step in tracing back all the different phenomenologies observed in the AGNs to a common picture is to unify radio-loud and radio-quiet galaxies. In this, it is important to take into account the ultimate source of the energy, the central black hole. Indeed, according to this framework we expect intrinsic differences between AGNs in terms

[5]The hydrogen equivalent column density is defined as $N_{\rm H} \equiv n_{\rm H} R$, $n_{\rm H}$ being the hydrogen density and R the thickness of the absorber.

of the basic physical parameters regulating the black hole physics: the black hole mass, the accretion rate and the black hole spin (*grand unification scheme*, Blandford et al. 1990). The sketch in Fig. 4 visualizes the basic properties of a superunification scheme for the AGNs. In the past years different models have been proposed assuming that radio-loud objects are able to produce powerful jets because of special (and relatively rare) properties of the central engine, such as a large value of the spin or mass or magnetic fluid strength. Also a difference in the environmental properties of the host galaxy and/or in the power of the jet could play an important role: dense environments would prevent the accelerated matter to escape from the galaxy or even to collimate to form a jet.

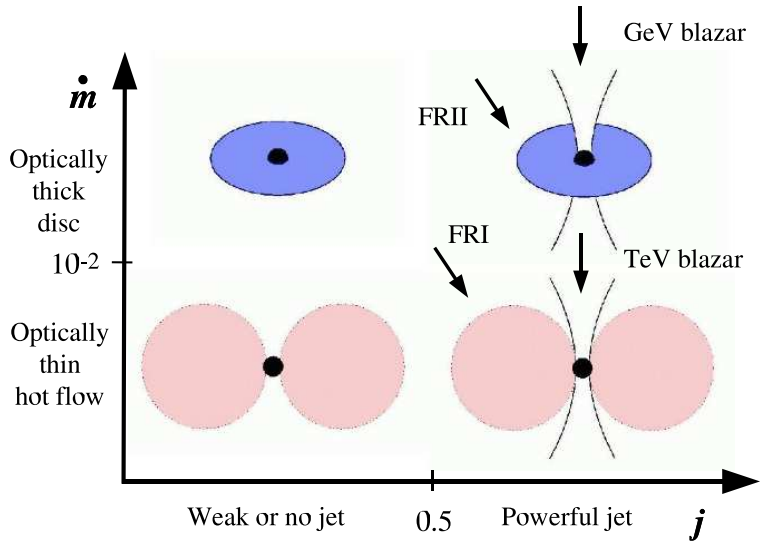

Figure 4 Sketch of the AGN grand unification model, that ascribes the dichotomy radio-loud/radio-quiet to different physical parameters of the black hole/accretion disk system (from Maraschi & Tavecchio 2005).

2 AGNs and their host galaxies. Coevolution

The paradigm that AGNs are powered by mass accretion on a supermassive black hole received strong support from the discovery, in the past years, that massive black holes ($M_{\rm BH} \sim 10^6 - 3 \times 10^9\ M_\odot$) are present in essentially all local galaxies with a substantial spheroidal component (Kormendy & Richstone 1995; Magorrian et al. 1998; Kormendy & Gebhardt 2001). The mass of the central black holes is found to correlate with various properties of the spheroidal component of their host galaxies: luminosity (Kormendy &

Richstone 1995; Magorrian et al. 1998; McLure & Dunlop 2002; Marconi & Hunt 2003), mass (Häring & Rix 2004), velocity dispersion (in turn correlated to the bulge magnitude via the Faber-Jackson relation; Ferrarese & Merritt 2000; Gebhardt et al. 2000; Merritt & Ferrarese 2001; Tremaine et al. 2002), light concentration (Graham et al. 2001), and halo circular velocity (Ferrarese 2002).

This set of relations opens a window over the very same accretion mechanism: reconstructing the history of the relation between $M_{\rm BH}$ and $M_{\rm bulge}$ is a benchmark to follow the accretion history over the cosmic time. The bottom line is quite simple: if the growth of supermassive black holes and host galaxies occurs in lockstep, then the ratio of their masses must be independent of redshift. However, both direct black hole mass determinations and spatially resolved kinematical studies are feasible only for local systems. The former could be inferred from secondary estimators, based on empirical relations between the mass (or related quantities) and other AGN properties easily measurable (*e.g.*, the relation between continuum luminosity and size of the BLR, the latter being related to $M_{\rm BH}$ through the virial relation; see Kaspi et al. 2000; Peterson et al. 2000; Vestergaard 2002). The agreement between widths measured from stellar absorption-line kinematics and widths of the [O III]$\lambda\lambda 5007, 4959$ Å lines of AGNs suggests the possibility of using the latter when the stellar velocity dispersion is not direct measurable (Nelson 2000).

There is evidence that, although there seems to be a unique local relation, supermassive black holes at different evolutionary stages might reach this relation in different ways. Semi-analytic cosmological models (*e.g.*, Di Matteo et al. 2003) suggest that the dependence of black hole mass on velocity dispersion is fully established only at low redshift, $z \lesssim 2$. Rix et al. (1999) found that quasars at $z \sim 2$ show a higher ratio between nuclear luminosity and stellar mass than that found at $z = 0$. A possible interpretation would then be that luminous black holes at high redshift may grow faster than their associated host galaxies.

On the other hand, we must confront with a degeneracy in the interpretation of observations: another possibility is that the relation itself does not vary with redshift, but the Eddington ratio is higher in high redshift objects ($\lambda = 1$) as opposed to lower values for the local counterparts ($\lambda = 0.01 \div 0.1$; see, *e.g.*, Woo & Urry 2002; Akiyama 2005).

Shields et al. (2003) estimated the black hole masses for a sample of QSO from the width of the Hβ emission line and nuclear continuum luminosity at 5100 Å (Kaspi et al. 2000), and the stellar velocity dispersion of bulge from width of the narrow [O III] lines, to study the $M_{\rm BH}$-σ relation out to redshift $z \approx 3$. They found that the relationship for

radio-quiet QSO does not depend on redshift and is fully consistent with that derived locally by Tremaine et al. (2002). This is an important keystone for the origin of this relation and supports the view of growth in lockstep for both supermassive black holes and stellar bulge of the host galaxies. Recently, Woo et al. (2006) perform a similar study on a sample of Seyfert 1 galaxies at $z \sim 0.3$, finding that the correlation between black hole mass (estimated as in Shields et al. 2003) and bulge velocity dispersion (measured from stellar absorpion lines) could be subject to a cosmic evolution. Host R-band luminosity observations reported by Peng et al. (2006) imply evolution occurring at $z > 1$ (with black holes becoming over-massive relative to their hosts), while, once allowing for passive evolution of the stellar population, the $M_{\rm BH}$–M_R relations at $z < 1$ are compatible with the local relation.

Regarding the evolution of these correlations, Hopkins et al. (2006b) outlined the importance of having constraints independent of systematics and selection effects in host measurements. Requiring a total mass density in the most massive black holes lower at a given redshift z than today, they found an upper limit to the degree of evolution in the $M_{\rm BH}$-$M_{\rm bulge}$ ratio consistent with passive evolution at all redshift.

Despite these still unresolved issues, the relevance of the link between black hole mass and bulge properties is twofold: on one side, it offers a powerful observational approach to derive black hole masses, otherwise scarcely accessible to direct measurements. On the other hand, it raises what is now one of the most hot topic in AGN studies, namely the coevolution of black holes and host galaxies. Indeed, leaving aside the somewhat hot debate on the exact analytic form of the relationships found (Ferrarese & Ford 2005; see also the discussion in Sect. I 4.1), the existence of a correlation between host galaxy and black hole masses points out that the formation of supermassive black holes and of the host galaxy spheroidal components, and ultimately their fate, must be tightly related.

Currently, a very fashionable theory is that the main culprit might be found in the feedback from supermassive black holes, able to regulate the bulge growth (see, *e.g.*, Mathur & Grupe 2004 for references). The effects of the QSO emission on the surrounding gas could limit the quantity of mass accreted: the accretion is slowed down, or even stopped, when the gas binding energy is balanced by the energy stored in a dynamical time by the nuclear sources in the gas (Silk & Rees 1998). As a byproduct, taking into account the effects of the mutual feedback between galaxies and quasars in the first stage of their evolution might help to overcome some difficulties of the standard scenario for galaxy evolution in explaining observational data (Granato et al. 2001).

The physical mechanism governing the interaction between the active nucleus and

the host galaxy remains obscure. An important goal to study and understand the coevolution of galaxy and nuclear black hole lies in our ability to reconstruct the detailed cosmic history of supermassive black hole accretion (Silk & Rees 1998; Granato et al. 2001, 2004; Hopkins et al. 2005). As an ultimate task, one should match the total black hole mass accreted with the integral of the local mass function of the quiescent black holes (see, *e.g.*, Salucci et al. 1999; Yu & Tremaine 2002; Marconi et al. 2004; Shankar et al. 2004).

An important question is whether the accreted mass is on average falling onto supermassive black holes already supplied with very large mass ($\Delta M_{\rm acc}/M_{\rm BH} \ll 1$), or the accretion is occurring onto smaller supermassive black holes. The first regime corresponds to Eddington ratios $\lambda = L_{\rm bol}/L_{\rm Edd} \ll 1$ and can be associated to reactivation of pre-existing black holes, while the latter corresponds to $\lambda \lesssim 1$ and is associated with the main episode of growth of lower mass black holes. Understanding the accretion powering the AGNs that constitute the bulk of the X-ray background (see Sect. 2.1) would provide important constraints on this field: as pointed out by Marconi et al. (2004) and Shankar et al. (2004), the mass accreted onto the central supermassive black holes of these $z < 1$ AGNs turns out to be $\sim 30\%$ of the total mass density accreted at any redshift.

Vittorini et al. (2005) investigated the accretion history of active galaxies. Their model is based on recurrent supply-limited accretion phenomena, stochastical in nature, but with a gradual decrease of the energetic output. Consequences of their model are Eddington ratios declining and widely scattered with redshift, and only a weak evolution in the $M_{\rm BH}$-σ relation. In new-generation numerical simulations, merger events at high redshift, predicted by hierarchical models of universe, are a natural trigger for both intense bursts of star formation and the onset of consistent gas inflows (see, *e.g.*, Di Matteo et al. 2003, 2005). The very first phases of a massive galactic black hole are thus likely be as a deeply buried object obscured at visual wavelengths and rapidly growing at the same time of a rapid star formation (see, *e.g.*, Granato et al. 2004; Hopkins et al. 2006a).

A study of accretion properties as the one described in Sect. I (starting from the above mentioned relation, namely the $M_{\rm BH}$-$L_{\rm bulge}$ one with the assumption of no evolution) could add a new observational piece to this puzzle.

2.1 The X-ray Background

Important information on the evolution of AGNs (and of their host galaxy, taking into account the paradigm of coevolution discussed above) and on the presence (and the evolution) of obscured AGNs comes from the study of the Cosmic X-ray Background

(hereafter XRB). The XRB, discovered in the early '60s (Giacconi et al. 1962), has been object of extensive studies to understand its origin. The spectrum of the XRB is well studied in a wide energetic range; as shown in Fig. 5, where its spectral energy distribution from 0.25 keV to 400 keV is reported, it is characterized by a "bell" shape, with a peak at about $30 - 40$ keV. The origin of the bulk of the XRB (*i.e.*, discrete sources or thermal

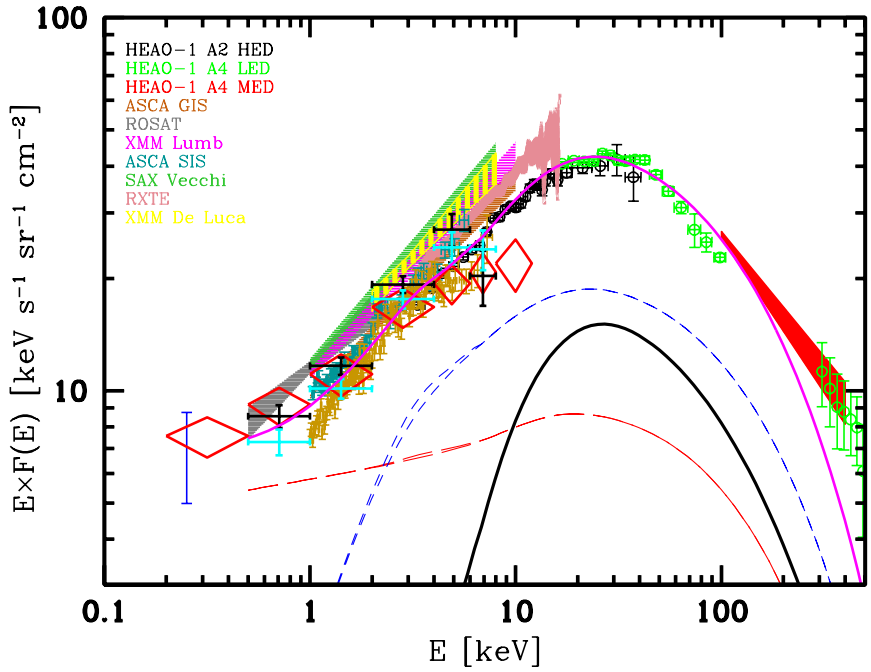

Figure 5 Spectrum of the XRB from 0.25 keV to 400 keV and predicted AGN contribution (magenta solide line which includes also galaxy clusters; from Comastri et al. 2006). Different colors correspond to measurements by different missions/instruments, as labelled. The contribution of unobscured (red dashed line), Compton thin (blue thin line) and Compton thick (black line) sources is shown. Red diamonds, cyan crosses and black crosses represent the resolved XRB fractions in different surveys by Worsley et al. (2005): Lockman Hole, CDF-S and CDF-N, respectively.

emission from hot intergalactic gas) has been initially matter of debate. The absence of a strong Compton distortion on the Cosmic Microwave Background spectrum, that was not observed by the COBE satellite (see Mather et al. 1994; Wright et al. 1994), places a strong upper limit to the possibility of a truly diffuse component (less than 3%), ruling out the second hypothesis. On the other hand, the discrete nature of the XRB has been clear

since the deepest observations with *ROSAT*, that resolved $70-80\%$ of the soft component into discrete objects (Hasinger et al. 1998), and found that the sources lie mainly in AGNs at redshifts from 0.1 to 3.5. *ASCA* observations extended the search for sources in the $2-10$ keV band, resolving about 30% of the background mostly into AGNs (Ueda et al. 1998). Observations with *Beppo*SAX have continued these studies.

In spite of the difficulties in the spectral normalization between observations from different instruments (mainly in the best sampled energy range, beyond 10 keV), all the measurements seem to agree in describing the low energy XRB as a power law with a spectral slope of $\Gamma \sim 1.4$. Here and in the following, a power law spectrum will be described with its spectral index α (where $F_\nu \propto \nu^{-\alpha}$) as well as using the photon index Γ, where $\Gamma = \alpha + 1$. The spectral shape typical of the unobscured AGNs that, according to the *ROSAT* surveys, produce the soft XRB, is much steeper than $\Gamma \sim 1.4$. Hence, to explain the flatness observed at low energies in the XRB spectrum (the so-called "spectral paradox", Boldt 1987), the existence of a population of absorbed AGNs producing much of the XRB at energies > 2 keV has been suggested very early (Setti & Woltjer 1989).

With the advent of the deep X-ray surveys performed by XMM-*Newton* and *Chandra* (Brandt et al. 2001; Rosati et al. 2002; Hasinger et al. 2001; see Sect. 3.2), $\sim 90\%$ of the XRB up to 10 keV has been resolved into single sources (see Bauer et al. 2004). In agreement with the main predictions of the synthesis models, these surveys have shown that in this energy range the XRB is due to the integrated emission of different classes of AGNs,

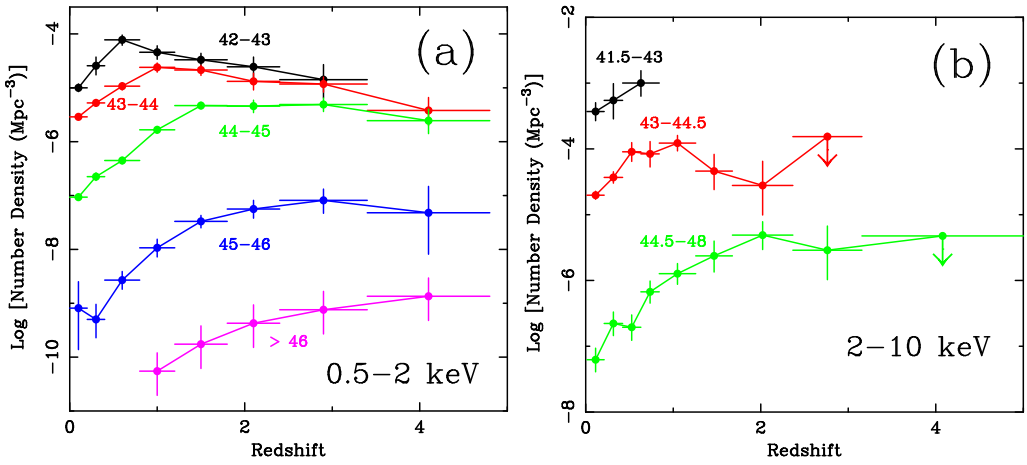

Figure 6 The comoving space density of AGNs selected in the $0.5-2$ keV band [*panel (a)*] and in the $2-10$ keV band [*panel (b)*] as a function of redshift, shown for five and three luminosity ranges (as labelled), respectively. From Brandt & Hasinger (2005; adapted from Ueda et al. 2003).

obscured and unobscured, with an increasing fraction of obscured AGNs towards fainter X-ray fluxes (Rosati et al. 2002; Barger et al. 2002). Their observed redshift distribution peaks at ~ 0.7 (Szokoly et al. 2004), and the major contribution in the interval $0.4 < z < 1$ comes from objects with X-ray luminosities between 3×10^{41} and 10^{43} ergs s^{-1} (Ueda et al. 2003; see Fig. 6).

3 The multiwavelength approach. Instruments, surveys and databases

It is widely accepted that the strength of modern observational campaigns to tackle several astrophysical issues does rest on the multiwavelength approach. Nowadays, several great space-born observatories are fully operating in different energy ranges and allow to get rid of the atmospheric barrier. An unprecedented amount of new data thus is presently within reach. The synoptic view as given by multiwavelength studies is widely used in the present work. Hence, to conclude this introduction we present an overview of all the instruments used, meaning both the exploited databases and the physical observatories and devices used to gather the data.

In Sect. 3.3 we put special emphasis on the technical properties of XMM-*Newton* as the X-ray observatory whose data are analysed in Part II.

3.1 *HST* and the survey GOODS

The Great Observatories Origins Deep Survey (GOODS) was designed to gather the best and deepest multiwavelength data for exploring the distant universe, tracing the mass assembly history of galaxies throughout most of the cosmic history. The main scientific drivers were to study the formation and evolution of galaxies and AGN, to put constraints on the distribution of dark and luminous matter at high redshift, and to determine the cosmological parameters from distant supernovae. These aims were pursued planning the extremely wide spectral coverage described in the following.

In this respect the GOODS survey is really unique; in fact, in addition to deep X-ray and optical images from *Chandra*, XMM-*Newton* and *HST* satellites the survey also exploits extensive follow–up work with ground-based telescopes, extending the sampling of the electromagnetic spectrum of the sources down to the radio wavelength (with completed or on-going surveys).

The survey area is divided in two fields ($10' \times 16'$ each) centered on the *Chandra*

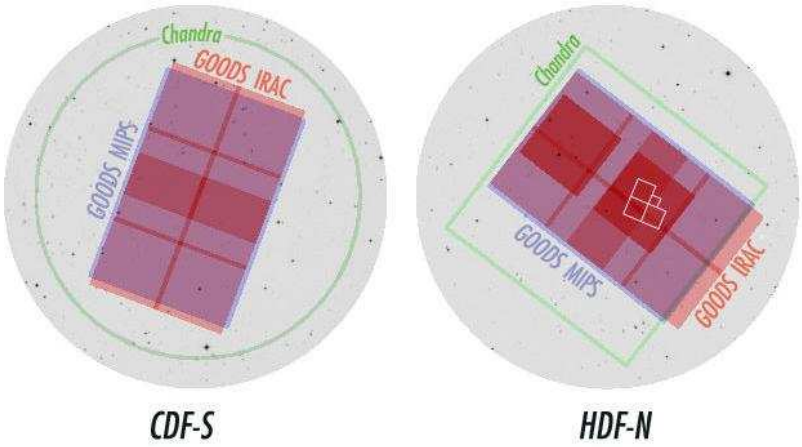

Figure 7 Layout of the GOODS fields. The red regions show the areas covered by *Spitzer* IRAC (3.6 μm to 8.0 μm) observations. The *Spitzer* MIPS 24 μm fields are shown in blue, and closely overlap the IRAC fields. The ultradeep (1 Msec) *Chandra* ACIS fields are schematically outlined in green. The *HST* HDF-N central WFPC2+NICMOS field is shown as a white chevron. From the GOODS site `http://www.stsci.edu/science/goods/`.

Deep Field North and South (hereinafter CDF-N and CDF-S; see also Sect 3.2): these regions have been choosen because they have already been extensively observed in deep extragalactic studies; moreover, observations in both the hemispheres can exploit follow–up with different observatories, providing at the same time a safety check against cosmic variance possibly due to line-of sight clustering effects.

A detailed description of the project can be found in Dickinson et al. (2003); see also Giavalisco et al. (2004). Here we will briefly limit to the features most relevant to the present study.

The project incorporates one of the first *Spitzer* Legacy Program. GOODS has imaged these fields at 3.6 μm, 4.5 μm, 5.8 μm and 8.0 μm with the InfraRed Array Camera (IRAC) onboard *Spitzer*. Fig. 7 illustrates the field coverage of *Spitzer*. For each field, observations have been divided into two epochs, with a mean exposure time per channel per sky pointing of approximately 23 hours per epoch. As a part of the project, a small area in the CDF-N was selected as a target for deeper IRAC observations, with total exposure times of $\sim$ 90 hours. At longer wavelenghts, 10 hours exposures at 24 μm with the Multiband Imaging Photometer for *Spitzer* (MIPS) completed the *Spitzer* participation to the GOODS project. The data release is going on; the observing strategy and the data products from IRAC and MIPS observations will be presented in Dickinson et al. (2006, in preparation)

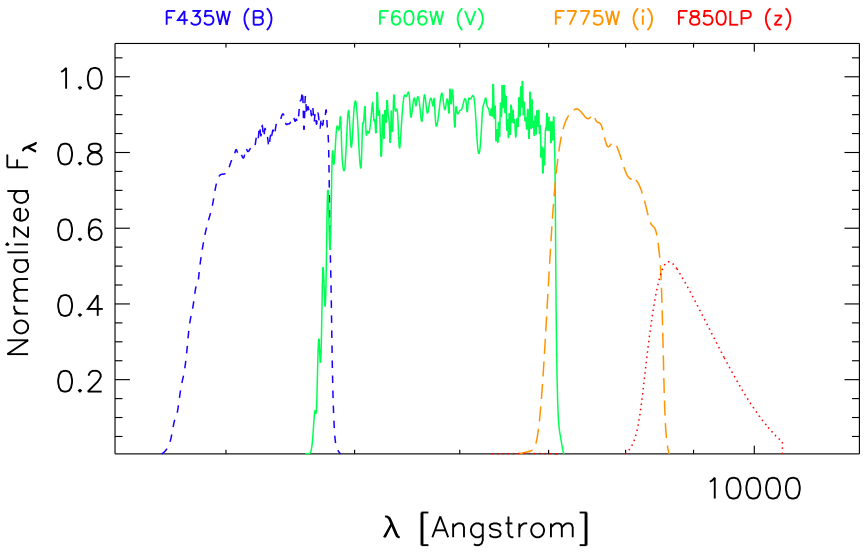

Figure 8 Throughput for the *HST*/ACS filters used in the framework of the GOODS survey.

and Chary et al. (2006, in preparation), respectively.

The GOODS *HST* Tresaury Program gathered images with the Advanced Camera for Surveys (ACS) onboard *HST* in four broad, almost non-overlapping filters, F435W, F606W, F775W and F850LP (hereafter we will refer to these four passbands as B, V, i and z respectively; their wavelength coverage is shown in Fig. 8). The layout of the GOODS/*HST* observations is shown in Fig. 9. The data acquisition is discussed in Giavalisco et al. (2004); briefly, the observations in the V, i and z bands have been carried out in five epochs, each with exposure times of 1050 sec, 1050 sec and 2100 sec, respectively; the complete set of B observations was obtained in the first epoch alone. After the basic reduction and having derived an astrometric solution for all the bands, a multi-drizzling algorithm was applied to the individual exposures taken in each band for each pointing; cosmic-rays were rejected during this step of the data reduction. At the end, the final product is multi-epoch stacked mosaics of the GOODS ACS data in each passband and in both fields of the survey, with a Point Spread Function (PSF) of $0.03''$/pixel.

The ground-based dataset includes new observations, as well as data from public surveys or as part of private projects currently made available to the astronomical community. The GOODS field of the CDF-S has been the target of a deep imaging campaign in the

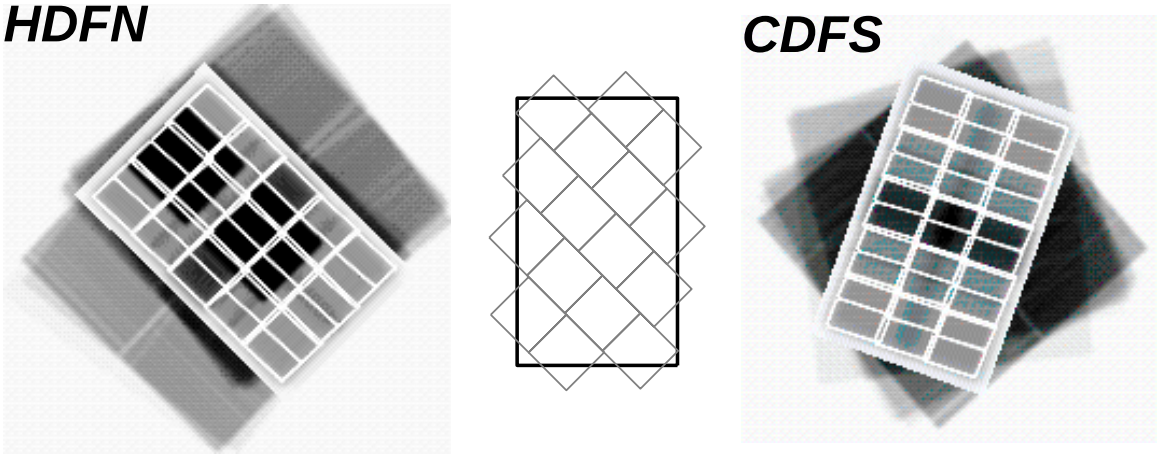

Figure 9 Layout of the GOODS/*HST* observations. The grid of white boxes shows the tiling of *HST*/ACS fields at one telescope orientation, superimposed on the *Chandra* (outer greyscale) and *Spitzer* IRAC (inner greyscale) exposure maps. The central inset schematically shows how the rotated ACS pointings from alternate visits are tiled over the GOODS area. From the GOODS site `http://www.stsci.edu/science/goods/`.

near Infrared (NIR) with the ESO telescopes. A large field ($20' \times 20'$) has been covered with the SOFI instrument at the NTT in the J and Ks bands as part of the Deep Public Survey carried out by the ESO Imaging Survey (EIS) program; the data are described in Vandame et al. (2001). An H-band survey of the CDF-S, encompassing the spatial coverage of the EIS observations, has been carried out with the same instrument; the results are presented in Moy et al. (2003).

The GOODS field is being covered by deeper observations in the same NIR bands with the ISAAC instrument at the VLT. These data have been partially released by ESO and will be used in the present work. The details of the ongoing GOODS program at ESO are given at `http://www.eso.org/science/goods/products.html`.

U-band data were taken with the ESO Wide Field Imager (WFI) at La Silla (Chile), as a part of the EIS public survey (Arnouts et al. 2001), as well as with VLT-VIMOS imager. The WFI images have been obtained in two filters, the so-called U_{35} and U_{38}, with an exposure time of $\sim$ 54 ksec and $\sim$ 75 ksec, respectively. The U-band image of VIMOS is based on a redder filter and has an exposure time of $\sim$ 10 ksec. The coverage with VIMOS of the GOODS field centered on the CDF-S is partial, since the observing program has not been completed yet.

The HK' catalogue of Capak et al. (2004) covers an area of 0.1 square degrees

centered on the CDF-N. The HK' filter covers both the H and K' bands in a single filter; it allows a greater depth but involves some loss of color information. HK' data have been collected using the *QUIRC* camera on the University of Hawaii 2.2m telescope with a $3.6' \times 3.6'$ field of view and with an AB magnitude limit across the field of 22.1 (in a $9' \times 9'$ field around the CDF-N the band reaches a limit of 22.8 mag).

Finally, the high energy view of the two GOODS field is provided by the deep X-ray pointings carried out by the *Chandra* X-ray Observatory before the start of the GOODS project. Archival data from XMM-*Newton* are also available.

In the work presented in the Part I, a morphological and photometric analysis of a sample of X-ray selected AGNs, we will fully exploit the characteristics of the GOODS project. The deep, high resolution optical imaging with large spectral coverage allowed to study the nuclear accretion powering these sources. The availability of observations in the IR and near-UV band allow to safely constrain our results.

3.2 *Chandra* and the *Chandra* Deep Fields

The *Chandra* X-Ray Observatory was launched on 1999 July 23 to be the NASA follow–up mission to the Einstein Observatory. The improvement in the technical capabilities are considerable, both on angular resolution, imaging sensitivity and spectroscopy capability; a good introduction to the observatory can be found in Weisskopf et al. (2002).

Chandra carries a high resolution mirror (consisting of four pairs of nested reflecting surfaces, arranged in the usual Wolter type-1 geometry; see Citterio et al. 1985), with two imaging detectors, the Advanced CCD Imaging Spectrometer (ACIS) and High Resolution Camera (HRC). Each instrument provides both a so-called imaging detector (ACIS-I and HRC-I) and a spectroscopy detector (ACIS-S and HRC-S). The two instruments can also be used in conjunction with two sets of transmission gratings, with the ACIS primarily used with the HETG (High Energy Transmission Gratings, that consists of two separate sets of gratings, optimized for the 0.4 to 5 keV range and the 0.8 to 10 keV range) and the HRC with the LETG (Low Energy Transmission Gratings, optimized for the 0.07 to 2 keV range).

The effective area of the *Chandra* mirror is approximately 800 cm^2 at energies below 2 keV and approximately 400 cm^2 between 2 and 5 keV. The PSF has a Full Width at Half Maximum (FWHM) less than $0.5''$ and a half-power diameter less than $1''$.

The Advanced CCD Imaging Spectrometer (ACIS) is composed of two CCD arrays, one for imaging and the other for grating spectroscopy. Each CCD in each array is tipped

to approximate the relevant focal surface. In conjunction with the High Resolution Mirror Assembly (HRMA), the ACIS imaging array provides simultaneous time-resolved imaging and spectroscopy. With the HETG and the LETG, the ACIS spectroscopic array acquires high resolution (up to $E/\Delta E = 1000$) spectra of point sources. The bare CCD arrays themselves have an intrinsic energy resolution of about $E/\Delta E = 50$ at 6 keV.

The main HRC characteristics include high spatial resolution ($< 0.5''$) and high time resolution (16 μsec) over the entire field of view, low internal background, low sensitivity to cosmic ray induced background, high X-ray quantum efficiency from 0.1 to 10 keV, and modest energy resolution over this spectral band ($0.1-10$ keV and $0.8-6$ keV for HRC-I and HRC-S, respectively). It is used for high resolution imaging, fast timing measurements, and for observations requiring a combination of both. The HRC emphasizes lower energies where the mirror area is largest. It has a large field of view and is useful for imaging large objects (*e.g.*, galaxies, supernova remnants, clusters of galaxies), or large regions of the sky.

In the last years *Chandra* accomplished two very deep ACS-I exposures on two small areas of the sky: the CDF-S (1 Msec covering 0.11 square degree, see Giacconi et al. 2002, Rosati et al. 2002, Alexander et al. 2003); and the CDF-N $0.5-8.0$ keV survey (2 Msec covering 448 square arcminutes centered in the HDF-N; see Alexander et al. 2003). The unusually small amounts of gas and dust within our Galaxy in these directions made these regions suitable for a deep look towards the distant Universe. In Fig. 10 we show a color composite of the adaptively smoothed $0.5-2$ keV, $2-4$ keV and $4-8$ keV CDF-N image (from Alexander et al. 2003).

The excellent imaging quality of *Chandra* allows to make extremely deep exposures without problems introduced by the "confusion effect". This effect refers to the overlapping of images of sources that are seen close to each other in the sky and thus are difficult to resolve individually. Previous X-ray satellites were not able to obtain sufficiently sharp X-ray images and the earlier deep X-ray surveys therefore suffered severely from this effect. Moreover, *Chandra* has much better sensitivity at higher energies, which are less affected by obscuration effects. It can therefore better detect faint sources emitting very energetic X-rays.

The main scientific goal of this survey is to understand the nature and evolution of the elusive sources that make up the XRB (see Sect. 2.1): thanks to the deep exposures, these surveys extend the study of the background to flux levels more than an order of magnitude fainter than achieved in previous surveys in the $0.5-2.0$ keV band and resolve over 90% of the background into a variety of discrete sources. The largest uncertainty in

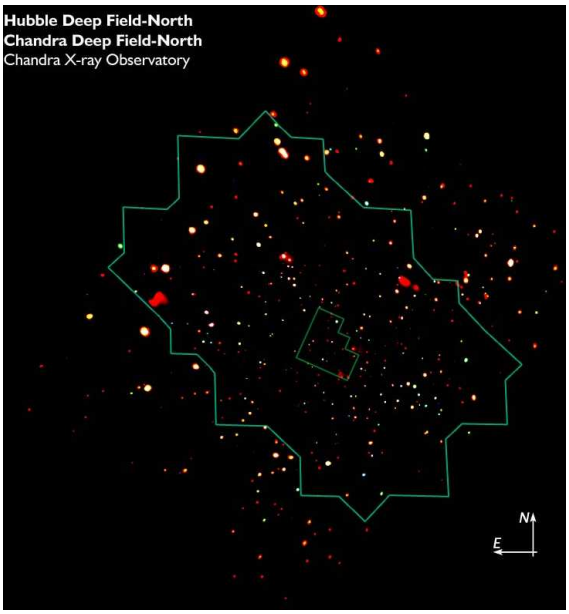

Figure 10 *Chandra* "true color" image of the 2 Msec CDF-N. This image was obtained by combining three energy bands: $0.5-2$ keV (red), $2-4$ keV (green) and $4-8$ keV (blue). The small polygon indicates the HDF-N, while the largest one indicates the area of the GOODS observations (*HST*+*Spitzer*; see Sect. 3.1). Adapted from Alexander et al. (2003).

establishing the fraction currently lies in the knowledge of the total level of the background itself.

After these observations, the two fields have become the target of extensive multiwavelength campaigns, carried out with ground-based and space observatories (see, *e.g.*, the GOODS survey, Sect. 3.1). Afterwards, an extension of the 1 Msec CDF-S survey was carried out (PI N. Brandt; the point source catalogue is presented in Lehmer et al. 2005 and Virani et al. 2006). The Extended CDF-S (E-CDF-S) consists of four *Chandra* ACIS-I pointings and covers approximately 1100 square arcminutes on the sky (~ 0.3 square degree) surrounding the original CDF-S field to a depth of ~ 228 ksec. The planning of the observations was optimized to fill the X-ray luminosity–vs–redshift plane at $z > 1.5$, where the AGN source statistics is still limited.

The follow–up exploits an extended multiwavelength coverage including VLT/Keck spectroscopy, *HST* imaging (within the GEMS, GOODS, and ACS Ultradeep Field projects), intensive ground-based imaging, and *Spitzer* observations. Moreover, the E-CDF-S has been selected as part of the ~ 1 square degree MUltiwavelength Survey by Yale/Chile (MUSYC; Gawiser et al. 2006). This project encompasses four fields of $30' \times 30'$ each, chosen to

exploit existing data and to enable flexible scheduling of observing time during the year. Each field will be imaged from the ground in the optical and near-infrared, and with space-based observatories in the optical (ACS on *HST*), X-rays (*Chandra*, XMM-*Newton*), and mid/far-infrared (*Spitzer*). Follow-up optical spectroscopy will be done mostly with multi-object spectrographs (VIMOS, IMACS, GMOS). The survey fields will be a natural choice for future observations with ALMA. A summary of the project status could be found at `http://www.astro.yale.edu/musyc/publications.html`

3.3 XMM-*Newton*

Launched on December 1999, the European Space Agency (ESA) observatory XMM-*Newton* has on board three Wolter type-1 X-ray telescopes (Citterio et al. 1985), equipped with different detectors, and a 30 cm optical/UV monitor. Three different science instruments are on board XMM-*Newton*. The European Photon Imaging Camera (EPIC) consists of 2 MOS (Metal Oxide Semi-conductor, basically the same cameras but rotated by 90% with respect to each other) and one pn Charge-Coupled Device (CCD) array located at the prime focus of each of the three X-ray telescopes behind six-position filters (see below). These CCDs are suited for extremely sensitive X-ray imaging (in the $0.15 - 15$ keV energy range) and moderate resolution X-ray spectroscopy over a field of view of $30'$. On the same telescopes carrying the MOS cameras are mounted two Reflection Grating Spectrometers (RGS, two identical grating structures on two mirror modules that deflect half of the beam on two of the X-ray telescopes), which provide high-resolution spectral information ($E/\Delta E \sim 200 - 800$ over the energy range $0.35 - 2.5$ keV). The design of the optics was driven by the requirement of obtaining the highest possible effective area over a wide range of energies, with particular emphasis in the region around 7 keV (*i.e.*, at the energies of the fluorescent Fe emission lines, one of the most important features in the X-ray spectrum, see Sect. II 1). Finally, the Optical Monitor can observe simultaneously the same region as the X-ray telescopes, but at ultraviolet and visible wavelengths. Below we summarize the main characteristic of XMM-*Newton*.

- Possible simultaneous operation of all science instruments (if not prohibited, *e.g.*, by target brightness constraints): simultaneous optical/UV observations make possible the monitoring and identification of optical/UV counterparts of X-ray sources seen by the X-ray telescopes as well as imaging of the surrounding field.
- High sensitivity: XMM-*Newton* carries the X-ray telescopes with the largest effective

area for a focusing telescope; the total mirror geometric effective area at 1.5 keV energy is ~ 1550 cm^2 for each telescope, *i.e.*, 4650 cm^2 in total.

– Angular resolution: the achieved point-spread function (PSF) has a Full Width at Half Maximum (FWHM) on the order of $6''$ and a Half Energy Width (HEW, where the 50% of the total energy is encircled) of $\sim 15''$.

– Moderate and high spectral resolution ($E/\Delta E \sim 20 - 50$).

The performance of each X-ray telescope is characterized mainly by its ability to focus photons, parameterized through the PSF, and to collect radiation at different photon energies, reflected by the effective area ($A_{\rm e}$).

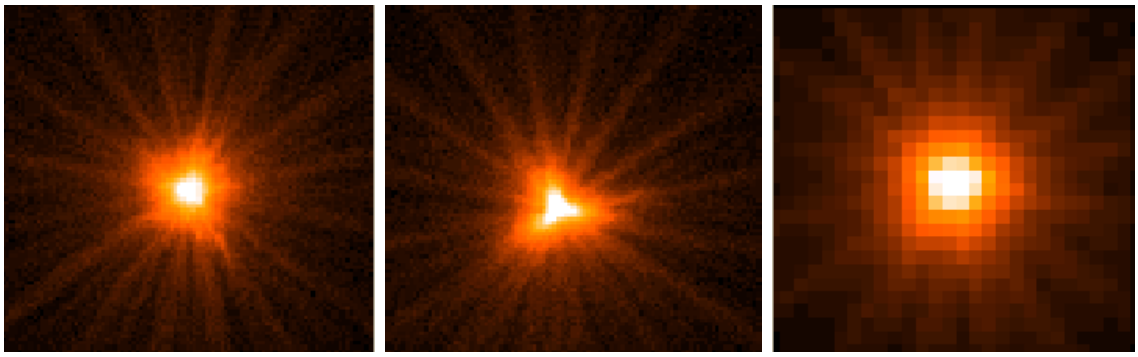

Figure 11 On axis PSF of the MOS1, MOS2 and pn X-ray telescopes (left to right). The shape of the PSF core (piled-up for this source) is slightly different for all cameras; the star-like pattern is created by the spider which supports the 58 co-axial Wolter I mirrors of the telescope.

The PSF Each of the three X-ray telescopes on board XMM-*Newton* has its own PSF; as an example, Fig. 11 shows the in orbit on-axis PSF of the MOS1, MOS2 and pn X-ray telescopes, registered on the same source.

The PSF could vary with the off-axis angle (*i.e.*, the distance from the center of the field of view; the elongation due to off-axis aberration is accentuated at large off-axis angles) and with the energy. In particular, one of the most important characteristic of XMM-*Newton* is that the core of its on-axis PSF is narrow and varies little over a wide energy range ($0.1 - 4$ keV). Above 4 keV, the PSF becomes only slightly more energy dependent.

The effective area A_e Concerning the effective area, Fig. 12, *left panel*, shows the values derived with the ready-made EPIC response matrices in case of full-frame mode and with the thin filter applied (see below) for all the different instruments. The effective areas of the two MOS cameras are lower than that of the pn, because these detectors are partially obscured by the RGSs. In Fig. 12, *right panel*, we show the decline of the X-ray telescope's effective area with the vignetting function (*i.e.*, the ratio of the off-axis area and the on-axis area at a fixed energy) for different energies. The vignetting function is the way to describe the decrease of the fraction of photons entering the telescopes that actually reach the focal plane with increasing off-axis angle; this effect is mainly due to the shadowing of the inner shells by the outer shells yielding a decrease of the effective area more and more larger as higher is the photon energy.

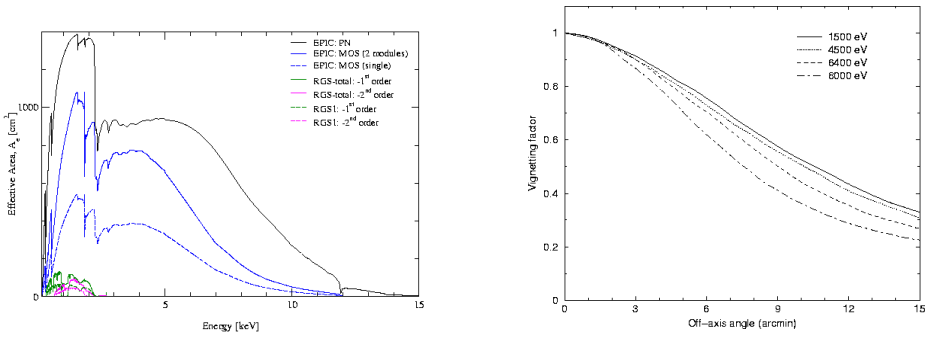

Figure 12 *Left panel:* the net effective area of all XMM-*Newton* X-ray telescopes, combined with the response characteristics of the focal X-ray instruments, EPIC and RGS (linear scale). *Right panel:* vignetting function of the X-ray telescope in front of the pn camera as a function of off-axis angle ($0' - 15'$, based on simulations) at a few selected energies.

Data acquisition mode All the EPIC CCDs operate in photon counting mode with a fixed, mode dependent frame read-out time frequency, producing event lists (which contain the `x` and `y` at which the events are registered, their energy and their arrival time). As mentioned, the MOS cameras are mounted on those X-ray telescopes that also carry RGS instruments. Therefore, they receive only 44% of the reflected light. MOS and pn differ for their geometry (see Fig. 13), but also for other properties, *e.g.*, their read-out times. The read-out of the pn chips is much faster than that of the MOS cameras, because each pixel column has its own read-out node. With this camera high-speed photometry of rapidly variable targets can be conducted. Moreover, the three cameras can operate in different

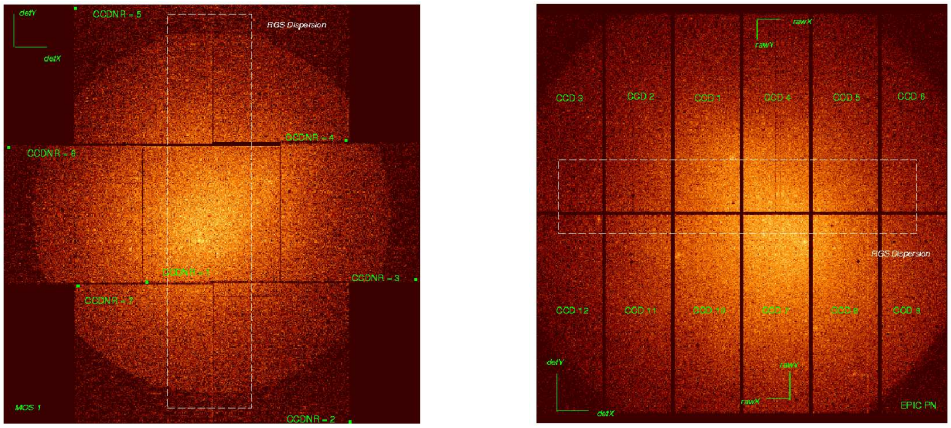

Figure 13 *Left panel:* layout of the EPIC MOS1 camera. The orientation of the DETX/DETY axes are shown, highlighting that the RGS dispersion axes are parallel within spacecraft physical co-ordinates. *Right panel:* layout of the EPIC pn camera; the orientation of the RAWX/RAWY (CCD specific) and of the DETX/DETY axes are shown.

data acquisition mode.

Filters Finally, the EPIC CCDs are sensitive not only to X-ray photons, but also to IR, visible and UV light. The main consequences are an increase of the system noise, an incorrect energy scale (because of finite offset for the nominally zero signal) and an excess of signal and noise fluctuations. To prevent this, the EPIC cameras include three different aluminised optical blocking filters (named "thick", "medium" and "thin"), as well as an internal "offset table" to subtract the constant level of (optical) light or other systematic shifts of the zero level of charge measurements. The use of a "thick" blocking filter (capable of minimizing the optical light contamination) will necessarily limit the softest X-ray energy response. It should be noted that also an off-axis bright optical object will leak through the filters, generating false X-ray events which could contribute to degrading the effective telemetry bandwidth.

Part I

PROPERTIES OF SMBHs AND HOST GALAXIES AT $0.4 < z < 1$

In this first part we present the estimate of black hole masses, bolometric luminosities and Eddington ratios for a sample of low–luminosity X-ray selected AGNs in the redshift range $0.4 \leq z \leq 1$. Sect. I 1 illustrates how this sample has been selected. This study has been possible thanks to the considerable amount of high quality data spanning a wide energy range available from the deep surveys carried out in the past few years. High spatial resolution and high signal-to-noise ratio data in the X-ray band gathered by the *Chandra* observations in the CDF-S and CDF-N (Giacconi et al. 2002; Rosati et al. 2002; Alexander et al. 2003; see Sect. 3.2) are of fundamental importance to select low–luminosity AGNs. We also took advantage of data from *HST* provided by GOODS for two smaller areas in the *Chandra* fields (see Sect. 3.1). The optical images, endowed with excellent spatial resolution and very high quality photometry, allow us to disentangle the galactic and nuclear components (the morphological analysis carried out is introduced in Sect. I 2, while Sect. I 3 is devoted to discuss its reliability), and to estimate the AGN bolometric luminosity and the black hole mass. The recovering of these properties is described in Sect. I 4, and our results are discussed and compared with those from the literature in Sect. I 5

If not otherwise stated, magnitudes are given in the AB system, and hard X-ray luminosities are in the $2 - 8$ keV energy range (when necessary, converted from $L_{\text{2-10 keV}}$ assuming a power-law X-ray spectrum with photon index $\Gamma = 1.8$: $L_{\text{2-8 keV}}/L_{\text{2-10 keV}} \simeq 0.84$).

I 1 Building-up the sample: selection criteria and checks for bias

The building up of an optimal sample for the kind of study we aimed is not an easy task. Incompleteness in redshift determinations, need of coverage in all the photometric passbands in the GOODS survey, required minimum signal-to-noise ratio for the analysis, limitations in the X-ray luminosity are all key steps in the procedure resulting in our final sample. In turn, any of these steps might be affected by potential problems whose effects may combine to give selection biases. Special care is thus required in order to sort out and minimize these biases.

We started by collecting all the X-ray sources in the *Chandra* fields with optical identification and spectroscopic redshift between 0.4 and 1 from the two catalogues reporting the optical follow up (Szokoly et al. 2004 for the CDF-S and Barger et al. 2003 for the CDF-N). The redshift interval was chosen to bracket a significant fraction of the low–luminosity sources contributing to the XRB. The upper bound $z = 1$ was imposed by the need of a signal-to-noise for the ACS bands high enough to make a reliable morphological analysis for most of the sources. This upper limit on the redshift also ensures that the observed z-band is always sampling the optical rest frame. Afterwards, a cross-correlation with the GOODS optical catalogues[1] restricted the sample to X-ray sources in the GOODS fields; finally, by using the X-ray informations reported in Giacconi et al. (2002; CDF-S) and Alexander et al. (2003; CDF-N) we selected sources with *observed* X-ray luminosity $L_{\text{2-8 keV}} > 10^{42}$ ergs s^{-1} in order to pick out *bona fide* AGNs (Zezas, Georgantopoulos & Ward 1998; Moran et al. 1999).

The determination of spectroscopic redshifts in the two *Chandra* fields is far from being complete ($\sim$ 48% of the CDF-S X-ray sources has a spectroscopic redshift; in the CDF-N, the percentage is $\sim$ 56%). Hence, our initial request of having spectroscopic redshift could introduce an implicit "optical flux limit" in the selection. As a consequence, this first approach to collect the sample made difficult to evaluate whether these criteria introduce a bias towards optically luminous objects, and to address the role that the possible optical selection effects may play. Hence, we decided to examine in much more details the issue of the sample selection.

First, we chose to extend our search also to photometric redshift catalogues. There are several groups carrying out the photometric follow up in the *Chandra* fields.

[1] Available at `ftp://archive.stsci.edu/pub/hlsp/goods/`

CDF-N For a number of sources without spectroscopic information, Barger et al. (2003) report a photometric estimate: thus, the completeness of redshift determination claimed by the authors is $\sim 69\%$. A second group of photometric redshifts is in progress at STScI.

CDF-S Photometric redshifts have been published by Zheng et al. (2004), Mainieri et al. (2005) and Grazian et al. (2006) for almost all the X-ray sources in the field. As for the CDF-N, the derivation of photometric redshifts for a second group of objects is underway at STScI.

There are objects that appear in more than one catalogue, in some cases with different values. Due to the discrepancy existing between spectroscopic and photometric redshifts from STScI, we decided to ignore the latter values for both fields (even at the price of reducing the completeness in the CDF-N; see Fig. I 1); this choice is supported also because that redshift survey is still an on-going project. In this way, for the CDF-N we were only left with the redshifts (spectroscopic *or* photometric) presented in Barger et al. (2003). Concerning the CDF-S, the comparison between spectroscopic and photometric redshifts indicates that the photometric estimates of Grazian et al. (2006) are in good agreement with the spectroscopic values, thus much more reliable. According to these comparisons, we adopted the spectroscopic information when available; otherwise, the priority was assigned

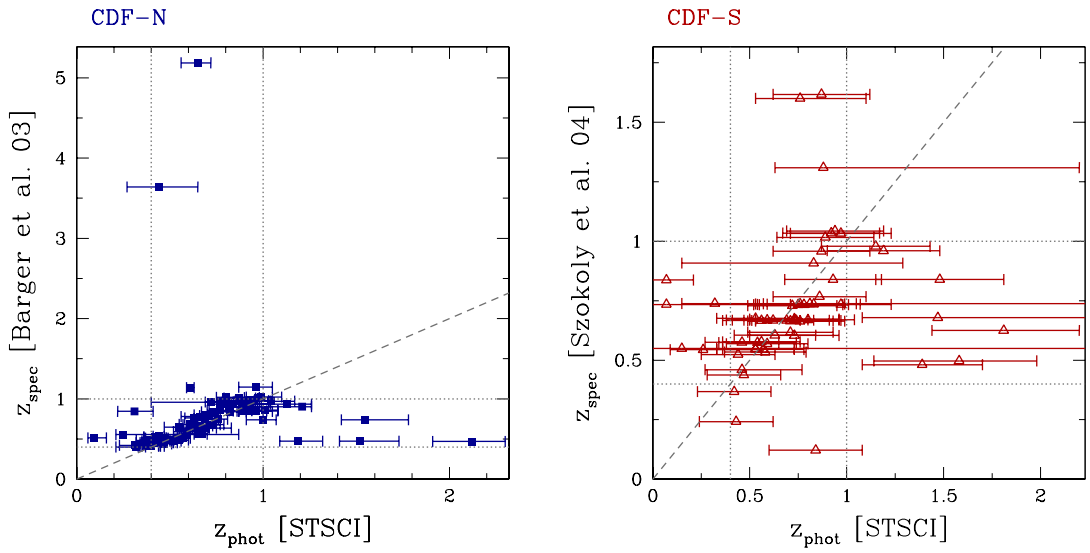

Figure I 1 Photometric redshifts from STScI compared with spectroscopic values, from Szokoly et al. (2004; CDF-S) and Barger et al. (2003; CDF-N).

to the catalogue of Grazian et al. (2006), complemented with the values from Zheng et al. (2004) for sources not reported in the former. In summary, by using both spectroscopic and photometric redshift we had information for $\sim 98\%$ of the X-ray sources in the CDF-S and $\sim 69\%$ for the CDF-N, respectively.

The second aspect to be addressed in the new selection process was the choosen cut in X-ray luminosity. First, for sake of homogeneity the X-ray information was collected from Alexander et al. (2003) for both fields. To understand if there is a bias against X-ray emitting optically faint objects, it is interesting to estimate the fraction of X-ray AGNs with redshift determinations in the area covered by GOODS.

If we make this comparison considering also the lowest luminosity side (*i.e.*, normal or starbursting galaxies), we include sources that probably do not have redshift information and at the same time are not target of this analysis: so we risk to *underestimate* this number. On the other hand, with no knowledge of the redshift we cannot estimate their luminosity. To get over this impasse, we assumed a typical spectrum (a power law with photon index $\Gamma = 1.8$) and estimated the limiting flux $F_{\rm lim}$ observed for a source with $z = 1$ (the upper bound of the sampled redshift range) that emits a luminosity $L_{\rm 2\text{-}8\,keV} = 10^{42}$ ergs s^{-1}. Afterwards, we determined the fraction of *Chandra* sources with $F > F_{\rm lim}$ in the area covered by GOODS with redshift determination. However, this could introduce a strong bias against obscured sources. Thus, we were forced to consider *all* the X-ray sources in the GOODS fields.

Finally, the steps for the sample selection are as in the following and they are summarized in Table I 1.

1. We started from the two *Chandra* catalogues as reported by Alexander et al. (2003); column (2).

2. We restricted our selection to the X-ray sources lying in the two regions of the sky defined by the GOODS ACS South and North catalogues in the i-band[2]; column (3).

3. By cross-correlating the GOODS optical catalogues with the *Chandra* X-ray catalogues we found an optical counterpart for $\sim 98 - 99\%$ among these X-ray sources; column (4).

4. Columns (5) and (6) show the number of X-ray sources with optical counterpart in the GOODS catalogues for which there are spectroscopic or photometric redshift

[2] `h_goods_si_r1.1z_cat.txt` and `h_goods_ni_r1.1z_cat.txt`; these files are available at the URL of the GOODS project, `ftp://archive.stsci.edu/pub/hlsp/goods/catalog_r1`

Table I 1. Steps in the sample selection.

Field	X-ray src	...in GOODS area	...with ID GOODS	...with z info		...$0.4 < z < 1$		...$\log L_{\rm X} > 42$		...cutouts OK		...isolates	
...	...	...	...	$z_{\rm spec}$	$z_{\rm phot}$	$z_{\rm spec}$	$z_{\rm phot}$	$z_{\rm spec}$	$z_{\rm phot}$	$z_{\rm spec}$	$z_{\rm phot}$	$z_{\rm spec}$	$z_{\rm phot}$
(1)	(2)	(3)	(4)	(5)	(6)	(7)	(8)	(9)	(10)	(11)	(12)	(13)	(14)
CDF-N	503	261	258	163 + 41		93 + 9		26 + 5		25 + 3		15 + 0	
CDF-S	326	197	196	134 + 60		63 + 5		32 + 3		23 + 2		18 + 1	

Note. —

Col. (1): North or South field observed.

Col. (2): Number of X-ray sources.

Col. (3): Number of X-ray sources in the GOODS area as identified by i-band observations.

Col. (4): Number of X-ray sources with optical counterpart in the i-band GOODS ACS catalogue.

Col. (5) − Col. (6): Number of X-ray sources identified in the i-band GOODS ACS catalogue with redshift (spectroscopic, from Barger et al. 2003 and Szokoly et al. 2004; or photometric, from Barger et al. 2003, Grazian et al. 2006 and Zheng et al. 2004).

Col. (7) − Col. (8): Number of X-ray sources with GOODS counterpart and redshift (spectroscopic or photometric, respectively) between 0.4 and 1.

Col. (9) − Col. (10): Number of X-ray sources with GOODS counterpart, $0.4 < z < 1$ (spectroscopic or photometric, respectively), and $L_{\rm 2\text{-}8\,keV} > 10^{42}$ ergs s^{-1}.

Col. (11) − Col. (12): Number of X-ray sources with GOODS counterpart, $0.4 < z < 1$ (spectroscopic or photometric, respectively), $L_{\rm 2\text{-}8\,keV} > 10^{42}$ ergs s^{-1}, and without damaged cutouts (SAMPLE A).

Col. (13) − Col. (14): Number of *isolated* X-ray sources with GOODS counterpart, $0.4 < z < 1$ (spectroscopic or photometric, respectively), $L_{\rm 2\text{-}8\,keV} > 10^{42}$ ergs s^{-1}, and without damaged cutouts (SAMPLE B).

information, respectively.

5. In the next step we restricted the sample to the redshift range $0.4 < z < 1$, leading to a substantial decrease in the source number; columns (7) and (8).

6. Afterwards, we discarded all the sources with $L_{2\text{-}8\,\mathrm{keV}}$ lower than 10^{42} ergs s^{-1}, producing a second substantial decrease in the source number; columns (9) and (10). The selection was then reduced to 66 sources, 88% of them having spectroscopic redshifts.

7. As described in Sect. I 2, we also had to reject sources for which the quality of one or more cutouts (*i.e.*, the small postage stamps of the GOODS ACS images centered on the source) was significantly below the average, typically due to a non-optimal data acquisition ($\sim$ 20%; an example is shown in Fig. I 9); columns (11) and (12). The objects remaining after this step are what we define "SAMPLE A". Fig. I 2 shows how the SAMPLE A is distributed as a function of redshift (*left panel*), hard X-ray luminosity (*middle panel*) and optical magnitude (*right panel*). The spikes visible in the redshift distribution trace the large scale structures identified in the whole CDF-S at $z = 0.67$ and $z = 0.73$ both in the optical (Vanzella et al. 2005) and in the X-ray range (Gilli et al. 2003), and at $z \sim 0.85$ in the CDF-N (see Barger et al. 2003; Gilli et al. 2005).

8. In the final step we discarded sources that we found to be "not isolated" (*i.e.*, with a close companion within a projected radius of $2''$; this operational criterion does not make distinction between physical interaction or projection effect; see also Sect. I 2 and Fig. I 10); in this way the analysed sample (hereinafter referred to as SAMPLE B) reduces to 34 objects (19 in the CDF-S and 15 in the CDF-N; *i.e.*, 64% of the SAMPLE A); columns (13) and (14). Sources of our SAMPLE B are listed in Table I 2.

All the cautionary tests performed during the selection make us confident that we did not introduced important biases. In particular, we have some caveats.

– We note that the X-ray sources in the GOODS fields with a redshift determination overlap in the same region of the F_{X}-F_{opt} plane the whole database of the "GOODS X-ray sources" (see Fig. I 3): according to a bidimensional Kolmogorov-Smirnov test, we cannot prove that the two samples are drawn from different distributions (the KS–probability is $\sim$ 60%). This makes us confident that selecting only sources with redshift determination does not introduce any biases towards optically bright objects.

Table I 2. Basic informations for X-ray selected AGNs (observed $L_{2\text{-}8\,\mathrm{keV}} > 10^{42}$ ergs s^{-1} in the GOODS fields with $0.4 < z < 1$) analysed in this work (SAMPLE B).

ID ... (1)	R.A. (J2000) (h:m:s) (2)	Decl. (J2000) (d:m:s) (3)	Redshift ... (4)	$\log L_{2\text{-}8\,\mathrm{keV}}$ (ergs s^{-1}) (5)	i AB (mag) (6)
		CDF-N			
1	12 : 36 : 18.58	+62 : 11 : 15.0	0.679	43.20	20.46
2	12 : 36 : 25.01	+62 : 21 : 15.7	0.747	42.29	21.87
3	12 : 36 : 27.75	+62 : 11 : 58.4	0.762	42.34	23.10
4	12 : 36 : 32.59	+62 : 07 : 59.8	0.680	42.16	21.83
5	12 : 36 : 35.86	+62 : 07 : 07.7	0.555	42.37	21.99
6	12 : 36 : 42.24	+62 : 06 : 12.8	0.857	42.60	21.38
7	12 : 36 : 46.33	+62 : 14 : 04.7	0.961	43.62	21.57
8	12 : 36 : 54.58	+62 : 11 : 10.6	0.955	42.43	22.47
9	12 : 36 : 59.09	+62 : 25 : 23.7	0.678	42.97	20.76
10	12 : 37 : 02.43	+62 : 19 : 26.1	0.514	43.27	19.70
11	12 : 37 : 10.07	+62 : 05 : 47.9	0.935	42.09	23.69
12	12 : 37 : 22.44	+62 : 05 : 36.1	0.978	42.61	21.87
13	12 : 37 : 24.00	+62 : 13 : 04.3	0.474	42.33	24.25
14	12 : 37 : 31.73	+62 : 17 : 03.7	0.839	42.61	20.89
15	12 : 37 : 39.46	+62 : 22 : 39.2	0.838	42.27	21.39
		CDF-S			
16	3 : 32 : 33.02	−27 : 45 : 47.4	0.839	42.93	22.19
17	3 : 32 : 26.76	−27 : 41 : 45.6	0.667	42.85	21.61
18	3 : 32 : 27.00	−27 : 41 : 05.1	0.734	44.17	19.12
19	3 : 32 : 27.61	−27 : 41 : 45.0	0.737	42.65	21.89
20	3 : 32 : 24.84	−27 : 56 : 00.0	0.733	42.64	21.44
21	3 : 32 : 24.84	−27 : 56 : 00.0	0.534	42.48	20.61
22	3 : 32 : 20.07	−27 : 44 : 47.0	0.670	42.35	23.76
23	3 : 32 : 17.18	−27 : 52 : 20.9	0.569	42.88	20.84
24	3 : 32 : 20.07	−27 : 44 : 47.0	0.604	42.36	22.11
25	3 : 32 : 08.24	−27 : 41 : 53.6	0.545	42.07	21.80
26	3 : 32 : 46.98	−27 : 43 : 46.2	0.664	42.14	20.00
27	3 : 32 : 22.51	−27 : 48 : 04.8	0.734	42.04	22.64
28	3 : 32 : 35.23	−27 : 53 : 17.8	0.733	42.48	21.76
29	3 : 32 : 39.73	−27 : 46 : 11.2	0.679	42.39	25.38
30	3 : 32 : 18.99	−27 : 47 : 55.4	0.481	42.13	24.71
31	3 : 32 : 13.92	−27 : 50 : 00.7	0.549	42.08	22.44
32	3 : 32 : 13.83	−27 : 45 : 25.6	0.735	42.01	21.23
33	3 : 32 : 34.73	−27 : 55 : 33.8	0.668	42.08	21.44
34	3 : 32 : 23.88	−27 : 58 : 42.4	0.910	42.29	22.54

Note. —
Col. (1):Source identification number.
Col. (2) & (3): J2000 right ascension and declination of the X-ray object.
Col. (4): Redshift for the optical counterpart, from Barger et al. (2003), Szokoly et al. (2004), Grazian et al. (2006) and Zheng et al. (2004).
Col. (5): *Observed* X-ray luminosity in the $2 - 8$ keV band.
Col. (6): AB magnitude in the i band from the GOODS ACS catalogue (available at `ftp://archive.stsci.edu/pub/hlsp/goods/catalog_r1`).

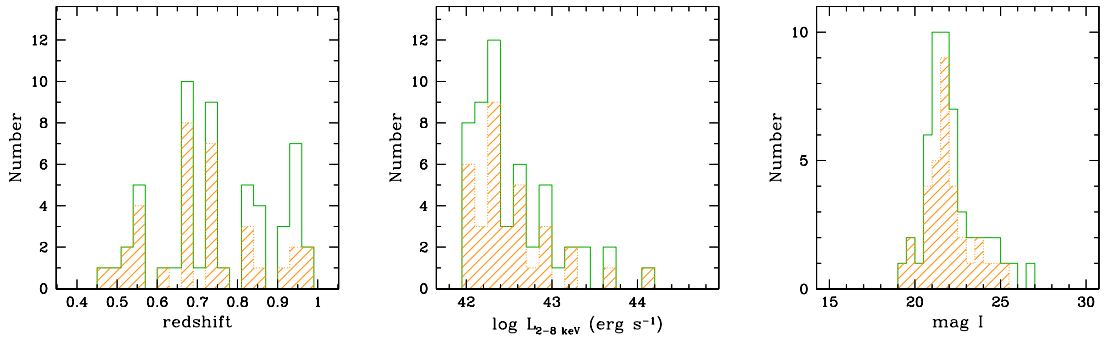

Figure I 2 Number of sources as a function of redshift (*left panel*), hard X-ray luminosity (*middle panel*) and i-band magnitude (*right panel*) for the SAMPLE A (X-ray sources in GOODS with spectroscopic or photometric redshifts between 0.4 and 1, observed hard X-ray luminosity $L_{2\text{-}8\,\mathrm{keV}} > 10^{42}$ ergs s^{-1} and with good cutouts in all bands); dashed areas show the same distributions for the analysed sources (SAMPLE B). Redshifts are from Szokoly et al. (2004), Grazian et al. (2006) and Zheng et al. (2004) for the CDF-S, and Barger et al. (2003) for the CDF-N; luminosities are from Alexander et al. (2003); i-band magnitudes are from the GOODS ACS catalogue (`ftp://archive.stsci.edu/pub/hlsp/goods/catalog_r1`).

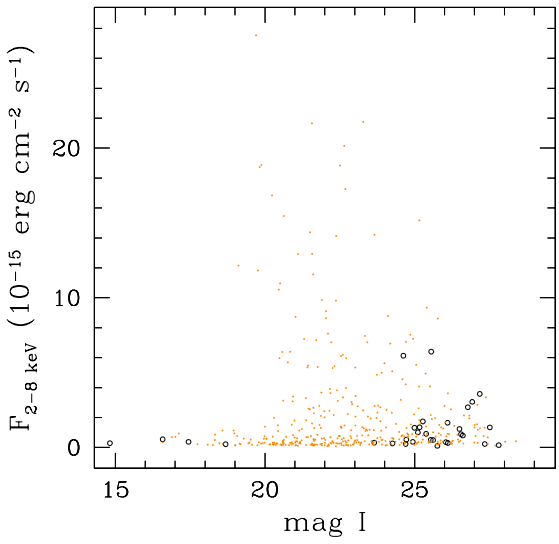

Figure I 3 Hard X-ray fluxes versus i-band magnitudes for the X-ray sources in the GOODS fields with (yellow dots) and without (black open circles) redshift informations.

– By comparing columns (5), (6), (7) and (8) it clearly appears that a larger decrease in number takes place for sources with only photometric redshifts. This result is not surprising, considering the distribution of spectroscopic and photometric redshifts of the sources in the South field (for which the redshift determination is almost complete): the first is clearly peaked between 0.5 and 1.2, while in the second case $\sim 88\%$ of the sources have $z > 1$. Besides, the fraction of sources retained in this step is reassuringly consistent with what estimated by integrating the QSO luminosity function down to the GOODS flux limits. We expect in fact to observe in the redshift range $0.4 < z < 1$ 37% of the total number in the interval $0 < z < 4$, and the fraction of spectroscopic and photometric redshifts assigned to the $0.4 < z < 1$ range turns out to be 27%.

– The largest decrease in the source number occurs because of the selection in redshift ($0.4 < z < 1$) and X-ray luminosity ($L_{\text{2-8 keV}} > 10^{42}$ ergs s^{-1}).

– As said, in order to carry out the morphological analysis described in the next section, the simultaneous availability of high-quality, non-crowded B, V, i and z ACS cutouts is essential. For the same reason mentioned above, objects lying in crowded fields have been excluded from the analysis. We checked that the objects for which these require-

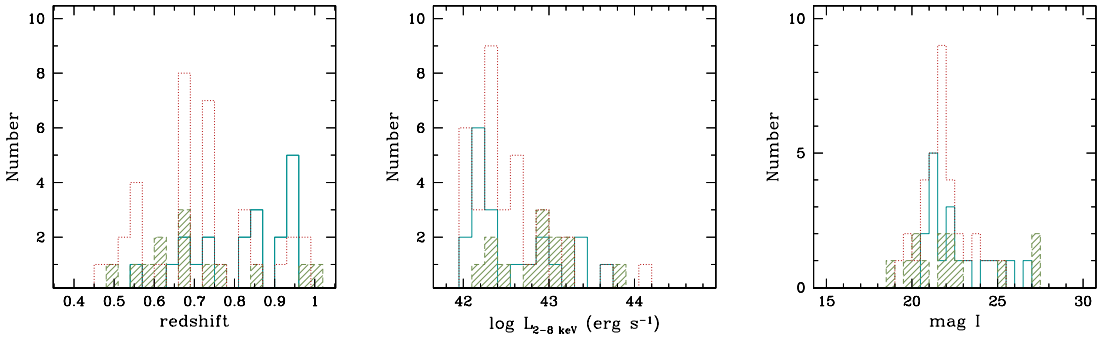

Figure I 4 Distributions in redshift (*left panel*), hard X-ray luminosity (*middle panel*) and i-band magnitude (*right panel*) for three subsamples of the GOODS X-ray sources with spectroscopic or photometric redshifts between 0.4 and 1 and observed hard X-ray luminosity $L_{\text{2-8 keV}} > 10^{42}$ ergs s^{-1}: sources with at least one bad cutout (green dashed line, shaded area); sources not isolated (cyan solid line); analysed sources (SAMPLE B; red dotted line). Redshifts are from Szokoly et al. (2004), Grazian et al. (2006) and Zheng et al. (2004) for the CDF-S, and Barger et al. (2003) for the CDF-N; luminosities are from Alexander et al. (2003); i-band magnitudes are from the GOODS ACS catalogue (available at `ftp://archive.stsci.edu/pub/hlsp/goods/catalog_r1`).

ments are not satisfied (and then removed in assembling SAMPLE A and SAMPLE B) have a random distribution in luminosity, redshift or spectral classification; so we are confident that rejecting these sources does not introduce any kind of bias against a particular class of objects. Fig. I 4 shows the distribution in redshift, hard X-ray luminosity and i-band magnitude of the sources rejected because they have at least one bad cutout (green dashed line, shaded area) or were classified as "not isolated" (cyan solid line), as compared to the distributions for the analysed sources (SAMPLE B, red dotted line).

– As is clear in Fig. I 2, the redshift and luminosity distributions of SAMPLE B (dashed areas) match the distributions of SAMPLE A. According to a Kolmogorov-Smirnov test, we cannot prove that the two samples are drawn from different hard X-ray luminosity or redshift distributions (the KS–probabilities are 99% and 75%, respectively).

I 1.1 The X-ray view

A first look at the selected sample comes from an inspection of their X-ray properties, as they can be deduced from the *hardness ratios* reported by Alexander et al. (2003). These ratios are an equivalent of X-ray colours, generally defined as a comparison of the number of counts s^{-1} detected in different energy bands: HR$\equiv$ $(HARD - SOFT)/(HARD + SOFT)$. Diagnostic diagrams involving the hardness ratios are frequently applied when the spectral analysis can not be performed properly, because of too large samples or too faint sources (see also Sect. II 3).

The diagrams shown in Fig. I 5, where we define HR$=$ $(H - S)/(H + S)$ with $S = [0.5{-}2\,\mathrm{keV}]$ counts s^{-1} and $H = [2{-}8\,\mathrm{keV}]$ counts s^{-1}, describe our sample as composed mostly by type 2 AGNs, with only one type 1 QSO. The expected column densities for the absorbed AGNs span the range between 10^{22} cm^{-2} and 10^{23} cm^{-2}.

To test the predictions of these diagrams we can use the spectral analysis reported in Tozzi et al. (2006) for the sources in the CDF-S. The good agreement we found between hardness ratios and observed column densities is reassuring, although it is limited to a dozen of sources (those with number counts high enough to leave all the parameters free during the spectral fit; the analysis is performed also in the other cases, but assuming a constant photon index, so for these sources the comparison is trivial).

The contributions of SAMPLE A to the soft and hard XRB[3] are 10% and 16%,

[3]Average total flux density, from De Luca & Molendi (2004): $(8.12 \pm 0.35) \times 10^{-12}$ erg cm^{-2} s^{-1} deg^{-2} in the soft band and $(1.79 \pm 0.11) \times 10^{-11}$ erg cm^{-2} s^{-1} deg^{-2}, converted from the $2 - 10$ keV band by

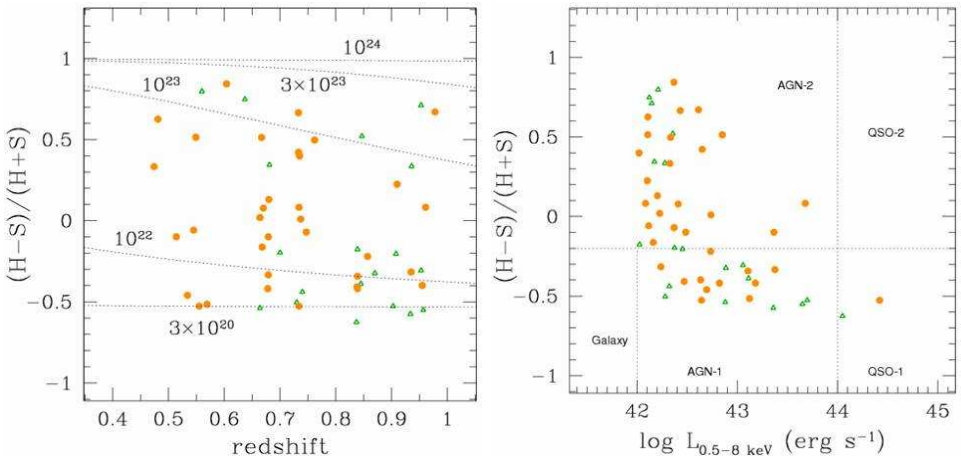

Figure I 5 Diagnostic diagrams for the analysed sample (yellow filled circles). Green open triangles mark the sources rejected (because of the interaction criterion) in passing from SAMPLE A to SAMPLE B. *Left panel:* hardness ratio versus redshift; the curves indicate the loci expected for spectra described by an absorbed power law with photon index $\Gamma = 1.8$ ($F_\nu \propto \nu^{1-\Gamma}$) and column density $N_{\rm H}$ as labelled. *Right panel:* hardness ratio versus observed total X-ray luminosity; the region of the plane typically occupied by different classes of sources is indicated.

respectively. In Fig. I 6 we compare the total contribution to the hard XRB computed from the CDF-S plus *ASCA* sample (Della Ceca et al. 2001; long-dashed line, the grey area representing the estimated uncertainties, see Tozzi 2001) with the integrated contribution of the SAMPLE A (continuous line) and of the selected 34 sources (dashed line). This comparison shows that with the analysed sources we are sampling in a uniform way the same range of flux of the SAMPLE A. In summary, the SAMPLE B is considered representative of the whole population of X-ray sources with spectroscopic or photometric redshifts between 0.4 and 1 and luminosity $L_{\rm 2\text{-}8\,keV} > 10^{42}$ ergs s^{-1}, and only scaled (*i.e.*, sparsely sampled) by a factor of 7. Both the SAMPLE A and the analysed objects cover the luminosity range $10^{42} \leq L_{\rm 2\text{-}8\,keV} \leq 3 \times 10^{43}$ ergs s^{-1}, while only a few sources exhibit larger luminosity. Taking into account the redshift and luminosity distributions, we can conclude that the SAMPLE B is representative of the AGNs contributing to the XRB at $z \leq 1$ (see Fig. I 7, from Ueda et al. 2003).

assuming the photon index of the XRB spectrum, $\Gamma = 1.4$.

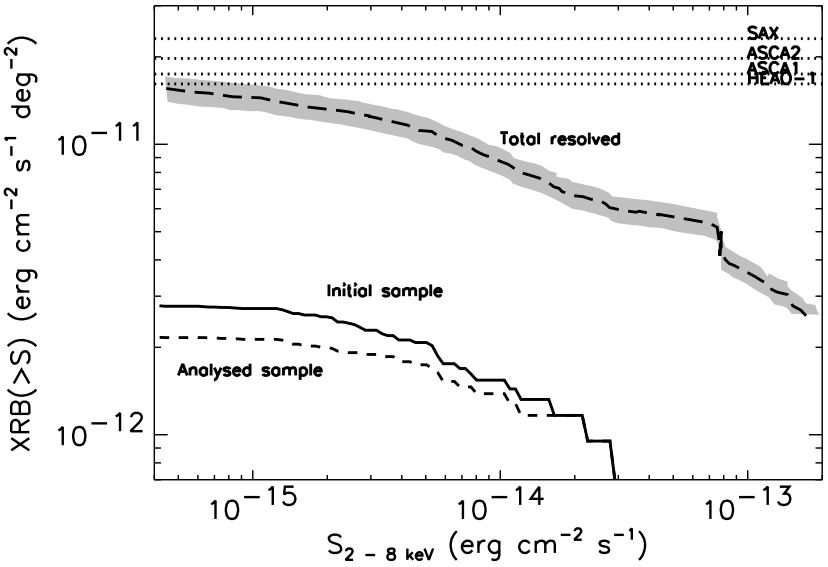

Figure I 6 Contribution to the $2-8$ keV X-ray flux density as a function of the resolved sources. We show the comparison between *1)* the total resolved contribution (long-dashed line, with grey area representing the estimated uncertainties) computed from the 1 Msec CDF-S sample plus the bright sample from *ASCA* (Della Ceca et al. 2001) at fluxes larger than 10^{-13} ergs cm^{-2} s^{-1}, see Tozzi (2001); *2)* the contribution of our initial selection (SAMPLE A: GOODS X-ray sources with spectroscopic or photometric redshifts between 0.4 and 1, observed hard X-ray luminosity $L_{2\text{-}8\,\mathrm{keV}} > 10^{42}$ ergs s^{-1} and with good cutouts in all bands; continuous line); *3)* the contribution of the analysed sources, as in Table I 2 (SAMPLE B; dashed line). The upper dotted lines refer to previous measures of the unresolved hard X-ray background; from bottom to top: Marshall et al. (1980), Ueda et al. (1999), Ishisaki et al. (2001), Vecchi et al. (1999).

I 2 Host galaxy components: morphological analysis with GALFIT

Methodological approach Our aim is to obtain a deep insight on the nuclear components in all the objects selected in our sample. In particular, to separate a typically faint nucleus from the surrounding bright bulge we need to determine accurate morphological information. The lack of this information was in fact the major obstacle to study the central sources on a quantitative basis.

However, two main problems are known to affect direct observations of galaxies hosting AGNs, even for not extreme redshift ranges.

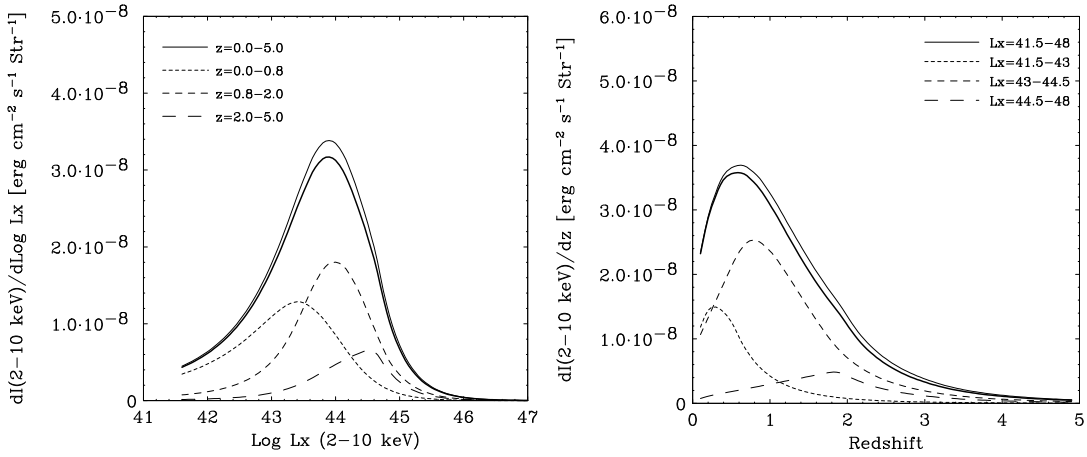

Figure I 7 Differential contribution of AGNs to the $2-10$ keV XRB intensity as a function of luminosity (*left panel*) and redshift (*right panel*); from Ueda et al. (2003). The authors computed the contribution from different ranges of redshift (*left panel*) or luminosity (*right panel*) starting from their best fit to the hard X-ray luminosity function and their $N_{\rm H}$ function. The uppermost curves represent the case when the Compton-thick AGNs are included.

– The small angular scales involved ($1''$ subtends about 7 kpc at $z \sim 0.7$, in the middle of the redshift range of our sample).

– The point-like nature of the nuclear source itself. For very strong AGNs the nuclear emissions could mask the features of the host galaxy and, *vice-versa*, the light from the underlying spheroids might overwhelm the nuclear sources when the AGN is not very powerful.

Both these problems in principle may hamper our goal to reach a quantitative description of morphological parameters for all the relevant galactic components. As a consequence, the main novelty in the present study is to exploits the capabilities of ACS-*HST*, namely both its superior resolution and imaging quality. In order to disentangle the main galactic components (nucleus, bulge and disk) of galaxies hosting the AGNs for the 34 sources listed in Table I 2, we performed a morphological analysis of the GOODS ACS-*HST* images (see Sect. 3.1).

In our analysis, we adopted a two-dimensional fitting approach. It has been shown that a two-dimensional modeling allows a better estimate of the parameter values in a bulge-disk decomposition (*e.g.*, Byun & Freeman 1995; Wadadekar et al. 1999). In fact, the smooth merging of the bulge and disk components in a galaxy may often result into the

onset of a degeneracy in the solutions. On the other hand, the two-dimensional approach takes advantage of ellipticity changes and/or isophotal twisting to put stronger constraints to the model. This provides a more unambiguous uniqueness of the solution, as compared to one-dimensional modeling. Moreover, a central component as an active nucleus, although photometrically distinct on an image, due to its nearly round shape when collapsed into a one dimensional, azimuthally averaged surface brightness profile can be easily blended with the inner part of the bulge light distribution. Making use of all the information available (*i.e.*, working with the full two dimensional image) can significantly help in improving the decomposition process.

For all sources, the images were fitted with a galaxy model composed of a bulge, a disk and a nuclear source. Notice that we are not implying that our sample on the whole is composed only of objects having all these components. The only feature whose presence is certain *a priori* is of course the nuclear component: due to our selection criteria, all the selected sources do contain an active nucleus. Regarding the other galactic components, in our surface photometry decomposition we took advantage of images in four different bands, as obtained from ACS-*HST*. We have two red bands (z and i) as well as two bluer bands (V and B) available from the survey GOODS; the different components of the host galaxy will have a different relative importance in each bandpass. Hence, using all these available bands to extract the morphological informations we are able to asses the derived parameters in a solution more suitable to the *actual* morphology of each galaxy. As a consequence, the requirement of good cutouts in all the four bands is a key one in the selection process of the sample, as described above.

The main parameters derived from the decomposition are the magnitudes of the nuclear component and of the bulge: the first will enter in the determination of the bolometric luminosity of the AGN and the second will be used to obtain the black hole masses, when coupled with an appropriate relationship between bulge magnitude and mass of black hole (see Sect. I 4).

The choice of the package: detailed analysis Among the publicly available softwares designed to accurately model bidimensional galaxy profiles, the most popular are GALFIT (Peng et al. 2002) and GIM2D (Simard et al. 2002). These two programs for morphological galaxy deconvolution are based on different minimization algorithms (that results into GIM2D being remarkably more expensive in term of CPU). The latter has been specifically designed to be fully automated in bulge-disk decomposition, while GALFIT was not con-

Table I 3. Comparison between GALFIT and GIM2D.

Software (1)	Nuclear comp. available (2)	Fit simultaneous in several bands (3)	Good in working with mosaics (4)	Automated batch fitting (5)
GALFIT	$\surd$	$\times$	$\surd$	$\times$
GIM2D	$\times$	$\surd$	$\times$	$\surd$

Note. —
Col. (1): Software under exam.
Col. (2): Nuclear component available to be added to the fitted model.
Col. (3): Possibility of performing the fit simultaneously on several images, in different bands.
Col. (4): Adequate return in working with treated images (drizzling; mosaics).
Col. (5): Complete automation in performing the decomposition.

ceived to do automated batch fitting of galaxies. One of the most interesting properties of GIM2D is the possibility of fitting stacks of images *even in different bands* simultaneously. On the other hand, GALFIT was designed to extract nuclear point sources, combining simultaneously an arbitrary number of profiles. Their performances look quite similar, both strongly dependent on the initial guesses for the model parameters. The main characteristics taken into account in choosing the software of analysis are compared in Table I 3. The most important point is that, unlike GIM2D, GALFIT has the possibility to include a nuclear component in the fitted model. Indeed, a possible method to use GIM2D would be to perform a bulge-disk decomposition on the *PSF-subtracted* images. This could be a good approach to study the morphology of the host galaxy, but it is a poor way to collect information on the nuclear component. Moreover, the authors suggest of using archival images; mosaics of imaging or drizzling (if the data are dithered) must be avoided (Simard et al. 2002; Tran 2000). On the other hand we worked with *HST* images processed by the GOODS team, as described in Sect. 3.1 (see also Giavalisco et al. 2004). Hence, GALFIT appears to be better suited to our purposes, since we are interested in the nuclear engines of AGNs nested in their host galaxies.

The fitting algorithm of GALFIT constructs a model image, convolves it with a

PSF, and finally compares the result with the data. In order to construct our own PSF for each band, we identified in the GOODS ACS images a number of point sources and averaged them.

During the fit, the reduced χ^2 is minimized using a Levenberg-Marquardt algorithm (Press et al. 1997). The uncertainties as a function of the pixel position used to calculate the reduced χ^2 are the Poisson errors, and are generated on the basis of the GAIN and the READ-NOISE parameters, recovered using the Weight Map Images provided by the GOODS Team.

Each galaxy was fitted with a de Vaucouleur model (to describe the bulge) and an exponential function (representing the disk). Moreover, we always assumed the presence of a nuclear source, obtained by adding a PSF component to the above model. We also assume that the morphological parameters for each component are color-independent, *i.e.*, position angle, axial ratio and optical radius are the same for each passband.

In order to exploit all the information we had (*i.e.*, the images in four passbands) even using software that cannot work with several images simultaneously, we implemented a three-step procedure (with a number of free parameters different from step to step). A schematic diagram representing the whole process of analysis is shown in Fig. I 8 and individual steps are illustrated in the following.

0) We need to provide GALFIT with initial guesses for the parameters of the models (magnitudes, scale length, position angle and semi-minor axis to semi-major axis ratio). They have been drawn from the GOODS ACS public catalogue[4] (the MAG_BEST, A_IMAGE and/or FLUX_RADIUS, THETA_IMAGE and ELLIPTICITY parameters, respectively). In particular, magnitudes reported in this catalogue refer to the whole galaxy, while GALFIT requires an initial value for each component: as a starting point, we split the observed value ascribing the same flux to each component.

1) First, we adopted a two-component model, always comprising a nucleus, while the host galaxy has been described using only the component that is expected to dominate in each band. Thus, the galaxy was modelled as pure disk + nucleus in the B and V filters, while we assumed for the i and z bands a pure bulge + nucleus description. We note again that we are talking about a two-component *independent* fit. At the end of this first step, we compared the parameters resulting from the analysis in the B and V bands: position angle PA_d, axis ratio b/a_d and radius R_d, for the

[4] Available at `ftp://archive.stsci.edu/pub/hlsp/goods/catalog_r1`

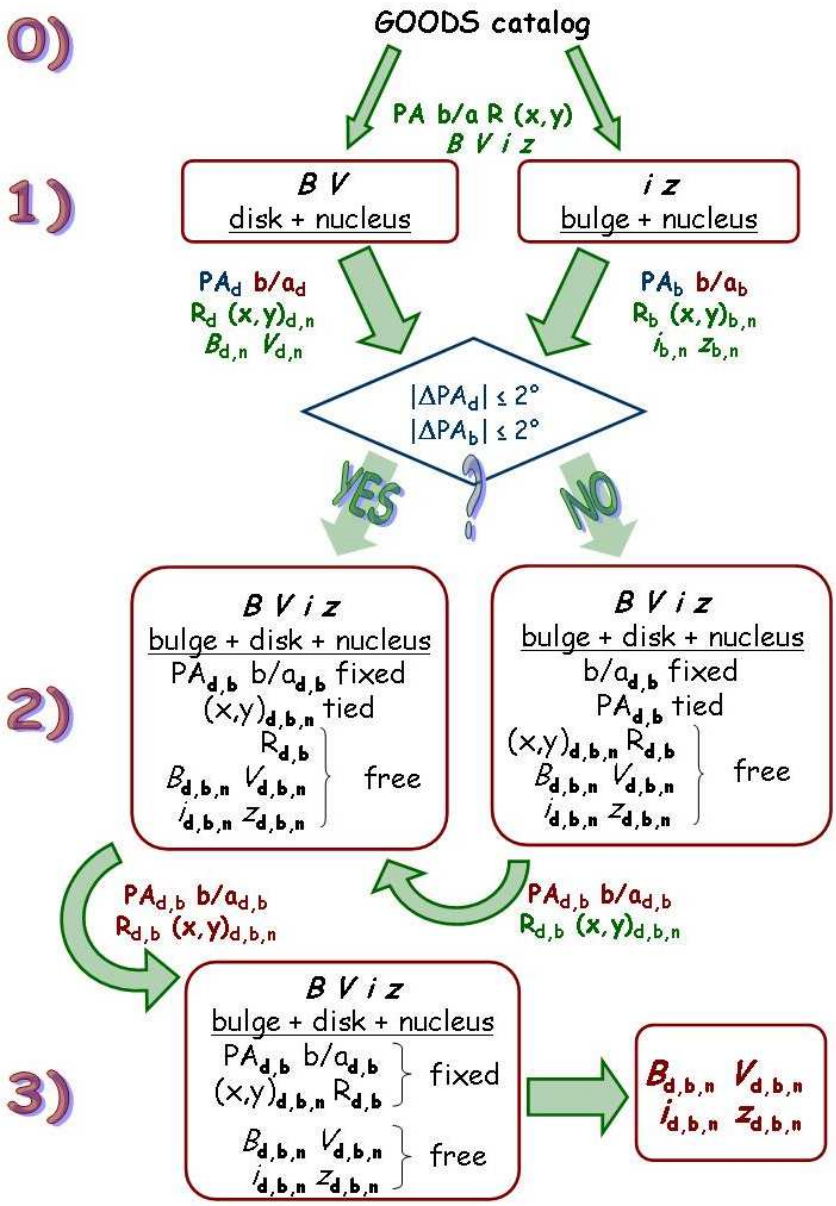

Figure I 8 Flux diagram showing the various steps of the performed decomposition. Square red boxes refer to a single run of GALFIT; parameters subject to a check are implemented in blue rhomboidal box. Quantities near plumpy arrows connecting two boxes indicate the introduction from the starting box of new guesses (in green; labeled as "free" or "tied" in the box of arrival) or fixed values (colored red) for the corresponding parameter, respectively. Pedices "n", "b" and "d" indicate parameters of the *nucleus*, *bulge* and *disk* component.

disk component; centers $(x, y)_n$ and $(x, y)_d$ for both nucleus and disk. We behaved likewise starting from the output of the analysis in the i and z bands, comparing the two values of position angle PA_b, axis ratio b/a_b, radius R_b and center $(x, y)_b$ of the bulge component, and the center of the nucleus, $(x, y)_n$.

- Axis ratios, centers and radii obtained from the fit in the B band were found to be in good agreement with those resulting from V band (disk + nucleus model); the values found for the corresponding parameters in the bulge + nucleus model fitted to the i and z bands were consistent, too. For these parameters, we were able to fix/identify new guesses *common to the four bands* for all the sources.
- In some cases the position angle of the disk found in the B band was strongly different for the value from the V band; a similar inconsistency was found for the position angle of the bulge derived in the i and z bands. Objects for which we were unable to establish a common value for the disk and/or the bulge position angle(s), were subjected to an additional run of GALFIT in the following step.

2) In the second step, morphological parameters were refined assuming the three components (nucleus, bulge and disk) in all the bands.

- Centers and radii found during the first step were used as new guesses. The centers of the three components were constrained to differ at most by ± 0.1 pixel.
- We fixed b/a to the values obtained in the first step.
- If PA was not well determined in the previous step, we re-runned GALFIT constraining the disk PA to be within ± 2 deg of the bulge parameter; then, we fixed PA to the values obtained in the previous run of GALFIT or in the first step.

At the end of this step, we were able to fix for the three components all the parameters (*i.e.*, position angles, axis ratios, centers and radii) but the four magnitudes.

3) A final run of GALFIT provided the magnitudes associated to each component; centers, radii, PA and b/a were fixed to the values found in the previous step. For each component, they were assumed to be the same in all bands. Only the total fluxes of all the components are left free and derived in this last step.

Results of the analysis are reported in Table I 4a and Table I 4b, for sources

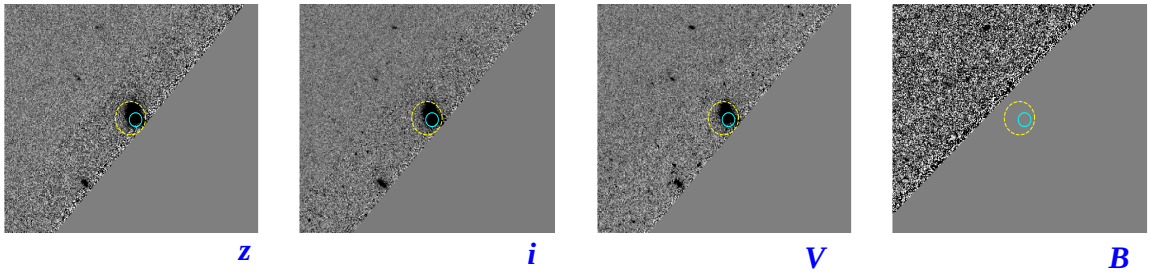

Figure I 9 ACS images in the four bands for a typical object rejected due to bad cutouts. We can clearly see the presence of regions with low S/N and the too small region with good quality data near the source (in this case, due to the source location near the edge of the GOODS field). Moreover, the B-band image shows that the coverage in the four ACS filters could be slightly different. Cyan and yellow circles mark the errors on the optical and X-ray positions, respectively.

in CDF-N and CDF-S, respectively: magnitudes of the nucleus - from column (2) to column (5); of the disk - from column (6) to column (9); and of the bulge component - from column (10) to column (13).

The associated errors were evaluated as follows: considering the image in a single filter, we fixed all the parameters except for the three magnitudes; to determine the range of variability for the magnitude of one component, we increased the magnitude by a value Δ mag in steps of 0.05 mag and perform a new fit with the two other magnitudes as free parameters until the variation of χ^2 with respect to the best fit value is $\Delta\chi^2 = 1$ (68% confidence level). For each source, we repeated this procedure for each component in each passband.

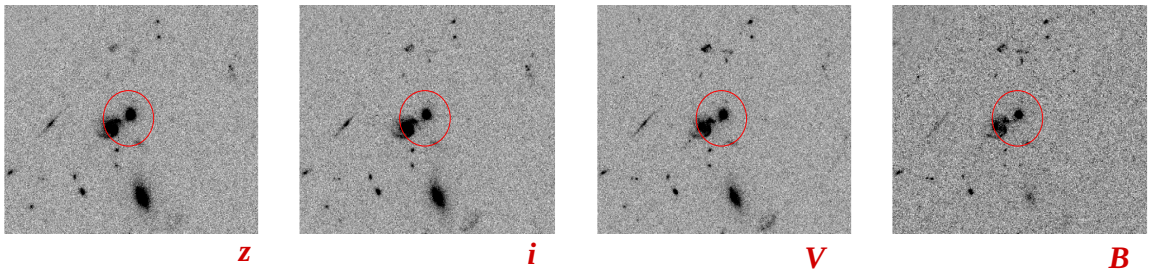

Figure I 10 As described in the text, we defined a source "not isolated" if another object was present within a projected radius of $2''$ (*i.e.*, $\sim$ 13 kpc at the mean redshift of sources in SAMPLE B), marked by the red circle in this representative case.

Due to the number of free parameters in this three-components decomposition, we

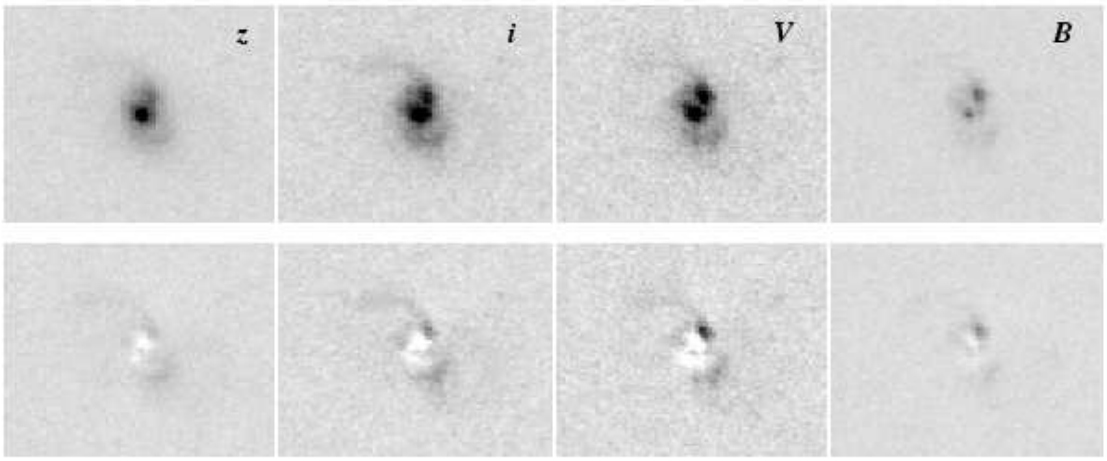

Figure I 11 Result of the analysis for a typical case (ID 16, CDF-S; $z = 0.839$). Original images in the four bands (*upper panels*) and residuals after subtracting the final model from the original images (*lower panels*).

required the same quality of data in a region of at least 60 pixels centered on the source. In addition, we required that *all* the four images meet this requirement in order to perform the analysis. For a number of sources in the regions target of the survey GOODS, the quality of one or more ACS images is significantly below average, *e.g.*, due to the source location near the edge of the GOODS field; in the construction of the SAMPLE A we rejected the objects for which these requirements are not satisfied [step 7), see Sect. I 1; columns (11) and (12) in Table I 2]. In Fig I 9 we present an object rejected because of bad quality data. It is evident that the conditions leading to the exclusion of the source are totally independent on its optical flux; this is reassuring and supports the idea that we are not introducing a bias against optically faint objects.

The same above-mentioned reason induced us to discard sources showing a nearby companion regardless whether they are really interacting or there is only a projection effect [step 8), see Sect. I 1; columns (13) and (14) in Table I 2]; a typical example is shown in Fig. I 10.

In Fig. I 11 we show as an example the result of the decomposition in a typical case (ID 16, CDF-S; $z = 0.839$). The residuals after subtracting the final model (*lower panels*) from the original images (*upper panels*) in the four bands show that the object is well modelled, apart from the residuals tracing the spiral arms (not accounted for in the applied galaxy model) and some particularly intense spots of emission. Xilouris & Papadakis (2002) studied the morphology of the central region of a sample of nearby Seyfert and LINERS, as well as of a control sample of normal galaxies, finding similar residuals. By comparing

the result of modeling active and inactive galaxies, the authors note that the AGNs show nuclear structures not reproduced by the model; these features are not present in modelized inactive galaxies.

I 3 Reliability of the deconvolution

The project we are dealing with has admittedly quite ambitious aims: our goal is to recover the nuclear properties for a sample of X-ray selected AGNs, performing a galaxy decomposition whose complexity is enhanced by the number of free parameters and by the use of images in several bands (see Sect. I 2). Therefore the reliability of the analysis must be carefully evaluated.

First, we considered how much robust the fit is. Due to the complexity of the applied model, the χ^2 identifying our solution could correspond to a *relative* minimum; furthermore, due to the high number of parameters involved, if we consider the space of the whole set of parameters it might even happen that no *absolute* minimum can be found. On the other hand, the core of the implemented best fitting procedure is to iteratively fix some parameters, on the basis of physical constraints. As a consequence, we think that the minimum found at the end of the analysis corresponds to the *physical* solution.

For all the sources the fit requires the presence of a bulge and a nucleus; in five cases, the disk component is not required. In a few cases, the result seemed to suggest that a simple two-component model fit would work as well. We addressed this issue, repeating the fit with only two components in the most extreme cases; the fit got worse, without a significant change in the magnitudes of the remaining components.

Deriving correctly the parameters of the bulge component is a fundamental task not only in the estimate of the nuclear contribution, but also in determining the black hole masses (see Sect I 4). In this context, the ability of deriving realistic scale lengths for the host component is an important issue, in particular taking into account the distance of the sources. Usually, both the deconvolution of images or observed profile (see Fig. 4 in Fasano et al. 2002) and the best-fitting of models convolved with the PSF (see Figs. 4 and 14 in Simard et al. 2002 for GIM2D) are reliable up to scale lengths $R_b \sim$FWHM of the PSF for the bulge and $R_d \sim 0.5\times$FWHM for the disk. We can assume that the limits of reliability are similar also in the case of GALFIT (for which similar simulations are not reported; Simmons et al. 2006, in preparation is dealing with this issue, containing ~ 50000 simulated galaxies). With this assumption, we did not find objects whose characteristic

Table I 4a. Two dimensional image fitting magnitudes - CDF-N.

ID	Nucleus				Disk				Bulge			
...	z	i	V	B	z	i	V	B	z	i	V	B
(1)	(2)	(3)	(4)	(5)	(6)	(7)	(8)	(9)	(10)	(11)	(12)	(13)
1	21.66±0.20	21.81±0.22	21.72±0.21	22.02±0.28	–	–	–	–	20.52±0.21	20.81±0.22	22.32±0.24	25.52±0.25
2	25.57±0.38	25.81±0.41	26.00±0.41	26.16±0.43	22.84±0.30	23.22±0.31	24.42±0.33	25.62±0.34	21.71±0.26	22.43±0.27	23.81±0.28	26.91±0.36
3	26.66±0.40	27.07±0.42	27.83±0.41	28.85±0.50	23.90±0.30	24.25±0.31	25.32±0.34	26.19±0.36	23.15±0.27	23.61±0.28	25.63±0.30	30.25±0.35
4	25.82±0.40	26.12±0.41	26.87±0.41	27.56±0.43	22.90±0.36	23.11±0.37	23.93±0.38	24.70±0.41	21.72±0.20	22.13±0.22	23.67±0.24	27.08±0.24
5	27.67±0.42	27.86±0.45	28.31±0.44	28.10±0.48	22.25±0.26	22.26±0.26	23.25±0.27	24.26±0.28	22.63±0.22	23.49±0.23	24.76±0.25	27.35±0.29
6	24.59±0.36	24.85±0.36	25.56±0.38	26.10±0.41	21.78±0.22	22.01±0.23	23.03±0.26	23.96±0.26	21.58±0.28	22.24±0.29	24.27±0.28	26.74±0.31
7	24.43±0.35	24.21±0.37	24.53±0.37	25.93±0.39	21.55±0.21	22.18±0.24	23.17±0.23	24.15±0.25	21.66±0.32	22.68±0.35	24.50±0.34	26.85±0.37
8	25.83±0.36	26.01±0.35	26.54±0.37	26.94±0.38	23.00±0.33	23.82±0.34	25.41±0.34	26.58±0.35	22.01±0.31	22.87±0.32	24.94±0.36	29.01±0.37
9	23.93±0.31	24.23±0.33	23.98±0.34	24.04±0.36	21.47±0.24	22.01±0.25	22.93±0.25	23.75±0.26	20.98±0.26	21.26±0.26	22.85±0.28	26.05±0.30
10	21.58±0.22	21.74±0.23	21.32±0.22	21.34±0.25	21.86±0.23	21.93±0.24	22.59±0.26	23.02±0.28	19.80±0.20	20.08±0.21	21.29±0.22	24.02±0.24
11	24.61±0.38	25.17±0.38	26.89±0.40	28.21±0.43	–	–	–	–	23.25±0.21	23.98±0.22	25.41±0.24	30.75±0.28
12	24.52±0.38	24.55±0.37	25.09±0.39	26.01±0.40	22.11±0.28	22.73±0.31	23.79±0.33	24.09±0.34	21.83±0.28	22.67±0.30	24.05±0.35	26.70±0.38
13	26.52±0.40	26.08±0.41	26.25±0.41	26.14±0.43	24.33±0.20	24.81±0.22	25.40±0.24	25.50±0.24	25.21±0.36	25.80±0.37	26.81±0.38	29.30±0.41
14	24.27±0.33	23.70±0.33	23.93±0.32	24.65±0.35	21.46±0.24	21.93±0.24	22.89±0.25	23.30±0.27	21.01±0.26	21.66±0.27	23.17±0.32	26.83±0.33
15	24.57±0.38	24.88±0.37	25.12±0.39	25.43±0.40	22.73±0.31	22.97±0.31	24.63±0.33	25.83±0.36	20.87±0.28	21.74±0.30	23.63±0.31	26.31±0.35

Note. — Errors are quoted at a 68% of declared confidence level (see text for details).

Col. (1): Source identification number.

Col. (2) − Col. (5): Total magnitude (not corrected for Galactic extinction) of the *PSF* component in the HST filters z, i, V and B respectively .

Col. (6) − Col. (9): Total magnitude (not corrected for Galactic extinction) of the *exponential* component in the HST filters z, i, V and B respectively.

Col. (10) − Col. (13): Total magnitude (not corrected for Galactic extinction) of the *DeVaucouleur* component in the HST filters z, i, V and B respectively.

Table I 4b. Two dimensional image fitting magnitudes - CDF-S.

ID	Nucleus				Disk				Bulge			
...	z	i	V	B	z	i	V	B	z	i	V	B
(1)	(2)	(3)	(4)	(5)	(6)	(7)	(8)	(9)	(10)	(11)	(12)	(13)
16	23.85±0.35	24.89±0.35	25.18±0.36	25.20±0.36	22.40±0.33	22.68±0.33	23.63±0.34	24.17±0.36	22.74±0.32	23.51±0.33	24.91±0.36	27.87±0.38
17	25.04±0.40	25.34±0.41	25.63±0.43	25.84±0.45	22.86±0.34	23.19±0.35	23.68±0.35	24.58±0.36	21.76±0.21	21.98±0.24	23.61±0.28	25.90±0.30
18	18.96±0.22	19.10±0.24	19.25±0.26	19.36±0.26	–	–	–	–	23.18±0.32	24.30±0.32	26.02±0.35	28.68±0.35
19	25.29±0.38	25.16±0.40	25.51±0.43	26.04±0.46	22.11±0.28	22.74±0.29	23.66±0.31	24.78±0.31	22.31±0.31	22.64±0.32	24.47±0.33	27.59±0.35
20	23.45±0.33	23.62±0.34	23.88±0.36	24.57±0.36	21.93±0.26	22.32±0.27	23.48±0.27	24.04±0.28	21.86±0.29	22.34±0.29	23.76±0.30	26.52±0.32
21	23.47±0.34	23.60±0.35	24.18±0.35	24.36±0.37	21.81±0.25	22.44±0.25	23.32±0.27	24.69±0.28	20.52±0.20	20.92±0.21	22.23±0.21	25.10±0.23
22	25.82±0.39	25.67±0.39	26.19±0.41	27.42±0.43	24.56±0.35	24.86±0.36	26.05±0.37	27.67±0.39	24.02±0.28	24.23±0.30	26.10±0.32	27.91±0.35
23	23.02±0.35	22.88±0.34	23.59±0.35	23.57±0.38	20.90±0.23	21.33±0.24	22.08±0.26	24.38±0.28	22.21±0.30	23.05±0.32	24.31±0.33	26.56±0.33
24	25.41±0.38	25.48±0.38	26.14±0.39	26.67±0.42	22.59±0.30	23.30±0.30	24.18±0.32	25.35±0.34	22.16±0.24	22.64±0.24	23.99±0.26	27.04±0.28
25	25.54±0.39	25.96±0.38	25.66±0.40	25.83±0.43	23.26±0.34	23.37±0.35	24.61±0.37	24.57±0.38	21.72±0.19	21.85±0.20	22.97±0.20	25.39±0.22
26	25.97±0.40	25.02±0.41	26.11±0.41	25.92±0.44	21.18±0.23	21.64±0.24	22.71±0.26	23.84±0.27	19.85±0.22	20.27±0.24	21.60±0.25	24.05±0.27
27	26.01±0.38	26.21±0.39	26.47±0.39	27.20±0.41	24.02±0.35	24.57±0.38	25.09±0.38	26.60±0.39	22.25±0.28	22.89±0.30	24.84±0.30	27.46±0.32
28	25.56±0.39	25.72±0.40	25.91±0.42	26.60±0.44	22.20±0.30	22.80±0.30	23.76±0.31	24.67±0.32	21.81±0.27	22.27±0.28	24.01±0.31	26.65±0.33
29	25.77±0.33	25.58±0.35	25.52±0.37	25.62±0.38	–	–	–	–	26.85±0.37	27.34±0.38	29.06±0.38	30.58±0.39
30	25.76±0.35	26.29±0.33	25.84±0.34	26.12±0.34	–	–	–	–	24.62±0.19	25.04±0.20	26.49±0.23	28.01±0.26
31	26.68±0.40	26.51±0.40	27.01±0.41	27.57±0.42	23.27±0.34	23.11±0.34	23.37±0.36	24.16±0.36	22.81±0.25	23.31±0.26	25.06±0.28	27.04±0.30
32	24.92±0.37	25.80±0.38	25.94±0.37	26.54±0.40	21.35±0.23	21.89±0.23	22.64±0.25	23.40±0.27	21.91±0.28	22.14±0.28	23.94±0.29	26.80±0.30
33	24.73±0.37	24.39±0.37	24.61±0.39	25.24±0.40	22.17±0.30	22.66±0.30	23.99±0.33	25.05±0.34	21.58±0.25	21.98±0.26	23.41±0.26	27.10±0.29
34	24.43±0.37	25.35±0.37	26.01±0.39	27.83±0.40	22.50±0.25	23.11±0.26	24.02±0.26	24.75±0.27	22.91±0.30	23.67±0.30	25.77±0.33	28.09±0.34

Note. — Errors are quoted at a 68% of declared confidence level (see text for details).

Col. (1): Source identification number.

Col. (2) − Col. (5): Total magnitude (not corrected for Galactic extinction) of the *PSF* component in the HST filters z, i, V and B respectively .

Col. (6) − Col. (9): Total magnitude (not corrected for Galactic extinction) of the *exponential* component in the HST filters z, i, V and B respectively.

Col. (10) − Col. (13): Total magnitude (not corrected for Galactic extinction) of the *DeVaucouleur* component in the HST filters z, i, V and B respectively.

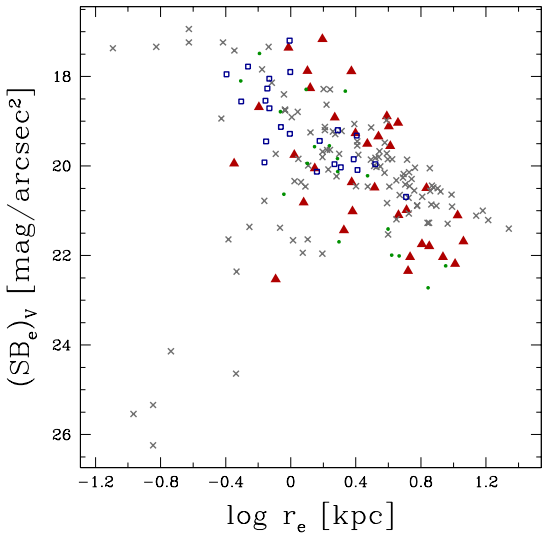

Figure I 12 Average surface brightness within the effective radius in the V-band (Johnson magnitude) vs. the effective radius. The distribution found for the analysed sources (red triangles) is in good agreement with that of local elliptical galaxies and bulges studied by Bender et al. (1992; grey crosses in the figure). The same region in the $SB_{\rm e}$–$r_{\rm e}$ plane is occupied by the bulges of Seyfert galaxies, as determined by Granato et al. (1993; green dots in the figure), as well as by a sample of early-type galaxies at higher redshift (see Fasano et al. 1998; blue open squares).

radii resulting from our analysis are really critical.

We have a confirmation of the identification of real bulges in the deconvolution from the agreement between our results with the fundamental plane found for elliptical galaxies and bulges. Indeed, we checked that the relation between the effective radius $r_{\rm e}$ and the surface brightness within it, $SB_{\rm e}$, is consistent with the one derived for local samples. Studies of galaxies hosting active nuclei have shown that they seem to lie on the same fundamental plane as normal early-type galaxies, being statistically consistent with the Kormendy relation for normal elliptical galaxies (see, *e.g.*, **?**Woo et al. 2004). The surface brightness for each bulge hosting an X-ray selected AGNs has been derived from the result of the decomposition described in Sect. I 2 (with a K-correction applied to convert the observed i-band AB magnitudes in rest-frame V-band Johnson magnitudes). In particular from Fig. I 12 we can see that the bulges derived with our analysis (red triangles) are distributed in the $r_{\rm e}$–$SB_{\rm e}$ plane as the sample of nearby elliptical galaxies and bulges studied by Bender et al. (1992), converted in the V-band assuming $B - V = 0.96$ and

corrected for the different cosmology adopted (grey crosses in the figure). It is interesting to note that the same region of the plane is occupied by the 18 bulges of local Seyfert 1 and Seyfert 1.5 galaxies observed in the V-band by Granato et al. (1993), corrected for the different cosmology adopted (green dots in the figure). We also find a good agreement with the distribution reported by Fasano et al. (1998) for a sample of 23 early–type galaxies with spectroscopic redshift $z \lesssim 3.4$, with K- and evolutionary corrections applied (see their Fig. 6) and corrected for the different cosmology adopted (blue open squares in the figure).

Since the analysis was carried out *separately* in the four bands, no *a priori* constraint was imposed on the measured spectral energy distributions (SEDs) for the individual components (bulge, disk and nucleus). To test the goodness of our analysis we compared the resulting SEDs with suitable templates. In doing this, it is extremely important to recall that a number of factors could concur to give differences between the observed emission and generic templates. First, the reddening may significantly affect the observed SEDs. Intrinsic nuclear emission in the UV and optical ranges may be altered by dust absorption from circumnuclear and/or more diffuse component(s). The latter is also relevant for the galactic components, particularly for the disc, which is composed by younger and bluer stars. The bulge component is expected to be less affected by absorption.

SED templates for the bulge and disk components were derived by using a set of Single Stellar Population (SSP) SEDs[5]. To describe the bulge, first we selected a template representing the "typical" elliptical galaxy at $z \sim 0$. Afterward, we proceeded as follows. To take into account the well-known metallicity-age degeneracy, we assumed two initial chemical compositions of the evolutionary sequences: $[Z = 0.02, Y = 0.28]$ and $[Z = 0.05, Y = 0.352]$, where Z is the mass fraction of heavy elements in the interstellar gas, and Y is the fraction by mass of helium (the solar values are $Z_\odot = 0.02$ and $Y_\odot = 0.21$). For both these metallicity mixes, integrated spectra of SSP of different ages were compared with the mean empirical spectrum obtained from the observed spectra of NGC 1399 and NGC 1404 (A. Bressan, priv. comm.). In this way, we found the age which provides the best agreement: 10 Gyr for $Z = 0.05$, and 11 Gyr for $Z = 0.02$. These ages were fixed as epoch of formation for all the galaxies in our sample, in order to select the template to which to compare the SED derived from the decomposition: for the two metallicities, once the the epoch of formation has been fixed, we compute the integrated SSP spectrum at the redshift of each analysed source.

For the disk, the SSPs used were the same as for the bulge component. In this

[5]Available at `http://web.pd.astro.it/granato/grasil/SSP/ssp.html`; see also Silva et al. 1998.

case we assumed younger templates, in order to simulate a continuous star formation during the disk lifetime. Finally, to check the nuclear optical SED, we adopted the QSO template spectrum of Cristiani & Vio (1990) down to 538 Å, modified as described by Cristiani et al. (2004) and Monaco & Fontanot (2005), and extrapolated to 300 Å using $f_\nu \propto \nu^{-1.75}$ (following Risaliti & Elvis 2004).

In Fig. I 13, we show the comparison of the decomposed SEDs with the three templates and the magnitudes for the whole galaxy in all the available bands for a generic case (ID 16, CDF-S; $z = 0.839$). For the bulge and the disk components the observed SEDs are always in good agreement with the template, without invoking large correction for absorption even for the latter component.

Concerning the nuclei, the agreement of the observed SEDs with the template is

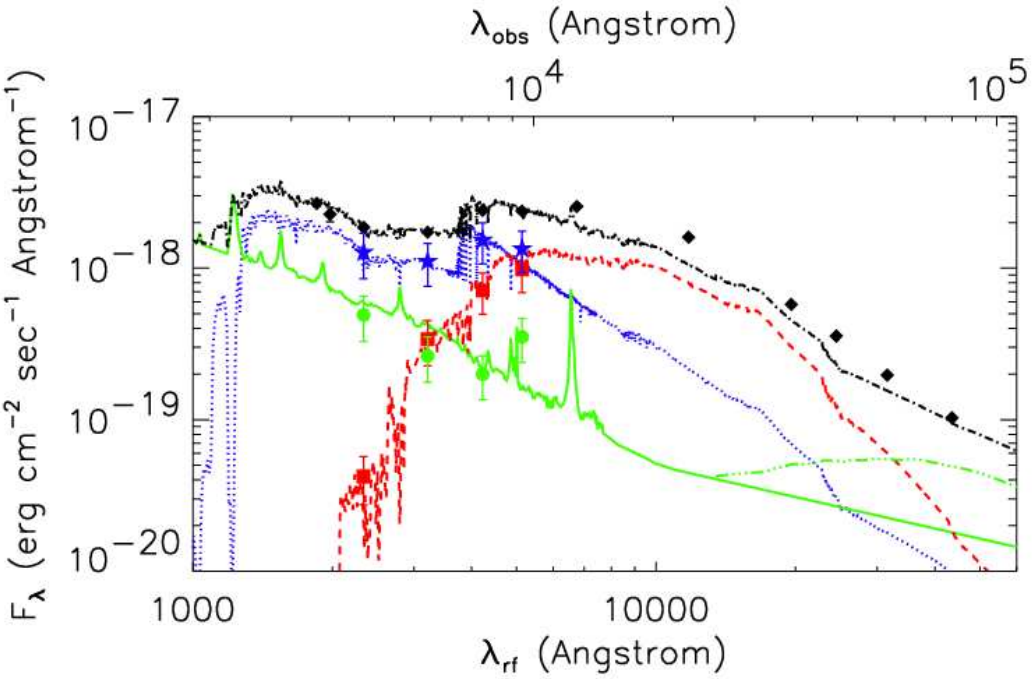

Figure I 13 Fit of the templates (bulge: red dashed line, disk: blue dotted line, and nucleus: green solid line) to the decomposed optical magnitudes (ID 16, CDF-S; $z = 0.839$) for the different components (bulge: red squares, disk: blue stars, and nucleus: green circles), and comparison of the sum of the templates (dot-dashed line) with the fluxes observed from the whole galaxy in all the available bands (diamonds); a contribution from a circumnuclear torus is assumed to account for *Spitzer* data (green long-dashed line; adapted from the mean SED of a typical Seyfert 1 reported in Granato & Danese 1994).

good for 70% of the analysed objects; in the remaining 10 cases the emission in the V and in particular in the B bands is lower than expected from the SED normalized to the i and z-bands. Of course this results strongly suggests the presence of significant obscuration. The existence of significant amount of obscuring matter is well supported by the high column density, $N_{\rm H} \geq 10^{22}$ cm^{-2}, inferred from their X-ray emission (see the discussion in Sect. I 4; the $N_{\rm H}$ values for the whole sample are reported in Table I 7).

Fluxes from the decomposition and templates were also compared to the magnitudes for the whole galaxy as retrieved from the GOODS catalogue, as well as to the magnitudes in the IR and U-band, when available (see Sect. 3.1). In particular, the *Spitzer* data used (for the CDF-S only) were analysed by Grazian et al. (2006). For the U-band and *Spitzer* data the angular resolution is not good enough to let us to make a morphological decomposition. Nevertheless we can obtain important indications by comparing the observed total fluxes with the sum of the templates of bulge, disk and nucleus, normalized to the decomposed magnitudes. In particular, we are able to reproduce the *Spitzer* data by assuming a contribution from a circumnuclear torus, as observed in a typical Seyfert 1 galaxy (see Granato & Danese 1994).

Finally, the nuclear [host] component could dominate the optical images at all wavelengths, overwhelming the emission from the other components. Whenever this happens, the galactic [nuclear] component, even if still significant in the fit, could be not tightly constrained. Underestimating the magnitudes for the bulge or the nucleus may affect the determination of the nuclear properties (see Sect. I 4). We identified similar situations looking at the luminosity ratio of the different components resulting from the decomposition (these ratios are reported in Table I 5a and Table I 5b for sources in the CDF-N and the CDF-S, respectively). As described in the following, in such cases we could only provide upper limits for the magnitudes of the fainter component; constraints imposed by the observations in the IR range for the flux expected on the basis of this reconstruction prevented us from *overestimating* this fainter component in the cases of nucleus-dominated objects.

In sources dominated by the AGN (two objects in the present sample) we can only set upper limits to the host component by minimizing the nuclear contribution (which is well constrained). We put a threshold on the nucleus–to–total luminosity ratio N/T in the z band [column (11) in Table I 5a and Table I 5b] of $N/T(z) = 0.2$ as a fiducial value to identify the galaxies affected by this problem. For the two analysed sources satisfying this criterion we proceeded as follows.

Table I 5a. Ratio of the luminosity of the different components obtained from the two dimensional image fitting - CDF-N.

ID	Redshift	Bulge/Gal				Nucleus/Bulge				Nucleus/Total			
...	...	z	i	V	B	z	i	V	B	z	i	V	B
(1)	(2)	(3)	(4)	(5)	(6)	(7)	(8)	(9)	(10)	(11)	(12)	(13)	(14)
1	0.679	1.000	1.000	1.000	1.000	0.349	0.396	1.739	25.26	0.115	0.124	0.241	0.325
2	0.747	0.739	0.675	0.636	0.234	0.029	0.045	0.133	1.986	0.020	0.028	0.068	0.194
3	0.762	0.666	0.643	0.428	0.022	0.040	0.041	0.132	3.631	0.024	0.025	0.048	0.065
4	0.680	0.747	0.712	0.560	0.101	0.023	0.025	0.052	0.643	0.016	0.017	0.027	0.054
5	0.555	0.413	0.245	0.200	0.055	0.010	0.018	0.038	0.501	0.004	0.004	0.007	0.025
6	0.857	0.546	0.447	0.242	0.072	0.063	0.091	0.305	1.809	0.031	0.036	0.060	0.093
7	0.961	0.476	0.386	0.227	0.077	0.078	0.245	0.972	2.323	0.033	0.074	0.133	0.116
8	0.955	0.714	0.705	0.605	0.097	0.030	0.055	0.229	6.742	0.020	0.035	0.098	0.221
9	0.678	0.610	0.667	0.518	0.107	0.066	0.065	0.354	6.362	0.036	0.038	0.118	0.224
10	0.514	0.870	0.846	0.768	0.285	0.194	0.218	0.967	11.805	0.112	0.119	0.230	0.303
11	0.935	1.000	1.000	1.000	1.000	0.286	0.336	0.257	10.365	0.100	0.112	0.093	0.313
12	0.978	0.565	0.515	0.441	0.083	0.084	0.177	0.383	1.905	0.041	0.072	0.112	0.107
13	0.474	0.309	0.287	0.214	0.029	0.298	0.774	1.676	18.345	0.072	0.133	0.173	0.205
14	0.839	0.602	0.560	0.436	0.037	0.050	0.153	0.495	7.399	0.027	0.068	0.131	0.151
15	0.838	0.847	0.756	0.715	0.391	0.033	0.056	0.254	2.254	0.026	0.038	0.118	0.242

Note. —
Col. (1): Source identification number.
Col. (2): Redshift for the optical counterpart, as in Table I 2.
Col. (3) − Col. (6): Bulge–to–galaxy ratio in the four bands.
Col. (7) − Col. (10): Nucleus–to–bulge ratio in the four bands.
Col. (11) − Col. (14): Nucleus–to–total ratio in the four bands.

Table I 5b. Ratio of the luminosity of the different components obtained from the two dimensional image fitting - CDF-S.

ID	Redshift	Bulge/Gal				Nucleus/Bulge				Nucleus/Total			
...	...	z	i	V	B	z	i	V	B	z	i	V	B
(1)	(2)	(3)	(4)	(5)	(6)	(7)	(8)	(9)	(10)	(11)	(12)	(13)	(14)
16	0.839	0.422	0.318	0.235	0.032	0.360	0.280	0.777	11.665	0.104	0.070	0.118	0.176
17	0.668	0.734	0.753	0.516	0.229	0.049	0.045	0.156	1.057	0.032	0.031	0.065	0.140
18	0.734	1.000	1.000	1.000	1.000	48.591	119.994	511.588	5323.043	0.329	0.331	0.333	0.333
19	0.734	0.454	0.523	0.322	0.070	0.064	0.098	0.384	4.169	0.027	0.044	0.090	0.155
20	0.733	0.516	0.495	0.436	0.092	0.231	0.308	0.895	6.026	0.088	0.105	0.180	0.209
21	0.534	0.766	0.802	0.732	0.407	0.066	0.085	0.166	1.977	0.044	0.056	0.089	0.236
22	0.670	0.622	0.641	0.488	0.445	0.191	0.265	0.920	1.570	0.087	0.113	0.191	0.226
23	0.569	0.231	0.170	0.114	0.118	0.474	1.170	1.941	15.785	0.083	0.125	0.133	0.283
24	0.604	0.599	0.649	0.544	0.174	0.050	0.073	0.138	1.404	0.027	0.041	0.061	0.141
25	0.545	0.805	0.802	0.818	0.318	0.030	0.023	0.085	0.668	0.022	0.017	0.057	0.130
26	0.664	0.773	0.780	0.736	0.450	0.004	0.013	0.016	0.181	0.003	0.010	0.011	0.065
27	0.734	0.836	0.825	0.557	0.310	0.031	0.047	0.223	1.273	0.024	0.035	0.091	0.181
28	0.735	0.588	0.619	0.441	0.139	0.032	0.042	0.175	1.047	0.018	0.024	0.063	0.101
29	0.679	1.000	1.000	1.000	1.000	2.723	5.054	26.065	96.235	0.268	0.294	0.325	0.331
30	0.481	1.000	1.000	1.000	1.000	0.348	0.318	1.813	5.721	0.114	0.108	0.244	0.299
31	0.549	0.605	0.454	0.175	0.066	0.028	0.052	0.165	0.616	0.016	0.022	0.027	0.036
32	0.735	0.374	0.443	0.233	0.042	0.063	0.034	0.158	1.267	0.022	0.015	0.033	0.046
33	0.668	0.634	0.652	0.630	0.132	0.055	0.107	0.331	5.516	0.031	0.058	0.128	0.229
34	0.910	0.407	0.375	0.166	0.044	0.247	0.212	0.801	1.275	0.077	0.064	0.095	0.048

Note. —
Col. (1): Source identification number.
Col. (2): Redshift for the optical counterpart, as in Table I 2.
Col. (3) – Col. (6): Bulge–to–galaxy ratio in the four bands.
Col. (7) – Col. (10): Nucleus–to–bulge ratio in the four bands.
Col. (11) – Col. (14): Nucleus–to–total ratio in the four bands.

- We assumed for the QSO template a normalization 2σ lower than the best fit (where the uncertainties are evaluated as described in Sect. I 2), determining a minimum value for the nuclear magnitudes in the four bands.

- Assuming these nuclear magnitudes, we rescaled the bulge component[6] until the observed value of the total flux is reached.

- Finally, we compared the new galaxy reconstruction (*i.e.*, the sum of the templates of bulge and nucleus rescaled) with the emission in the IR bands, checking that the new estimate does not overpredict (at more than 2σ level) the emission at wavelengths greater than 1 μm.

For both sources we found that the bulge luminosity can increase up to a factor of 10 with respect to the result of the decomposition; we consider these values robust upper limits.

On the other hand, when the optical emission is dominated by the host galaxy components (bulge and/or disk, six objects), the nuclear contribution provided by GALFIT could be a lower limit to the actual one. We re-analysed separately the six sources with nucleus–to–total luminosity ratio in the V band $N/T(V) < 0.05$ [see Table I 5a and Table I 5b, column (13)]. Again, these are the detailed steps we followed.

- We assumed for bulge and disk templates a normalization 2σ lower than the best fit (where the uncertainties are evaluated as described in Sect. I 2), determining a minimum value for their magnitudes in the four bands.

- Upper limits to the nuclear magnitudes were then calculated imposing that the total (host plus nucleus) values are equal to the observed ones.

- We checked that the new estimate of the nucleus in the U-band was not higher (at more than 2σ level) than the observed flux.

Again, the results of this procedure are considered robust upper limits to the nuclear luminosity.

I 4 Recovering the nuclear properties

Disentangling the different galactic components via the two dimensional decomposition described in Sect. I 2 provided detailed information on the bulge and nuclear

[6] We note that for both the sources re-analysed the disk component is not required in the final fit, even if assumed in the initial analysis.

luminosity. This information was used to study the nuclear activity of the galaxies in our sample. In Sect. I 4.1 we present our derivation of the black hole mass, while the bolometric luminosity, evaluated from optical and X-ray nuclear luminosities, is discussed in Sect. I 4.2. In the figures showing our results in this section, as well as in Sect. I 5, we adopt the following color/shape code.

Red symbols: sources for which we are confident that the results from the morphological decomposition are reliable.

Yellow circles: nucleus–dominated sources

- Open symbols: values obtained from the decomposition.
- Filled symbols: values obtained assuming for the fainter component the more robust upper limits (see Sect. I 3).

Green squares: host–dominated sources

- Open symbols: values obtained from the decomposition.
- Filled symbols: values obtained assuming for the fainter component the more robust upper limits (see Sect. I 3).

I 4.1 Black Hole Masses

We exploited the observed local relationship between black hole mass and bulge component luminosity to obtain an estimate of the mass of the central compact object, starting from the absolute magnitudes of the bulge component (see Sect. 2). Several versions of this relation have been proposed with the bulge luminosity evaluated at electromagnetic bands ranging from B to K (see, *e.g.*, Kormendy & Gebhardt 2001; McLure & Dunlop 2002; Marconi & Hunt 2003).

In order to compute the black hole mass, we made the following assumptions: *i)* in this relation the absolute magnitude of the bulge strictly reflects the mass locked in old stars, $M_{\rm bulge}$: this is the quantity primarily related to the black hole mass; *ii)* the $M_{\rm bulge}$–$M_{\rm BH}$ relation is imprinted at high redshift.

The last claim is supported by the recent findings of Peng et al. (2006). They showed that, once allowing for passive evolution of the stellar population, the $M_{\rm BH}$–M_R

relations for 5 AGNs at $z \leq 1$ are compatible with the local relation. We note that their results on individual black hole masses for 4 QSOs at $z \approx 1$, derived through the virial theorem applied to the BLR, are uncertain by at least a factor of 3; moreover, the luminosities of the host spheroids are also affected by large systematic errors. Nevertheless the result is reassuring.

Another supporting evidence can be derived from the study by McLure & Dunlop (2002). They analyzed with the same technique a sample of 72 active galaxies (Seyferts and QSOs) at $z \lesssim 0.5$, and demonstrated that AGN host galaxies at these redshifts follow a relation between black hole mass and bulge luminosity consistent with that of local quiescent galaxies.

There are claims that the scaling relations between black hole mass and bulge parameters are subjects to a cosmic evolution (*e.g.*, Woo et al. 2006; but see also the discussion in Sect. 2); however, such a behaviour would produce black hole mass estimates only slightly higher than those presented in the following. On the other hand, it is hard to imagine how a significant independent evolution can lead to a $M_{\rm bulge}$–$M_{\rm BH}$ relation with a scatter as small as that reported, *e.g.*, by Ferrarese & Ford (2005).

When converted to $H_0 = 70$ km s^{-1} Mpc^{-1}, the relation between the total R-band magnitude of the bulge and the black hole mass, as reported in McLure & Dunlop (2002) for a sample of 20 inactive E-type galaxies at $z \sim 0$, is:

$$\log\left(\frac{M_{\rm BH}}{M_\odot}\right) = -0.50\,(\pm 0.03)\cdot M_R - 2.69\,(\pm 0.72) \qquad \text{(I.1)}$$

with a scatter of $\Delta \log(M_{\rm BH}) = 0.33$. As mentioned above, other versions of this fundamental relation are available in the recent literature.

It is worth noting that equation (I.1) has been derived using B-band and V-band magnitudes, translated to R-band assuming average colours $(B - R) = 1.57$ and $(V - R) = 0.61$. On the other hand, the relation presented by Marconi & Hunt (2003) exploits the K-band magnitudes and on average predicts black hole masses higher by about 0.3 dex at fixed luminosity. However, the difference could be ascribed to the uncertainty in evaluating the bulge component of spiral galaxies in their observed sample (Shankar et al. 2004). The relationship estimated by Kormendy & Gebhardt (2001), using B-band bulge luminosities, yields black hole masses at most by about 0.2 dex larger than those predicted on the basis of equation (I.1). In this work we have adopted the relation proposed by McLure & Dunlop (2002), since it yields conservative mass estimates. Hence, in the following it is worth recalling that our derived black hole masses could be a factor from 1.5

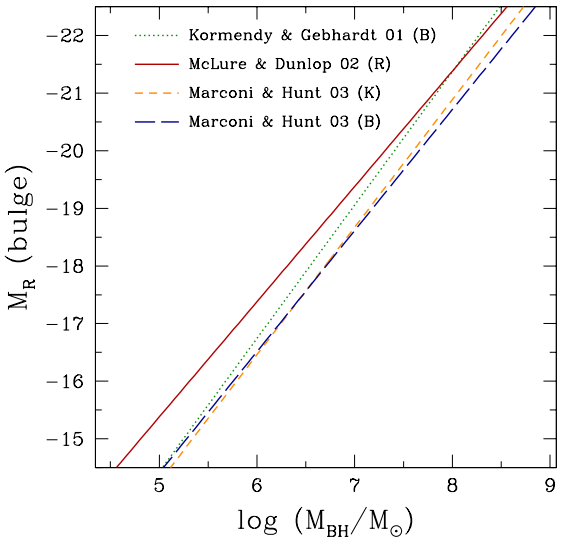

Figure I 14 Observing the bulge in different bands yields different relations between black hole mass and bulge magnitude. Here we summarized a number of these relations from the recent literature (references are given in the text). Apart from the one proposed by Kormendy & Gebhardt (2001), the main difference lies in their normalization, with McLure & Dunlop (2002) resulting in the lowest black hole mass.

to 2 higher, had we used the relationship proposed by Kormendy & Gebhardt (2001) or by Marconi & Hunt (2003). Correspondingly, the Eddington ratios would be lower by the same factor.

A graphical summary of the above discussion is shown in Fig. I 14, where we compare the black hole masses derived from the different relations. All these relation were corrected for the different cosmology used in the original papers; moreover, the original relationships were converted to the R-band assuming a colour $B - R = 1.57$ for those proposed by Kormendy & Gebhardt (2001) and Marconi & Hunt (2003, for a subsample observed in B-band). We adopted $R - K = 2.5$ for the relation of Marconi & Hunt (2003) obtained from observations in K-band.

To estimate the rest-frame R-band magnitude at $z \sim 0$ for the bulges in our sample, we started from the SSP SEDs normalized as described in Sect. I 3 and computed their passive evolution up to the present epoch[7]. The R-band magnitudes obtained by

[7]As a check, we evaluated also the black hole masses obtained from the relation for AGNs at higher redshift (see Table 3 in McLure & Dunlop 2002) using the rest-frame R-band magnitude at the redshift of each source (*i.e.*, *without evolution*); we found a systematic shift of the order of +0.18 dex with respect to the values reported in Table I 7.

using the two metallicities introduced in Sect. I 3 are very similar, within 0.1 mag for all the sources. As a consequence, we adopted the average from the two metallicities mix as our final R-band magnitudes; these averages as well as the black hole masses obtained from equation (I.1) are listed in Table I 7. The same fit was also carried out for sources dominated either by the nuclear component or by the host galaxy; however, in these cases we assumed for the bulge the magnitudes obtained as described in Sect. I 3. The corresponding upper or lower limit to the mass of the central black hole is reported as a second line in Table I 7 for each of these sources.

We estimated the error for the R-band magnitude of the bulge component by combining two contributions that differ in the choice of the template and its normalization.

- The uncertainties associated with the decomposed magnitudes propagate on to the best fit normalization of the elliptical template adopted in computing the R-band magnitudes:

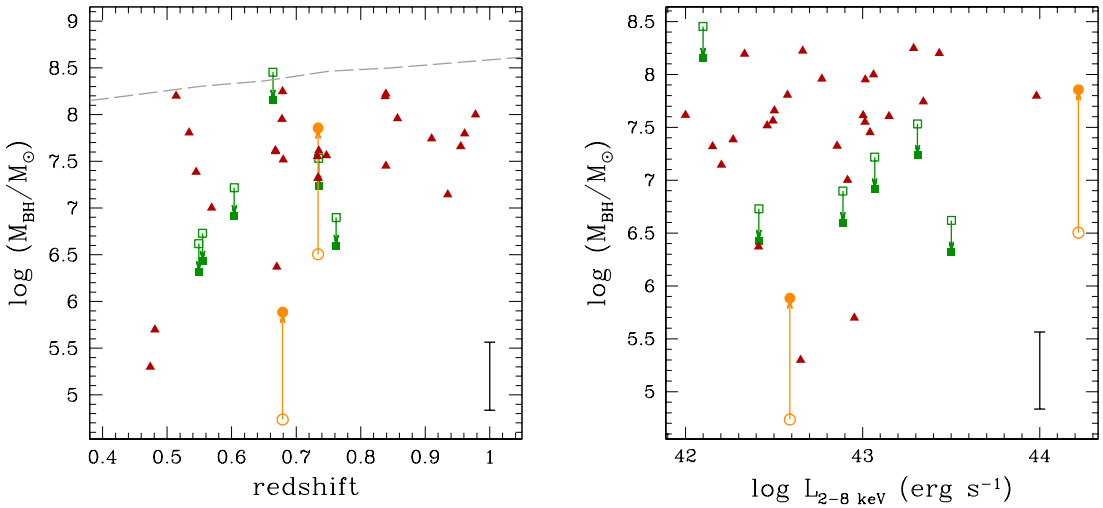

Figure I 15 Black hole masses versus redshift (*left panel*) and unabsorbed hard X-ray luminosity (*right panel*) for the analysed sample. Red triangles refer to sources for which we are confident that the results from the morphological decomposition are reliable. For nucleus–dominated or host–dominated sources (according to the criteria established in Sect. I 3) yellow circles and green squares (filled symbols) mark the upper limits to $M_{\rm BH}$ and $L_{\rm bol}$ respectively; open symbols connected to the previous ones mark the values obtained from the decomposition. Only mean error bars are reported to avoid clutter. As a comparison, we overplot to our distribution of masses versus redshift (*left panel*) the mean (within $\Delta z = 0.1$ bins) values found by McLure & Dunlop (2004) for their full Sloan Digital Sky Survey (*SDSS*) quasar sample (long-dashed line).

for each source, we repeated the fit changing the normalization of the template until $\Delta\chi^2 = 1$, and computed the R-band magnitudes corresponding to the minimum and maximum values of the normalization.

- The difference between the R-band magnitudes found by using two different metallicities for the SSPs (see Sect. I 3) was assumed as an estimate of the error induced by selecting these particular templates to represent a local inactive galaxy (*i.e.*, by choosing the two above-mentioned pairs age/metallicity).

The final errors were then propagated to give the uncertainties associated with the black hole masses, together with the scatter in equation (I.1); we note that this last factor always represents the dominant contribution.

Derived black hole masses for objects in our analyzed sample are shown in Fig. I 15 as a function of the redshift and of the unabsorbed hard X-ray luminosity. The masses are distributed over two decades, $2 \times 10^6 \leq M_{\rm BH} \leq 2.5 \times 10^8\ M_\odot$; only 3 out of 34 objects have $M_{\rm BH} \leq 10^6\ M_\odot$. AGNs at low redshift span the whole range in mass, while at the upper end of the redshift distribution only large ($M_{\rm BH} > 10^7\ M_\odot$) black hole masses are found (see Fig. I 15). We can devise no obvious selection effects able to explain this observed pattern. Thus, we advance the tentative working hypothesis that such a behaviour is an intrinsic property of the sample. Moreover, we did not see any correlation between the estimated bulge luminosity and the X-ray luminosity. As a consequence, no correlation was found also between black hole mass and X-ray luminosity.

I 4.2 Nuclear Bolometric Luminosities

Nuclear bolometric luminosities for all the objects in our sample are required to investigate the accretion rates powering these sources. We compared the X-ray flux, totally ascribed to the AGN, and the optical nuclear magnitudes (*i.e.*, the nuclear emission) to SEDs of active nuclei with different X-ray–to–optical ratios. In these SEDs, the high energy emission is described as a power law with photon index Γ. For the optical bands we adopted the QSO template spectrum described in Sect. I 3.

However, these SEDs (describing the emission of a *type 1* AGN) must be compared with the *intrinsic* nuclear emission, which in case of absorbed sources can be very different from the observed one. The problem was tackled starting from the X-ray spectral analysis and assuming the picture proposed by the Unified Model (see Sect. 1)

X-ray emission

- We adopted the intrinsic $N_{\rm H}$ quoted by Tozzi et al. (2006) for the CDF-S sources and we *de-absorbed* the X-ray flux. Since the analysis of CDF-N X-ray emission (Alexander et al. 2003) does not include an intrinsic absorption, we derive it from the hardness ratios and redshifts, assuming a mean photon index $\Gamma = 1.8$. As shown in Table I 7, only one object of the sample exhibits a hydrogen column density $N_{\rm H} \simeq 1.5 \times 10^{24}$ cm^{-2} (hence it might be a likely Compton-thick candidate.).

- We recovered the *intrinsic* X-ray luminosity normalizing a power-law spectrum having the same X-ray photon index of the source (for the CDF-S) or with Γ fixed to 1.8 (for the CDF-N) so that it matches the intrinsic X-ray flux.

Optical bands

- We compared the QSO template spectrum with the optical nuclear magnitudes, computing:

$$\chi^2_= \sum_{j=1}^{N_{\rm bands}} \left[\frac{F_{{\rm obs},j} - b \times F_{{\rm templ},j}}{\sigma_j} \right]^2$$

  where b is a normalization constant and $F_{{\rm obs},j}$, $F_{{\rm templ},j}$ are the observed and template fluxes; σ_j is the uncertainty of the observed flux; the subscript refers to a given optical band j.

- We normalized the QSO template with the value of b corresponding to the minimum value for χ^2, obtaining the optical contribution to the bolometric luminosity.

- If $N_{\rm H} > 10^{22}$ cm^{-2} the presence of dust in the central regions could affect seriously our estimate of nuclear magnitudes: this happens for about 2/3 of the analysed sources. In this case, rather than assuming a quite arbitrary correction factor, we preferred to ignore the fluxes in the B and V bands, where the effects of the absorption are more severe. Thus, for these sources only the i and z magnitudes were considered in the fit.

Bolometric properties: finally, we connected the power-law spectrum and the QSO template normalized as described above, to recover the X-ray–to–optical ratio, the bolometric luminosity of the AGN and the hard X-ray bolometric correction.

As outlined in Sect. I 3, the mid-IR fluxes detected by *Spitzer* for 18 of the southern objects analysed are well explained by the expected contribution from the dusty torus

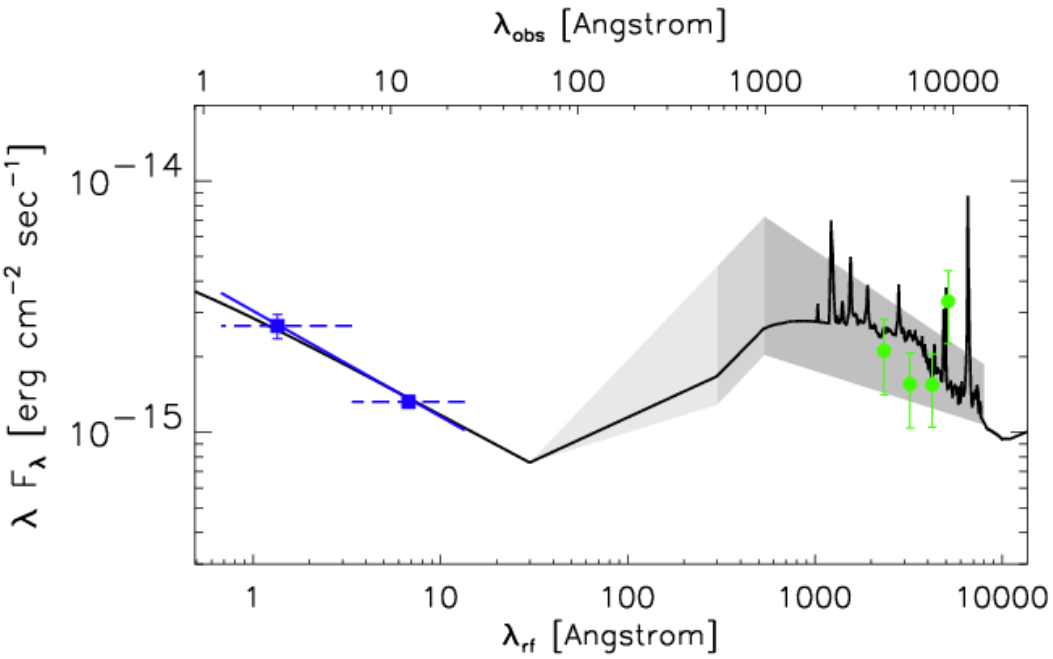

Figure I 16 Fit of the QSO template (solid line) to the nuclear SED (optical magnitudes, green circles; and X-ray flux, blue squares); grey areas represent the uncertainty in the optical emission, and the consequent uncertainty in the UV range (ID 16, CDF-S; $z = 0.839$).

around the nucleus. The addition of a torus component is needed when we compare the *observed data* (*Spitzer*) with the *intrinsic emission* (the QSO template). Indeed, in the latter we do not consider the effects of absorption, which in the IR band produces an increase of emission: we know that the torus emission is just the reradiation of a fraction of the "isotropic" radiation from the very nuclear region (see, *e.g.*, Granato & Danese 1994). Hence, when dealing with the task of computing the nuclear bolometric luminosity, the IR emission from the putative torus should not be included in the budget of bolometric emission for type 1 AGNs and not even for type 2 AGNs, when correction for absorption is done at shorter wavelengths, as in our case (thanks to the use of an unabsorbed QSO template). Fig. I 16 shows the result of the fit in the generic case, the source CDF-S ID 16 ($z = 0.839$).

We identified two possible sources of uncertainty in our estimate of the bolometric luminosity.

- The selection of only one spectral shape for the optical emission, common to all the sources, might cause a systematic error. Starting from a spectral shape $f_\lambda \propto \lambda^\alpha$,

we determined for each source the scatter in the optical luminosity due to a different choice in the slope (we used $\alpha = -1.37 \pm 0.25$, as found by Fontanot et al. 2006b averaging the rest-frame spectra of 215 QSO from the Sloan Digital Sky Survey, *SDSS*). The scatter, calculated assuming as a pivot the flux at the frequency corresponding to the i-band wavelength in the observed frame, results to be of the order of $\Delta \log L = 0.2$.

- Also in this case, the uncertainties associated with the decomposed magnitudes propagate on to the best fit normalization of the QSO template. To estimate this source of error we repeated the fit for each source changing the normalization of the template until $\Delta\chi^2 = 1$.

Bolometric luminosities with the estimated errors are shown in Table I 7. Their dependence on redshift and hard X-ray luminosity is shown in Fig. I 17. In host–dominated objects the nuclear flux provided by the decomposition could be underestimated. For these six sources, the same procedure has been applied also assuming as nuclear magnitudes the upper limits recovered as described in Sect. I 3. The corresponding upper limit to $L_{\rm bol}$

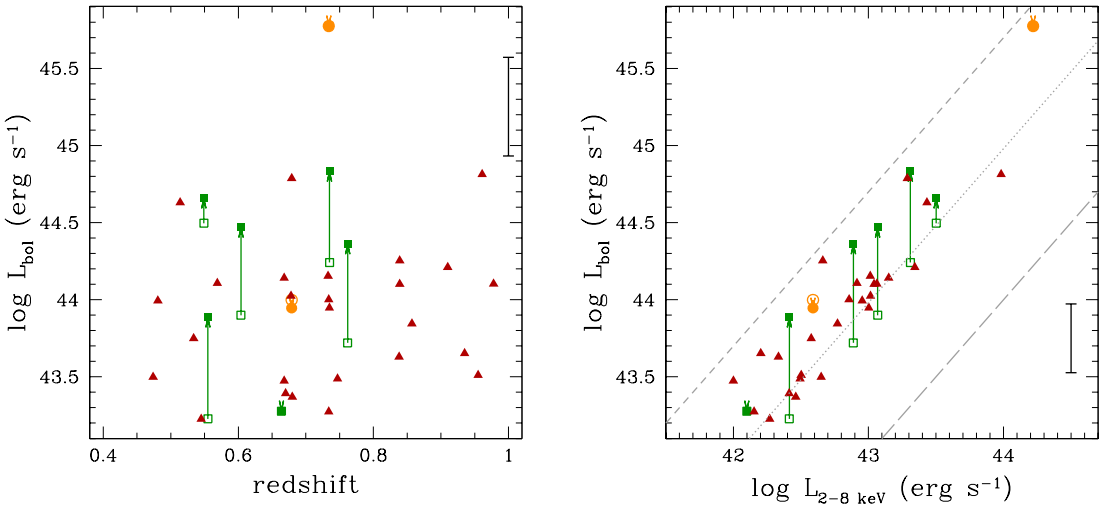

Figure I 17 Bolometric luminosities versus redshift (*left panel*) and unabsorbed hard X-ray luminosity (*right panel*) for the analysed sample. For the meaning of the symbols, see Fig. I 15 and the beginning of Sect. I 4. The dotted line in the $L_{\rm bol}$ vs $L_{\rm X}$ plot (*right panel*) represents the threshold $L_{\rm bol}/L_{\rm X} = 10$, while the dashed lines correspond to the "extreme" values for the X-ray bolometric correction reported in Sect. I 5. Only mean error bars are reported to avoid clutter. For the distribution of $L_{\rm bol}$ vs $L_{\rm X}$ (*right panel*), we plot the component of the error on $L_{\rm bol}$ that is independent from the error on $L_{\rm X}$.

is reported as a second line in Table I 7. While the upper limits of their optical nuclear luminosity may be a factor up to 200 larger than the decomposed ones, the bolometric upper limit is larger by factor of 10, at most. We found bolometric luminosities in the range $10^{43} \leq L_{\rm bol} \leq 10^{45}$ ergs s^{-1}, with only one exception (the source CDF-S ID 18, $L_{\rm bol} \simeq 5.9 \times 10^{45}$ ergs s^{-1}).

Fitting the templates to the nuclear SED we were able to characterize also the relative importance of the emission at different wavelengths in the bolometric output of each source. A detailed discussion about this topic is deferred to Sect. I 5; here we restrict ourself to note the relative importance of the high energy emission in these sources. The X-ray–to–optical ratios, defined as the slope of an hypothetical power law extending between 2500 Å and 1 keV ($\alpha_{\rm ox} = \log(L_{\nu\,[2500\,\text{Å}]}/L_{\nu\,[1\,\rm keV]})/\log(\nu\,[2500\,\text{Å}]/\nu\,[1\,\rm keV])$; see Zamorani et al. 1981), span the range $-1.4 \div -0.9$. The X-ray emission accounts for 15% of the whole energy emitted by the AGN: the X-ray bolometric corrections, $k_{\rm X} = L_{\rm bol}/L_{\rm X}$, span the range $6.8 \div 46.7$. This result is not completely surprising due to the initial X-ray selection of the sample. UV-luminosities, $\alpha_{\rm ox}$ and X-ray bolometric corrections are presented in Table I 6; for convenience, we report in the same table also the hard X-ray unabsorbed luminosities and the bolometric luminosities.

I 5 Results and discussion

The pattern of the main physical parameters found in the present analysis and their implications for our knowledge of the accretion properties of low luminosity AGNs are discussed in the present section.

The optical to X-ray spectral index, $\alpha_{\rm ox}$. For several objects in our sample we found quite low values of the nuclear optical luminosity. Correspondingly, the estimated spectral index $\alpha_{\rm ox}$ is large. In Fig. I 18, *left panel*, we report the distribution of spectral indices recovered from the decomposition (solid line). In particular we obtained a median value $\langle\alpha_{\rm ox}\rangle \simeq -1.1$, to be compared to the median value $\alpha_{\rm ox} = -1.51$ found for a sample of SDSS AGNs by Strateva et al. (2005, dotted line in Fig. I 18, *left panel*). The mean spectral index does not change much if we use for the host–dominated sources the $\alpha_{\rm ox}$ obtained by assuming the upper limits to the optical emission, decreasing to $\langle\alpha_{\rm ox}\rangle \simeq -1.2$. In this case, the distribution is shown as a dashed area in Fig. I 18, *left panel*. This finding supports the conclusion that our selection picked out sources rather different from optically selected samples.

Table I 6. Nuclear luminosities.

ID	Redshift	$\log L_{\rm 2\text{-}8\,keV}$ [ergs s^{-1}]	$\log L_{\rm [2500\,Å]}$ [ergs s^{-1}]	$\log L_{\rm bol}$ [ergs s^{-1}]	$\alpha_{\rm ox}$	$k_{\rm X}$
...	...				...	...
(1)	(2)	(3)	(4)	(5)	(6)	(7)
			CDF-N			
1	0.679	43.29	28.78	44.79	−1.36	31.62
2	0.747	42.49	27.33	43.49	−1.08	9.77
3	0.762	42.89	27.34	43.72	−0.91	6.76
–	–	–	28.36	44.36	−1.35	29.51
4	0.680	42.46	27.12	43.37	−1.00	8.13
5	0.555	42.41	26.96	43.23	−0.91	6.46
–	–	–	28.12	43.89	−1.42	44.67
6	0.857	42.77	27.73	43.84	−1.13	11.75
7	0.961	43.98	28.44	44.81	−0.91	6.76
8	0.955	42.50	27.36	43.51	−1.09	10.23
9	0.678	43.02	27.88	44.02	−1.09	10.23
10	0.514	43.43	28.57	44.63	−1.21	15.85
11	0.935	42.20	27.65	43.65	−1.34	28.18
12	0.978	43.06	27.97	44.10	−1.11	10.96
13	0.474	42.65	27.16	43.50	−0.93	7.08
14	0.839	42.66	28.26	44.25	−1.41	38.90
15	0.838	42.33	27.60	43.63	−1.27	19.95
			CDF-S			
16	0.839	43.04	27.79	44.10	−1.10	11.48
17	0.668	43.15	27.38	44.14	−0.91	9.77
18	0.734	44.22	29.81	45.78	−1.36	36.31
–	–	–	29.81	45.78	−1.36	36.31
19	0.734	42.86	27.43	44.00	−1.07	14.13
20	0.733	43.01	28.08	44.15	−1.18	13.80
21	0.534	42.58	27.64	43.75	−1.20	14.79
22	0.670	42.41	27.22	43.39	−1.07	9.55
23	0.569	42.92	28.10	44.11	−1.20	15.49
24	0.604	43.07	27.52	43.90	−0.91	6.76
–	–	–	28.46	44.47	−1.32	25.12
25	0.545	42.27	27.03	43.23	−1.04	9.12
26	0.664	42.10	27.21	43.28	−1.20	15.14
–	–	–	27.21	43.27	−1.20	15.14
27	0.734	42.15	27.19	43.27	−1.17	13.18
28	0.735	43.00	27.74	43.95	−1.03	8.71
29	0.679	42.59	27.45	44.00	−1.09	25.70
–	–	–	27.25	43.95	−1.00	22.91
30	0.481	42.95	27.87	43.99	−1.11	10.96
31	0.549	43.50	28.34	44.50	−1.08	9.77
–	–	–	28.59	44.66	−1.19	14.45
32	0.735	43.31	28.02	44.24	−1.02	8.51
–	–	–	28.83	44.83	−1.37	33.11
33	0.668	41.81	27.67	43.47	−1.44	46.77
34	0.910	43.34	27.90	44.21	−0.96	7.41

Note. — In case of nucleus–dominated or host–dominated sources (according to the criteria established in Sect. I 3), the second line shows the parameters obtained starting from the upper limits to the optical magnitudes determined as discussed in the same section.

Col. (1): Source identification number.

Col. (2): Redshift for the optical counterpart, as in Table I 2.

Col. (3): *Unabsorbed* X-ray luminosity at 2 keV band.

Col. (4): UV monochromatic luminosity at 2500 Å.

Col. (5): Bolometric luminosity.

Col. (6): X-ray–to–optical index, defined as
$\alpha_{\rm ox} = \log(L_{\nu\,[2500\,\text{Å}]}/L_{\nu\,[1\,\text{keV}]})/\log(\nu\,[2500\,\text{Å}]/\nu\,[1\,\text{keV}])$.

Col. (7): Hard X-ray bolometric correction, $k_{\rm X} = L_{\rm bol}/L_{\rm X}$.

We may expect that the X-ray selection at very low flux limits singles out objects exhibiting $\alpha_{\rm ox}$ lying in the distribution at the opposite side with respect to the values found for optically selected QSOs. Strateva et al. (2005) found evidence of an increase of the hard X-ray–to–optical luminosity ratio with decreasing optical luminosity (see their Fig 11; see also Fig I 19, where their data are overplotted to our results). It is worth noting that the average value of the spectral index of our sample falls on the extrapolation of the correlation between X-ray and UV emission found by Vignali et al. (2003) for optically selected QSOs and confirmed by Strateva et al. (2005) for optically selected X-detected sources in the *SDSS*. Thus the trend of increasing the X-ray–to–UV luminosity ratio with decreasing UV luminosity and the correlation between optical and X-ray lminosities (already suggested by studies based on *Einstein* data; see, *e.g.*, Tananbaum et al. 1986; Anderson & Margon 1987) is confirmed from the present study down to very low luminosity $L_{2500\,\text{Å}} \sim 10^{27}$ ergs s^{-1} Hz^{-1}. As noted by Strateva et al. (2005), this empirical relation will provide strong constraints on modelling both the accretion disk, where is produced the UV emission, and the surrounding hot corona, origin of the X-ray flux. To date, such a model, able to explain the observed range of $\alpha_{\rm ox}$ as well as its dependence from the UV luminosity, is missing.

The bolometric–to–X-ray luminosity ratio, $\mathbf{k_X}$. The bolometric–to–X-ray luminosity ratio, *i.e.*, the X-ray bolometric correction $k_{\rm X}$, turns out to be generally small. Its distribution is peaked around $k_{\rm X} \simeq 10$, with a tail extending to $k_{\rm X} \simeq 50$ and a median value $k_{\rm X} \simeq 12$ (see Fig. I 18, *right panel*; dashed area marks the distribution after the correction applied for host–dominated sources). In particular, objects with low $k_{\rm X}$ could be the analogous of X-ray AGNs found in optically normal galaxies (*e.g.*, the so-called XBONG; see Comastri et al. 2002, Severgnini et al. 2003, Brusa et al. 2003). We can compare the distribution of $k_{\rm X}$ in our low luminosity X-ray selected AGNs with bolometric corrections reported in literature for different samples of AGNs, first of all the sample of optically bright quasars studied by Elvis et al. (1994). The quasar bolometric corrections by Elvis et al. (1994) is based on *observed* SEDs. As noted in the previous sections (see also Marconi et al. 2004), the contributions to the *intrinsic* nuclear emission come from the accretion disk (UV bump) and the hot corona (X-ray continuum). At wavelength longer than the optical band, the radiation is nuclear emission reradiated by the circumnuclear torus (Antonucci 1993). If we remove the IR contribution from their observed bolometric luminosities, the median bolometric correction is $k_{\rm X} \simeq 25$. Note that in this sample of QSOs the emission in the

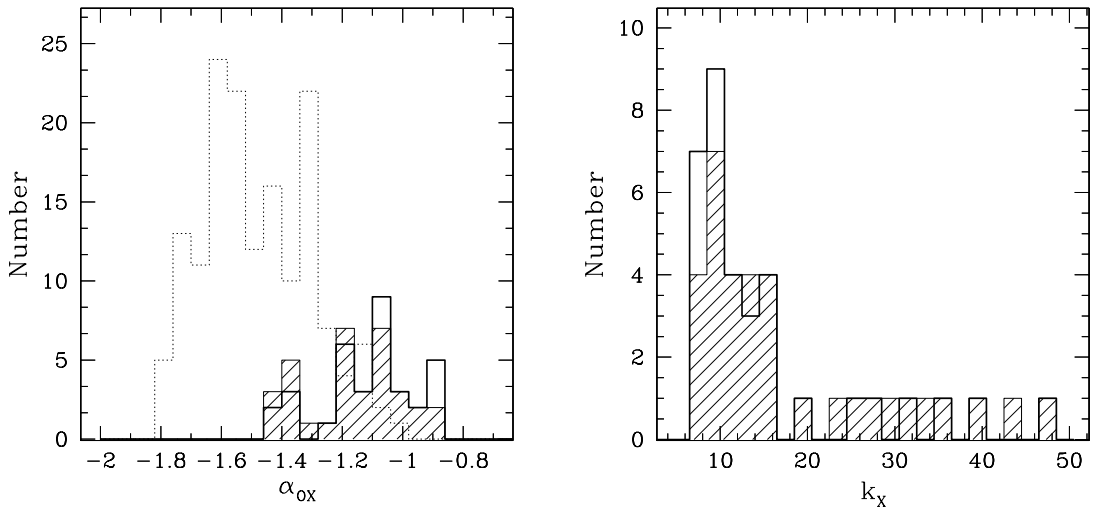

Figure I 18 Distribution of spectral indices α_{ox} (*left panel*) and X-ray bolometric corrections k_X (*right panel*) for sources of the analysed sample; dashed areas show the same distributions obtained taking into account the different treatment adopted for nucleus–dominated or bulge–dominated sources (see Sect. I 3). The dotted line in the spectral index distribution refers to the values found by Strateva et al. (2005) for the X-ray–detected sources in their "main" SDSS sample (155 objects with $0.1 \lesssim z \lesssim 4.5$).

$0.1 - 1$ μm range of wavelengths yields on average about 30% of the bolometric luminosity, while in our sample the percentage is lower, about 8%. The same analysis applied to the sample of type 1 AGNs listed by Kuraszkiewicz et al. (2003) yields a median $k_X \simeq 18$ with a maximum value $k_X \simeq 60$ for AGNs with $10^{43} \leq L_{2\text{-}10\,keV} \leq 10^{46}$ ergs s^{-1}. X-ray bolometric corrections in the range $k_X \simeq 12 - 18$ have been derived for low–luminosity type 1 AGNs by Fabian (2004). Our results suggest that the average bolometric correction for the X-ray emission k_X might be a decreasing function of the X-ray luminosity, as indicated also by Shankar et al. (2004) and Marconi et al. (2004).

Eddington ratios. The Eddington ratios (*i.e.*, the fraction of the Eddington limit at which the AGN is accreting, $\lambda = L_{bol}$ [ergs s^{-1}]$/1.3 \times 10^{38} M_{BH}$ [$M_\odot$]) derived for the analysed sources are plotted in Fig. I 20 as a function of redshift (*left panel*) and of the hard X-ray luminosity (*right panel*). From this figure we can see that in the present sample the Eddington ratios do not exhibit any statistically significant correlation with either redshift or X-ray luminosity. In general, we find AGNs of very low luminosity (all but one in our sample exhibit $10^{43} \leq L_{bol} \leq 10^{45}$ ergs s^{-1}) in galaxies endowed with large bulge

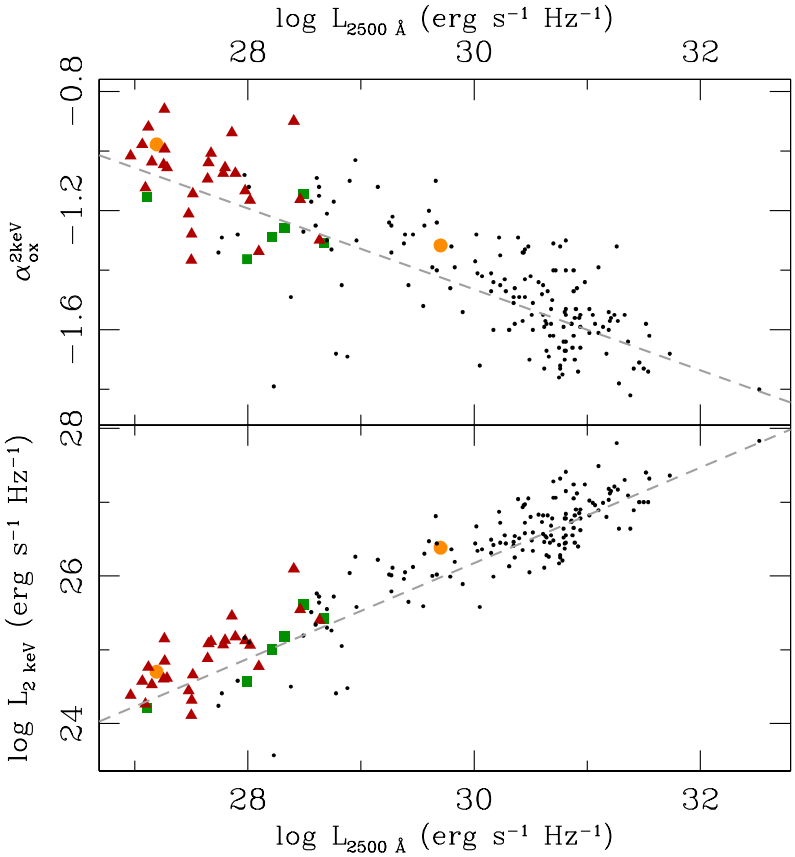

Figure I 19 Dependence on the 2500 Å monochromatic luminosity of $\alpha_{\rm ox}$ (*upper panel*) and $L_{\rm 2\,keV}$ (*lower panel*). Large symbols indicate objects in the present sample, and their meaning is as in Fig. I 15; see also the beginning of Sect I 4. Dots mark data from Strateva et al. (2005) for the X-ray–detected sources in their "main" *SDSS* sample (155 objects with $0.1 \lesssim z \lesssim 4.5$); dashed lines are the best–fit linear relations for their combined sample: $\alpha_{\rm ox} = -0.136 \cdot \log L_{\rm 2500\,\AA} + 2.616$ (*upper panel*) and $\log L_{\rm 2\,keV} = 0.648 \cdot \log L_{\rm 2500\,\AA} + 6.734$ (*lower panel*).

component, so accreting with rather low Eddington ratios.

We plot in Fig. I 21 the Eddington ratios as function of bolometric luminosities (*left panel*) and black hole masses (*right panel*) for our sample and, as a reference sample, for the PG QSO sample studied by Vestergaard & Peterson (2006). The authors derived black hole masses and bolometric luminosities for a large fraction of PG QSOs at redshift $z \leq 0.4$, by exploiting the most recent calibration of the black hole mass as function of the Hβ broad-band luminosity and FWHM. The behaviour of the PG QSO sample is quite similar to that found for QSOs at higher redshift. For instance, Kollmeier et al. (2006)

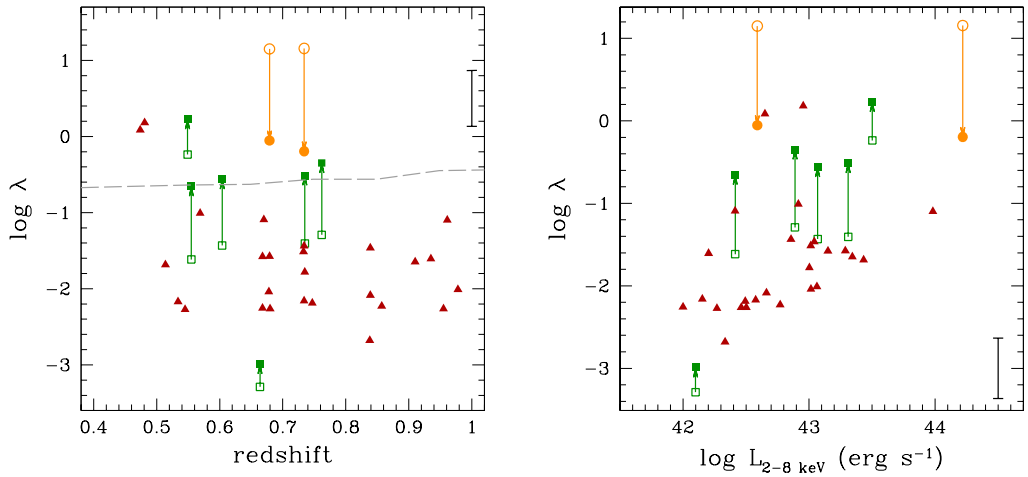

Figure I 20 Eddington ratios versus redshift (*left panel*) and unabsorbed hard X-ray luminosity (*right panel*) for the analysed sample. Symbols for our sample, as in Fig. I 15, are described in Sect I 4. Only mean error bars are reported to avoid clutter. As a comparison, we overplot to our distribution of Eddington ratios versus redshift (*left panel*) the mean (within $\Delta z = 0.1$ bins) values found by McLure & Dunlop (2004) for their full *SDSS* quasar sample (long-dashed line).

found Eddington ratios in the range $0.1 \leq \lambda \leq 1$ for a sample of powerful AGNs covering the redshift range $z \sim 0.3 - 4$, and Warner et al. (2004) estimated that 27% of their QSO sample ($0 \leq z \leq 5$) exhibits $\lambda \geq 1$. The two samples compared in Fig. I 21, *left panel*, are probing different, but complementary, ranges of bolometric luminosity and redshift. It is clear that the low–luminosity sample contains a large fraction of AGNs endowed with quite small Eddington ratios.

The small number of objects with large $L_{\rm bol}$ and small λ is related to the empirical limit to the black hole mass, which cannot exceed several thousandths the mass of the stars in the host galaxy (see, *e.g.*, Magorrian et al. 1998; Gebhardt et al. 2000; see Ferrarese et al. 2006 for a recent discussion). In fact, large bolometric luminosities ($L_{\rm bol} \geq 10^{47}$ ergs s^{-1}) would be obviously easy to observe; but, coupled with small Eddington ratios ($\lambda \leq 10^{-1}$), they would imply black hole masses $M_{\rm BH} \geq 10^{10}\ M_{\odot}$, as clear in Fig. I 21, *left panel*. These masses would be larger than several percent of the mass in stars of the largest galaxies ($M_{\rm star} \leq 10^{12}\ M_{\odot}$). On the other hand, our selection is designed to set up a fair sample of low–luminosity AGNs. Indeed, as a result, we find in our sample a few AGNs with $L_{\rm bol} \leq 10^{45}$ ergs s^{-1} and $\lambda \sim 1$. Our sample points to the very existence of galaxies endowed

with large halos and, therefore, large central black hole masses, hosting low–luminosity AGNs radiating at largely sub-Eddington regime. Woo & Urry (2002) noted that in their compilation there was no object with $L_{\rm bol} \leq 10^{44}$ ergs s^{-1} and $\lambda \gtrsim 1$. Finally, the tail of the nuclear X-ray emission ($10^{41} \leq L_{\rm 2\text{-}10\,keV} \leq 10^{42}$ ergs s^{-1}) at very low Eddington ratios, $\lambda \lesssim 10^{-3}$, in a redshift interval very similar to ours, $0.3 < z < 0.9$, has been detected by Brand et al. (2005) with the stacking technique applied to a sample of red galaxies (*i.e.*, galaxies endowed with significant bulge and, as a consequence, large central black hole).

On the basis of our data and of the results of other authors (Woo & Urry 2002; McLure & Dunlop 2004; Warner et al. 2004; Kollmeier et al. 2006; Vestergaard & Peter-

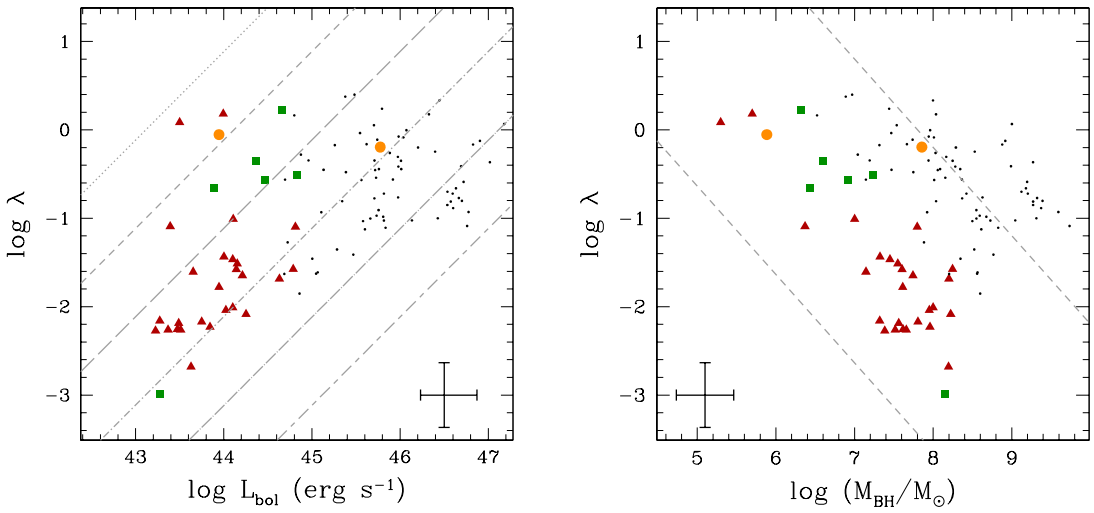

Figure I 21 Eddington ratios distributions for the analysed sample (larger symbols, see Fig. I 15 and Sect. I 4 for the meaning) and for the PG QSO sample at redshift $z \leq 0.4$ studied by Vestergaard & Peterson (2006), marked with dots. The error bars reported represent the mean uncertainties in the derived quantities. *Left panel:* Eddington ratios as a function of bolometric luminosities; from top to bottom, the lines define the trend for black hole masses of 10^5 $M_\odot$ (dotted), 10^6 $M_\odot$ (dashed), 10^7 $M_\odot$ (long-dashed), 10^8 $M_\odot$ (dot-dashed), 10^9 $M_\odot$ (dot-long-dashed), and 10^{10} $M_\odot$ (short-dashed-long-dashed), respectively. *Right panel:* Eddington ratios as a function of black hole masses; the dashed lines define the region in the plane in which the sources are confined on the bases of the hard X-ray luminosity range sampled (lower line: $L_{\rm 2\text{-}8\,keV} = 10^{42}$ ergs s^{-1}; upper line: $L_{\rm 2\text{-}8\,keV} = 1.7 \times 10^{44}$ ergs s^{-1}, the highest value in our sample) and assuming two bracketing values for the X-ray bolometric correction ($k_{\rm X,min} = 3$ and $k_{\rm X,max} = 50$, respectively).

son 2006), we can conclude that low–luminosity objects ($L_{\rm bol} \lesssim 10^{44}$ ergs s^{-1}) exhibit a large range of values of Eddington ratio ($10^{-3} \lesssim \lambda \lesssim 1$), while at high luminosity $L_{\rm bol} \gtrsim 10^{46}$ ergs s^{-1} the range is limited to $10^{-1} \lesssim \lambda \lesssim$ a few. The result can also be represented as a decline of the average value of the Eddington ratio with decreasing bolometric luminosity. This behavior coupled with the shift of the AGN luminosity function towards lower luminosity since $z \simeq 2.5$, may mimic a decrease of the Eddington ratio with decreasing redshift (see, *e.g.*, McLure & Dunlop 2004; Vestergaard 2004; Volonteri et al. 2006). It is worth noting that Salucci et al. (1999), Marconi et al. (2004) and Shankar et al. (2004) have shown that a dependence of λ on luminosity and/or on redshift is required in order to match the local black hole mass function to the mass function estimated from the evolution of the luminosity function of the AGNs.

We stress here that X-ray surveys at faint limits are very efficient in selecting these low–luminosity AGNs, because of the maximum contrast with the host galaxy. Therefore, we do not expect that the CDF-N and CDF-S surveys are missing objects at least up to $z \simeq 1$ (unless they are extremely absorbed, with $N_{\rm H} > 10^{23}$ cm^{-2}; see Fig. 14 in Tozzi et al. 2006). Selecting only "isolated" objects without companions within $2''$ decreases our sample from 53 to 34 objects [see columns (11), (12), (13) and (14) of Table I 1]. The redshift, X-ray flux and apparent magnitude distributions of the optical counterpart of objects in pairs are very similar to those of the final sample (see Fig. I 4). Since the host luminosity distribution of pairs in active and normal samples does not show statistically significant differences, and does not differ dramatically from that of isolated galaxies (Virani et al. 2000; Bergvall et al. 2003), we do not expect that the excluded objects would alter our conclusion. It is worth recalling here that the black hole masses reported in Fig. I 15 and Fig. I 21, *right panel*, have been estimated, following McLure & Dunlop (2002), through equation (I.1), which yields values a factor about $1.5-2$ lower than those evaluated through the $M_{\rm bulge}$–$M_{\rm BH}$ relations proposed by Kormendy & Gebhardt (2001) and Marconi & Hunt (2003).

Summary and conclusions. We found a very small number of AGNs with mass $M_{\rm BH} \lesssim 10^6$ $M_\odot$ *emitting at Eddington ratio* $\lambda \sim 1$. A possible explanation is that the bulk of the mass is accreting on smaller supermassive black holes at high redshift, when the stellar bulge is also built up. Later, both large and small supermassive black holes are on average accreting at low rates. In this case the $\lambda \sim 1$ accretion phase occurs at $z \geq 1$, outside the limit of our primary selection. Besides, the lack of small supermassive black holes can mirror a significant decrease in number density of black holes with $M_{\rm BH} \leq 10^6$ $M_\odot$.

Shankar et al. (2005) inferred a fall-off of the ratio between black hole and halo mass at $M_{\rm BH} \leq 5 \times 10^6\ M_\odot$, by comparing their respective mass functions. It is worth noting that this behavior is predicted in models of galaxy and AGN formation, in which the black hole grows in parallel with the old stellar bulge component and the stellar and AGN feedback affects the efficiency of the gas to cool and form stars (Granato et al. 2001, 2004).

Our analysis enlightens that most of the low–luminosity X-ray selected AGNs in the explored redshift and luminosity intervals are powered by massive black holes $M_{\rm BH} \geq 3 \times 10^6\ M_\odot$ and, as a consequence, that we are mostly witnessing a renewal at low level activity, in galaxies with only small amount of cold gas in the central regions. Probably, most of the black hole mass that we typically find in objects of our sample has been accreted during a higher luminosity phase. Sporadic activity at low accretion rates has been also observed in EROs at $z < 2$ (Brusa et al. 2005). It is very likely that short and sporadic activity is the rule for the supermassive black holes after the bright QSOs phase (see, *e.g.*, Hopkins et al. 2006a, and discussion in Sect. 2). Though the inferred low Eddington ratios can be even sustained for significant time intervals by a number of galactic processes, minor mergers and/or instabilities in the host galaxy induced by satellites are often invoked (see, *e.g.*, Cavaliere & Vittorini 2002). Vittorini et al. (2005) propose an evolutionary model in which, after the formation of massive protogalaxies through early major mergers, the galaxies are subject to minor subsequent interactions with companions. The following episodes of both *fly-by* interaction and cannibalization of small satellites (*e.g.*, Menci et al. 2003) produce small accretion phases, characterized by sub-Eddington AGN emission; time-scale considerations allow to find that the capture rate is higher at redshift $z \sim 1$. On the other hand, Waskett et al. (2005) claim that the environment of a sample of low–luminosity hard X-ray selected AGNs is the same of normal inactive galaxies in the same range of redshift and with similar optical properties. Moreover, recent attempts to find statistical evidence of recent merging in AGN host galaxies at $z \sim 0.4 - 1.3$ are negative (Grogin et al. 2005).

At the end of this part, it is interesting to recall the growing credit given to the hypothesis of a tight link between star formation episodes and AGN activity, probably fueled just via minor mergers and interactions. The redshift range where the bulk of the contributors to the XRB peaks corresponds to the redshift range where the decline in the cosmic star formation rate began ($z \sim 0.7 - 1$). Moreover, according to Barger et al. (2005), observations indicate that both star formation history and accretion history show remarkably similar features, presenting downsizing. All these considerations reinforce the

interest in exploring the re-ignition phase of AGN, as well as the connection between nuclear activity and star formation. A similar investigation, necessarily limited to two test cases (illustrative of the kind of in-depth studies now at hand to have more insight on the accretion properties here derived statistically) will be presented in the next part.

Table I 7. Derived properties.

ID	Redshift	$N_{\rm H}$	$\log L_{\rm 2\text{-}8\,keV}$	$\log L_{\rm bol}$	Bulge M_R	$\log M_{\rm BH}$	$\log \lambda$
...	...	$[10^{22}\ {\rm cm}^{-2}]$	[ergs s^{-1}]	[ergs s^{-1}]	[mag]	$[M_\odot]$	...
(1)	(2)	(3)	(4)	(5)	(6)	(7)	(8)
				CDF-N			
1	0.679	0.50	43.29	$44.79^{+0.90}_{-0.85}$	-21.88 ± 0.29	8.25 ± 0.36	-1.57 ± 0.36
2	0.747	2.02	42.49	$43.49^{+0.67}_{-0.59}$	-20.50 ± 0.33	7.56 ± 0.37	-2.19 ± 0.37
3	0.762	8.22	42.89	$43.72^{+0.31}_{-0.22}$	-19.18 ± 0.32	6.90 ± 0.37	-1.29 ± 0.37
–	–	–	–	44.36	–	6.60	-0.35
4	0.680	3.37	42.46	$43.37^{+0.31}_{-0.25}$	-20.41 ± 0.29	7.52 ± 0.36	-2.26 ± 0.36
5	0.555	0.00	42.77	$43.23^{+0.24}_{-0.17}$	-18.84 ± 0.24	6.73 ± 0.35	-1.62 ± 0.35
–	–	–	–	43.89	–	6.43	-0.65
6	0.857	1.31	43.98	$43.84^{+0.84}_{-0.76}$	-21.30 ± 0.35	7.96 ± 0.37	-2.23 ± 0.37
7	0.961	4.23	42.50	$44.81^{+0.30}_{-0.17}$	-20.97 ± 0.40	7.80 ± 0.39	-1.10 ± 0.39
8	0.955	0.36	43.01	$43.51^{+0.70}_{-0.57}$	-20.70 ± 0.40	7.66 ± 0.39	-2.26 ± 0.39
9	0.678	0.17	43.43	$44.02^{+0.74}_{-0.67}$	-21.28 ± 0.28	7.95 ± 0.36	-2.04 ± 0.36
10	0.514	1.28	43.06	$44.63^{+0.62}_{-0.56}$	-21.78 ± 0.20	8.20 ± 0.34	$-1.68^{+0.34}_{-0.35}$
11	0.935	1.15	42.65	$43.65^{+0.31}_{-0.17}$	-19.67 ± 0.41	7.14 ± 0.39	-1.61 ± 0.39
12	0.978	16.63	42.66	$44.10^{+0.53}_{-0.36}$	-21.38 ± 0.40	8.00 ± 0.39	-2.01 ± 0.39
13	0.474	3.68	42.46	$43.50^{+0.32}_{-0.29}$	-15.98 ± 0.25	5.30 ± 0.35	$+0.09 \pm 0.35$
14	0.839	0.22	42.20	$44.25^{+0.90}_{-0.84}$	-21.83 ± 0.35	8.22 ± 0.37	-2.08 ± 0.37
15	0.838	0.57	42.33	$43.63^{+0.35}_{-0.30}$	-21.77 ± 0.35	8.19 ± 0.37	-2.68 ± 0.38
				CDF-S			
16	0.839	0.64	43.04	$44.10^{+0.37}_{-0.39}$	-20.28 ± 0.35	7.45 ± 0.37	-1.46 ± 0.37
17	0.668	5.56	43.15	$44.14^{+0.42}_{-0.43}$	-20.59 ± 0.29	7.60 ± 0.36	-1.58 ± 0.36
18	0.734	0.19	44.22	$45.78^{+0.24}_{-0.13}$	-18.39 ± 0.33	6.50 ± 0.37	$+1.16 \pm 0.37$
–	–	–	–	45.78	–	7.86	-0.19
19	0.734	1.75	42.86	$44.00^{+0.45}_{-0.52}$	-20.03 ± 0.32	7.32 ± 0.37	-1.44 ± 0.37
20	0.733	7.99	43.01	$44.15^{+0.30}_{-0.31}$	-20.48 ± 0.32	7.55 ± 0.37	-1.51 ± 0.37
21	0.534	0.13	42.58	$43.75^{+0.34}_{-0.31}$	-20.99 ± 0.24	7.81 ± 0.35	-2.17 ± 0.35
22	0.670	1.75	42.41	$43.39^{+0.23}_{-0.30}$	-18.12 ± 0.34	6.37 ± 0.37	-1.09 ± 0.37
23	0.569	0.04	42.92	$44.11^{+0.25}_{-0.19}$	-19.38 ± 0.25	7.00 ± 0.35	-1.01 ± 0.35
24	0.604	23.16	43.07	$43.90^{+0.28}_{-0.25}$	-19.81 ± 0.25	7.22 ± 0.35	-1.43 ± 0.35
–	–	–	–	44.47	–	6.92	-0.56
25	0.545	3.59	42.27	$43.23^{+0.23}_{-0.46}$	-20.15 ± 0.23	7.39 ± 0.35	-2.27 ± 0.35
26	0.664	1.39	42.10	$43.28^{+0.29}_{-0.44}$	-22.29 ± 0.30	8.45 ± 0.36	-3.29 ± 0.36
–	–	–	–	43.27	–	8.15	-2.99
27	0.734	4.40	42.15	$43.27^{+0.30}_{-0.61}$	-20.02 ± 0.33	7.32 ± 0.37	-2.16 ± 0.37
28	0.735	12.55	43.00	$43.95^{+0.24}_{-0.28}$	-20.61 ± 0.32	7.61 ± 0.37	-1.78 ± 0.37
29	0.679	2.63	42.59	$44.00^{+0.25}_{-0.29}$	-14.85 ± 0.40	4.74 ± 0.38	$+1.15^{+0.38}_{-0.39}$
–	–	–	–	43.95	–	5.88	-0.05
30	0.481	73.51	42.95	$43.99^{+0.24}_{-0.27}$	-16.78 ± 0.21	5.70 ± 0.35	$+0.18^{+0.35}_{-0.36}$
31	0.549	150.00	43.50	$44.50^{+0.23}_{-0.22}$	-18.62 ± 0.25	6.62 ± 0.35	-0.24 ± 0.35
–	–	–	–	44.66	–	6.31	$+0.23$
32	0.735	88.76	43.31	$44.24^{+0.38}_{-0.37}$	-20.45 ± 0.33	7.53 ± 0.37	-1.41 ± 0.37
–	–	–	–	44.83	–	7.23	-0.51
33	0.668	0.00	41.81	$43.47^{+0.29}_{-0.44}$	-20.61 ± 0.30	7.62 ± 0.36	$-2.26^{+0.42}_{-0.36}$
34	0.910	37.62	43.34	$44.21^{+0.61}_{-0.22}$	-20.87 ± 0.14	7.74 ± 0.34	$-1.65^{+0.36}_{-0.35}$

Note. — In case of nucleus–dominated or host–dominated sources (according to the criteria established in Sect. I 3), the second line shows the parameters obtained starting from the upper limits to the optical magnitudes determined as discussed in the same section.

Col. (1): Source identification number.

Col. (2): Redshift for the optical counterpart, as in Table I 2.

Col. (3): X-ray absorption, from Tozzi et al. (2006) for the CDF-S, and as recovered from the hardness ratios reported in Alexander et al. (2003) assuming $\Gamma = 1.8$ for the CDF-N.

Col. (4): *Unabsorbed* X-ray luminosity in the $2 - 8$ keV band.

Col. (5): Bolometric luminosity, recovered as described in Sect. I 4.2.

Col. (6): Absolute magnitude of the bulge component in the R band rest-frame corrected for passive evolution (see Sect. I 4.1).

Col. (7): Mass of the central black hole, computed from equation (I.1).

Col. (8): Eddington ratio, defined as $\lambda = L_{\rm bol}\ [{\rm ergs\ s^{-1}}]\ /(1.3 \times 10^{38} M_{\rm BH}\ [M_\odot])$.

Part II

ZOOMING ON THE INTERNAL STRUCTURE: THE X-RAY VIEW

Statistical studies are at the same time test-beds and sources of new input for current evolutionary models. From such studies it appears that local active sources are subject to phenomena of reignition, involving star formation and accretion activity, even if their relative importance could vary in the different evolutionary phases. On the other hand, they are not sufficient to understand the physical processes taking place during the re-activation and their interplay, as they are limited in data quality for individual sources. For example X-ray properties for large samples are based on estimates of hardness ratios, while only spectra of individual objects with sufficient X-ray counts can allow a detailed analysis to establish the presence of an active nucleus and quantify properties such as luminosity, accretion, geometry of the system, and so on; and also to check the limits of the statistical approach. In the last few years, thanks to the X-ray satellites *Beppo*SAX and especially XMM-*Newton* and *Chandra*, this possibility became feasible not only for powerful unabsorbed AGNs but also for more complex systems.

In Part I we detailed our analysis of a *sample* of X-ray selected AGNs. The explored redshift range ($0.4 - 1$, where the XRB redshift distribution peaks) together with the low flux limit allowed us to select a sample of the low–luminosity AGNs which are major contributors to the XRB, and to to explore their accretion properties.

In particular, the most important result of Part I is that a renewal of low–level activity is a common phenomenon in the class of sources constituting a major component

of the resolved XRB. One of the most likely mechanisms of reignition is the interaction of gas–rich galaxies: during merger events, the interstellar gas available could be channeled toward the circum–nuclear regions. In this way, it would start the fueling of the pre–existing black hole, a powerful burst of stellar formation, or both (see Combes 2001 for a review). At the same time, the presence of this gas component embedding the central regions can make more difficult to detect and study the central nuclear activity. Moreover, dust and gas blocking the nuclear continuum will re-emit the absorbed radiation at lower energies: highly absorbed AGNs are expected to be strong IR emitters. As a consequence, local merging systems with powerful IR emission have been subjects of several studies aimed at searching obscured AGNs.

The investigations presented in this part follow these lines. By considering sources with luminosity analogous to those constituting the sample presented in Part I, we aim at performing an in-depth study of individual objects to better understand the mechanisms powering the AGN during re-ignition phase and the connection with star formation activity.

As dust and gas produce a strong extinction of the UV-optical and soft X-ray flux emitted in the center of these systems, the hard X-ray provides the best energy range to perform these investigations: strong emission in this band should be a characteristic of AGNs, as starburst-dominated galaxies emit very few photons in this band (see Sect II 1.1). Furthermore, the hard X-ray band ($E > 6$ keV) comprises (for low redshift sources) the energy range where Fe Kα lines are emitted; a strong line, by itself, can suggest the presence of a deeply absorbed AGN. X-ray high resolution spectroscopy, combined with high energy observations, is therefore a fundamental tool to perform this search; specific examples are, *e.g.*, NGC 6240 (see Vignati et al. 1999; Komossa et al. 2003) and NGC 4945 (Guainazzi et al. 2000).

In the following we describe our work on two particular sources, the merging system Arp 299 and AX J0447-0627.

Arp 299

In the last years high IR luminosity sources have been target of investigations to identify the origin of their powerful IR emission (*i.e.*, intense episodes of star-formation and/or nuclear accretion on compact supermassive objects) and to search for obscured AGNs. Quantifying their frequency is a key point in the evaluation of the energy density of the Universe: as pointed out by Fabian & Iwasawa (1999), if absorbed AGNs are the major contributors to the XRB above 2 keV, then about 85% of the accretion power in

the Universe is absorbed. These investigations are beginning to give some results in terms of the frequency and energetics of the AGN-phenomenon only for the higher luminosity sources (the so-called Ultra Luminous IR Galaxies, defined as galaxies with $L_{\rm IR} > 10^{12}\ L_{\odot}$; Franceschini et al. 2003); these local ultraluminous IR galaxies are always found associated to mergers (see, *e.g.*, the review by Jogee 2005 and references therein). Not much is at present known about the AGN-starburst connection in IR galaxies of lower luminosity.

Sect. II 2 describes the detailed study of the X-ray emission of one of these objects, Arp 299, in which there is evidence for the concomitant presence of starburst activity and AGN. Hence, in this framework this object appears to be an optimal test case for a detailed study on the effects driven by interaction and inflowing of gas during merging phenomena.

AX J0447-0627

X-ray high resolution spectroscopy is a powerful tool to increase our comprehension of the physical processes occurring near the AGN engine, a tool different but as fundamental as the previous one. Indeed the fluorescent line of Fe Kα, the most prominent features in the X-ray spectrum, is regarded as the most direct probe available of the inner accretion disk and central black hole, down to a few gravitational radii. Informations on the origin and on the gravitational and Doppler redshifts of this feature (derived from a detailed study of its profile) can give strong and direct constraints on the geometry and kinematics of the cold matter in the accretion disk. In fact, using this spectral approach we can probe the physics and properties of the accretion mechanism within a few gravitational radii from the event horizon (*e.g.*, Miller et al. 2006; for a recent review, see Reynolds & Nowak 2003).

In Sect. II 3 we present the X-ray observations of AX J0447-0627, an optical type 1 AGN showing in its X-ray spectrum a complex structure in the $4-8$ keV rest frame energy range with a very high observed equivalent width, ~ 2 keV. The most probable explanation for the origin of this feature, the accretion disk, allowed us to put constraints to the physics of the disk itself.

In this context, it is worth noting that these observations of AX J0447-0627 were requested because of the observed *ASCA* hardness ratios of the object, indicative of a hard, presumably obscured, X-ray source (cf. Della Ceca et al. 1999). The case of AX J0447-0627 turned out to be a clear example of how X-ray spectra with complex pattern of peculiar features may be misinterpreted as evidence of obscured objects, in particular when using the statistical tools such as the hardness ratios. In turn, this incorrect interpretation might significantly affect quantitative comparisons between samples selected in the optical and

X-ray bands, which are at the base of evolutionary models. Quantifying the occurrence of objects like AX J0447-0627 is thus of crucial importance.

The detailed study of Arp 299 and AX J0447-0627 will be preceded by a brief summary of the typical X-ray emission features observed and the physical processes believed to cause them (Sect. II 1).

II 1 Introduction. High energy emission

The primary X-ray emission of active nuclei above $0.5-1$ keV is well represented by a power law with photon index $\Gamma \simeq 1.7-2$ (Nandra et al. 1997). In the framework of the Unified Model (see Sect. 1), a similar spectrum naturally arises from thermal Comptonization of disk photons by the surrounding corona (Zdziarski et al. 1994). This primary emission is then modified by its interaction with different structures of matter neutral and/or ionized: the molecular torus, or other flow of matter possibly surrounding the central regions such as the warm absorber. The effects of the intervening medium strongly depend on the angle of view between the central engine and the observer.

The elements present in the matter (*i.e.*, oxygen and iron), if not highly ionized, can absorb the lower energy X-rays and add fluorescent emission lines (Matt et al. 1991, 1996). From the combination of high fluorescent yield and large cosmic abundance it follows that the most prominent of these features is the Fe Kα. Due to the interaction with cold material, the incident power law is partially suppressed, and it is visible only at energies higher than the photoelectric cutoff $E_{\rm C}$, whose value depends on the column density of the absorbing medium, $N_{\rm H}$. Below $E_{\rm C}$, the visible continuum is due to back-scattering of the incident radiation, a process more effective for photons at higher energies. In Fig. II 1 we show a "first order" summary view of the observed X-ray spectra as a function of $N_{\rm H}$.

The continuum modification previously described is strongly enhanced in obscured AGNs, where the line of sight intercepts the absorbing torus. Moreover, when the absorbing column density is higher than several times 10^{23} cm^{-2} the line(s) produced in (or very close to) the accretion disk is (are) suppressed. For column densities $N_{\rm H} > 10^{24}$ cm^{-2}, the optical depth equals unity (hence the name of this class of sources, "Compton-thick"). In these sources, the primary X-ray emission with energy $E \lesssim 10$ keV (in the rest frame) is totally blocked by Thompson-thick matter.

When the line of view is such that the direct emission is totally suppressed, the only contribution to the observed X-ray flux is the reflected continuum; the resultant spectrum,

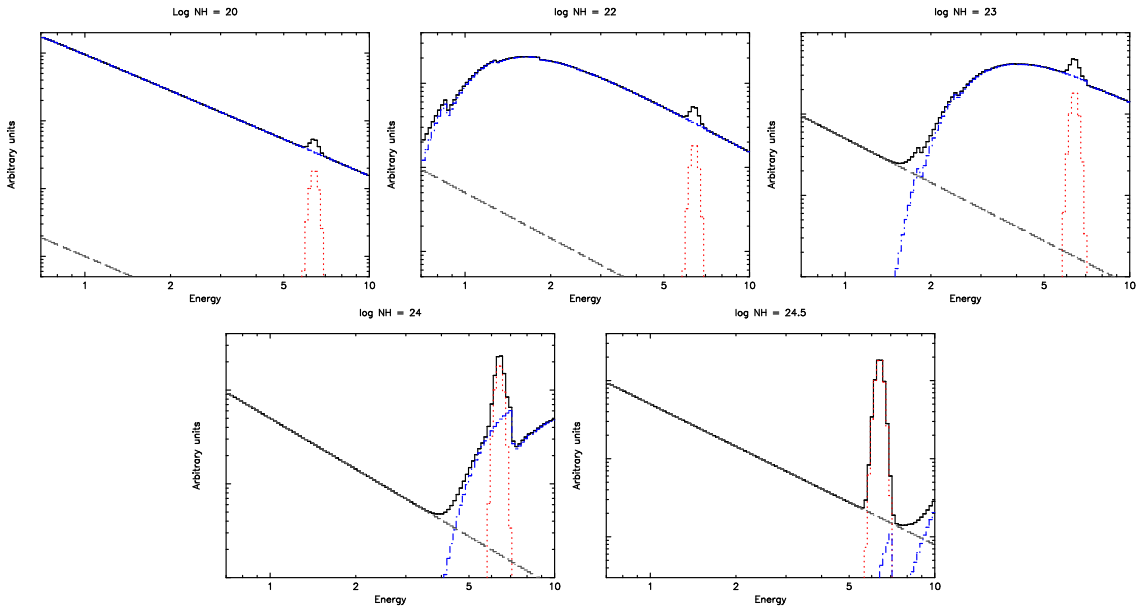

Figure II 1 X-ray spectra in the energy range $0.7 - 10$ keV expected for different column densities $N_{\rm H}$ along the line of sight. Below $E_{\rm C}$ only the scattered emission is visible, while the direct continuum emerges above this energy. The spectra are in arbitrary units. (Adapted from Della Ceca et al. 1999).

with the expected fluorescent Kα emission lines superimposed, is reported in Fig. II 2, *left panel*. Fig. II 2, *right panel* shows how this spectrum is modified if the reflector is not neutral: when its ionization state[1] increases, due to the lack of elements able to absorb the nuclear radiation, there is a decrease in the efficiency of the absorption from lower to higher energies and the modification in the continuum shape results less significant. The centroid of the Fe line shifts from 6.4 keV (cold Fe line) to ~ 6.9 keV due to the presence of more ionized Fe (*i.e.*, Fe XXV and Fe XXVI; Ross & Fabian 1993; Ross et al. 1999). Both the emission line and the absorption edge disappear when the reflector is totally ionized.

Depending on its origin, the energy position, the width and the equivalent width of the observed Fe line could be very different (see Fig. II 3). Hence, these properties can be used to derive informations on the physical state of the emitting regions; if produced by the accretion disk, their study provides primary information about the dynamics and physical processes that are taking place in the innermost part of the AGN (see Fabian, Iwasawa, Reynolds & Young 2000 and Reynolds & Nowak 2003 for a review; Fig. II 4, *right panels*).

[1]The ionization state is described via the ionization parameter $\xi \equiv L_{\rm ill}/(n\,R^2)$, where $L_{\rm ill}$ is the luminosity of the continuum, n is the numerical density (part cm^{-3}) of the illuminated slab and R is the distance between the slab and the illuminating source.

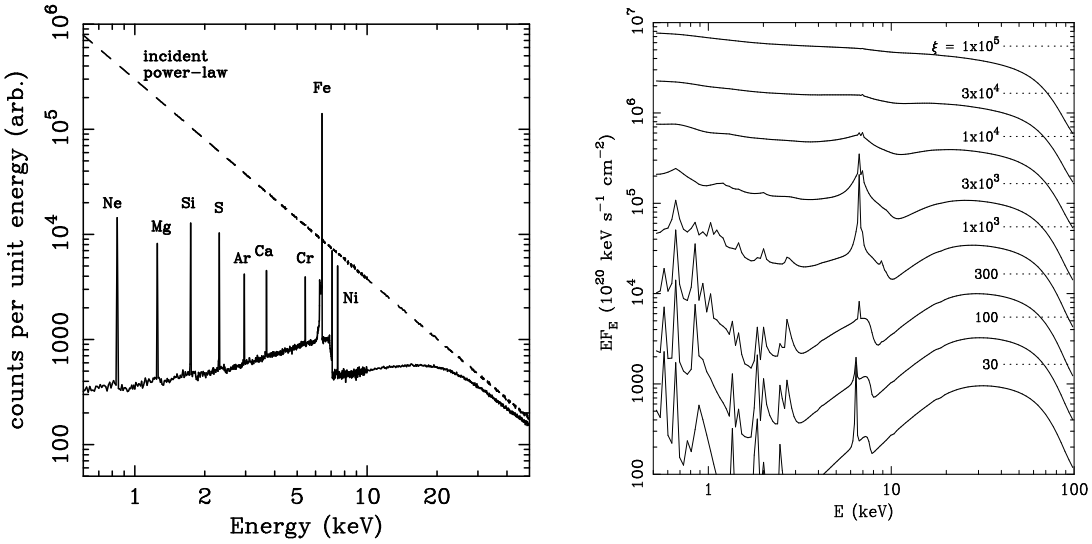

Figure II 2 *Left panel:* X-ray reflection of an incident power law spectrum (shown as dashed line) from an illuminated cold and semi-infinite slab of gas (from Reynolds 1996). *Right panel:* change of the reflected spectrum as a function of the ionization state of the slab; the level of the illuminating power law for the various values of ξ is indicated by the dotted lines (from Fabian, Iwasawa, Reynolds & Young 2000).

– The Fe line produced in a medium (neutral or ionized) far from the nucleus is narrow ($\sigma_{\rm K\alpha} < 0.1$ keV); its energy position depends on the abundances of Fe more ionized than Fe XVII and thus on the ionization state of the reprocessing medium. When the intrinsic continuum is heavily absorbed the "observed" equivalent width of the line could be as high as a few keV (Matt, Fabian & Ross 1993; Matt et al. 1996), because of the suppression of the underlying continuum by the same medium producing the line.

– The line produced in the disk is expected to be broadened by relativistic effects ($\sigma_{\rm K\alpha} >$ 0.2 keV, see George & Fabian 1991; Matt et al. 1991); a schematic view of how Doppler shifts, relativistic beaming and gravitational shift can modify the line profile is reported in Fig. II 4, *left panel*. The equivalent width of a typical disk line is $\sim$ 200 eV.

Finally, it is worth recalling how recent XMM-*Newton* and *Chandra* observations have discovered complex spectral features (broad and/or narrow) red-ward of the Fe emission line(s) in a number of AGNs (Turner et al. 2002; Guainazzi 2003; Yaqoob et al. 2003; Turner et al. 2004; Porquet et al. 2004; Bianchi et al. 2004; McKernan & Yaqoob 2004;

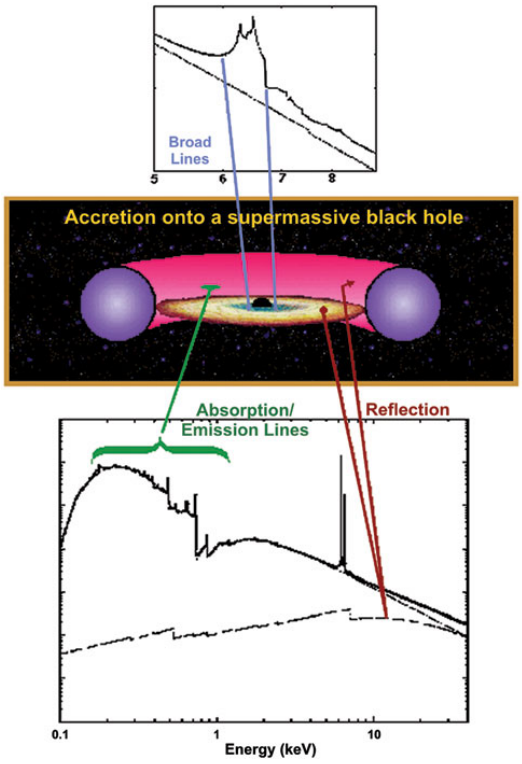

Figure II 3 *Upper panel:* spectrum of the X-rays produced in the accretion disk, near the event horizon. The iron line is broadened by the force of extreme gravity from the black hole. Broad lines are present close to the black hole, where gravity is most intense; and the extent of broadening and the shape of the profile relate to the mass and spin rate of the black hole, as well as to the region of the accretion disk where these feature originate. *Middle panel:* diagram of the innermost regions of an AGN, with an accretion disk bordered by a thick tube of dust. *Lower panel:* spectrum of dust and gas outside the accretion disk, with typical narrower emission lines. (Courtesy of I. George, GSFC) .

Gallo et al. 2004). Among the models invoked to explain these features, there are

- a localized hot spots on the accretion disk surface due to illumination by local flares (*e.g.*, Dovčiak et al. 2004);
- reprocessed emission from narrow annuli on the surface of the accretion disk (Gallo et al. 2004);
- inflow or outflow of material (*e.g.*, the ejected blob model proposed by Turner, Kraemer & Reeves 2004 to explain the properties of the narrow lines observed in MKN 766);

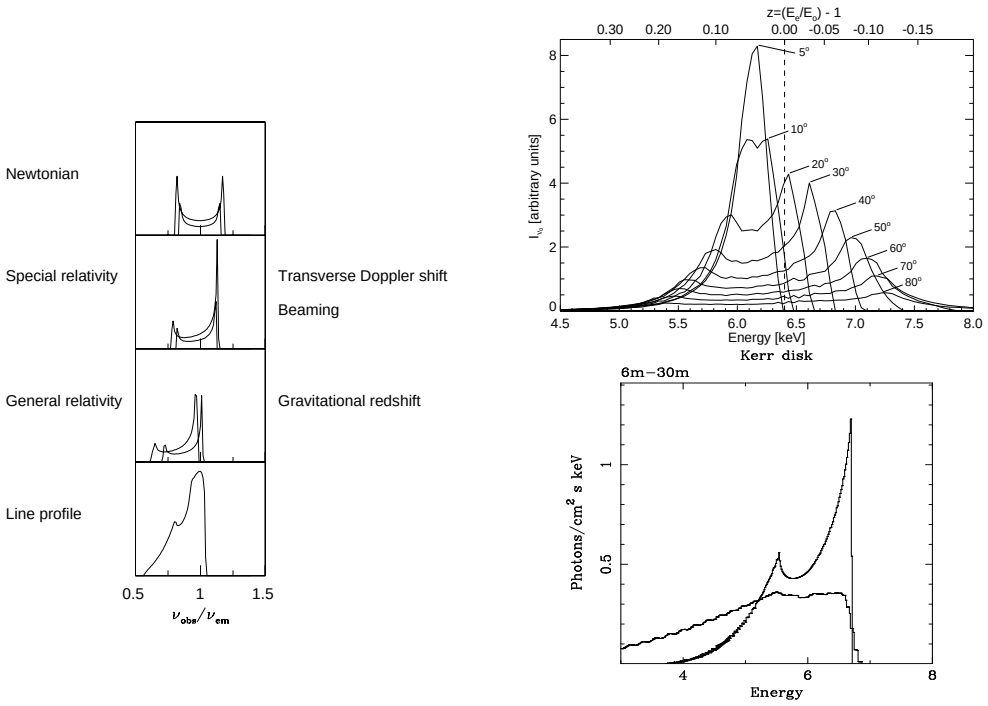

Figure II 4 Skewness and enhancement of a Fe line profile originated in an accretion disk as a function of different relativistic or nonrelativistic effects (*left panel*). Relativistic Fe profiles as a function of disk inclination (from an accretion disk around a rapidly-rotating black hole, *upper-right panel*), and of black hole spin (from Schwarzschild, narrower line, to Kerr blach hole, broader line; *lower-right panel*). Adapted from Fabian, Iwasawa, Reynolds & Young (2000) and Reynolds & Nowak (2003).

– destruction (spallation) by energetic protons on the accretion disk surface of Fe into lower Z elements (mainly Cr and Mn), implying an enhancement of the line emission expected from elements of lower abundance (Skibo 1997).

II 1.1 Concomitant AGN and starburst

In the present work, we are interested in sources where both AGN and starburst are present. Then it could be useful to describe the emission expected by the latter component, and the X-ray spectrum of a composite system. Indeed, when the accreting nuclear activity is coupled with a burst of intense central star formation, the X-ray emission becomes even more complex. One of the signatures of the enhanced star formation rate is an X-ray emission, which is generally more luminous than that of normal galaxies. This

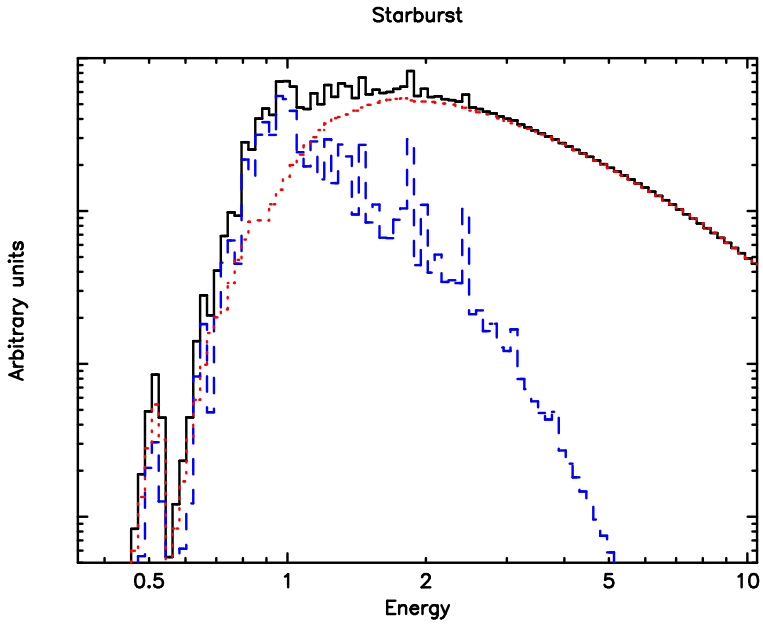

Figure II 5 Example of the expected X-ray spectrum for a starbursting component (from Persic & Rephaeli 2002). In ascending order at 2 keV we show the SNRs and HMXBs spectra, and the total emission; the Fe K emission line at 6.7 keV is not included. The assumed luminosities (in the $0.5-50$ keV band) are $\log L_{\rm SNRs} = 37.0$ ergs s^{-1} and $\log L_{\rm HMXBs} = 37.7$; the spectra are absorbed through a hydrogen column density of $N_{\rm H} = 10^{22}$ cm^{-2}.

X-ray emission is related mainly to supernova remnants (SNRs), galactic winds and X-ray binaries. X-ray observations of know starburst galaxies showed that the $0.5-10$ keV spectra are clearly complex (see Fig. II 5)

- The emission below 1 keV is dominated by a low-temperature ($kT \simeq 0.6-0.8$ keV) thermal component, interpreted as originating from the boundary region between the hot, low-density outgoing galactic wind and the cool, high-density interstellar matter (*e.g.*, Heckman et al. 1999; Strickland et al. 2000).

- At higher energies, the observed spectrum can be modelled either as thermal emission with $kT \simeq 5-10$ keV (related to the SNRs), or as a power-law model with $\Gamma \simeq 1.5-2$ (mainly due to unresolved point sources), or as their combination (*e.g.*, Weaver et al. 2000; Dahlem et al. 2000). A Kα feature at the energy of 6.7 keV of highly ionized Fe is expected from young SNRs (NGC 253 and M82, see Persic et al. 1998; Cappi et al. 1999); its intensity then must be tied to the SNRs intensity, and could be used to quantify the importance of this thermal component. XMM-*Newton* and in

particular *Chandra* observations of starburst galaxies (see NGC 253, Pietsch et al. 2001, Weaver et al. 2002; M82, Stevens et al. 2003; NGC 4038/4039, Zezas et al. 2002) have shown that the $2-10$ keV flux is dominated by point-source emission. Recently, Persic & Rephaeli (2002) developed a detailed quantitative model of X-ray spectra of "pure" starburst galaxies, based on evolutionary populations of galactic stars and on templates of X-ray spectra for the relevant emission processes and components. In particular they suggested that the $2-15$ keV spectrum is mainly due to the emission of High- and Low-Mass X-ray binaries. Both categories of X-ray binaries have spectra that can be described as cutoff power laws (White et al. 1983; Christian & Swank 1997) with Γ ranging form 1.1 to 1.4. Assuming a mix of High- and Low-Mass X-ray binaries of various luminosities in Galactic proportions, the $2-10$ keV emission can be described as a cutoff power law $E^{-\Gamma}e^{-E/kT}$ with photon index $\Gamma \sim 1.1$ and cutoff energy $kT \sim 8$ keV. In this context, it is worth noting that also an X-ray binaries component is expected to produce a Fe Kα at the energy of 6.4 keV, even if with intensity lower than the same feature produced by an AGN.

X-ray observations of composite starburst-AGN present, in addition to the AGN emission (dominant at energies higher than ~ 3 keV), a soft and usually extended thermal component (Levenson, Weaver & Heckman 2001a,b), attributed to the starburst activity. The observed X-ray spectrum depends on the amount of obscuration suffered by the AGN and on the relative strength of the thermal component associated with the starburst activity. Comparing the $N_{\rm H}$ distribution in a sample of Seyfert 2 and composite starburst/Seyfert 2 galaxies, Levenson, Weaver & Heckman (2001b) noted that the latter tend to have higher $N_{\rm H}$ (directly measured or inferred). This leds the above authors to propose that in composite sources also the circumnuclear starburst can strongly obscure the AGN. For illustrative purpose, Fig II 6 shows a model representing a deeply buried AGN with a concomitant starburst component, and the expected X-ray spectrum.

II 2 AGN(s) in a local merging system. A paradigm

In this section we present a specific example of Arp 299, a system composed by two starburst galaxies in which X-ray data from the *Beppo*SAX satellite for the first time unveiled the presence of an AGN of high luminosity. Moreover, more spatially resolved XMM-*Newton* observations strongly suggest that both the nuclei could host an AGN.

Arp 299 is a energetically powerful merging system located at D = 44 Mpc (Heck-

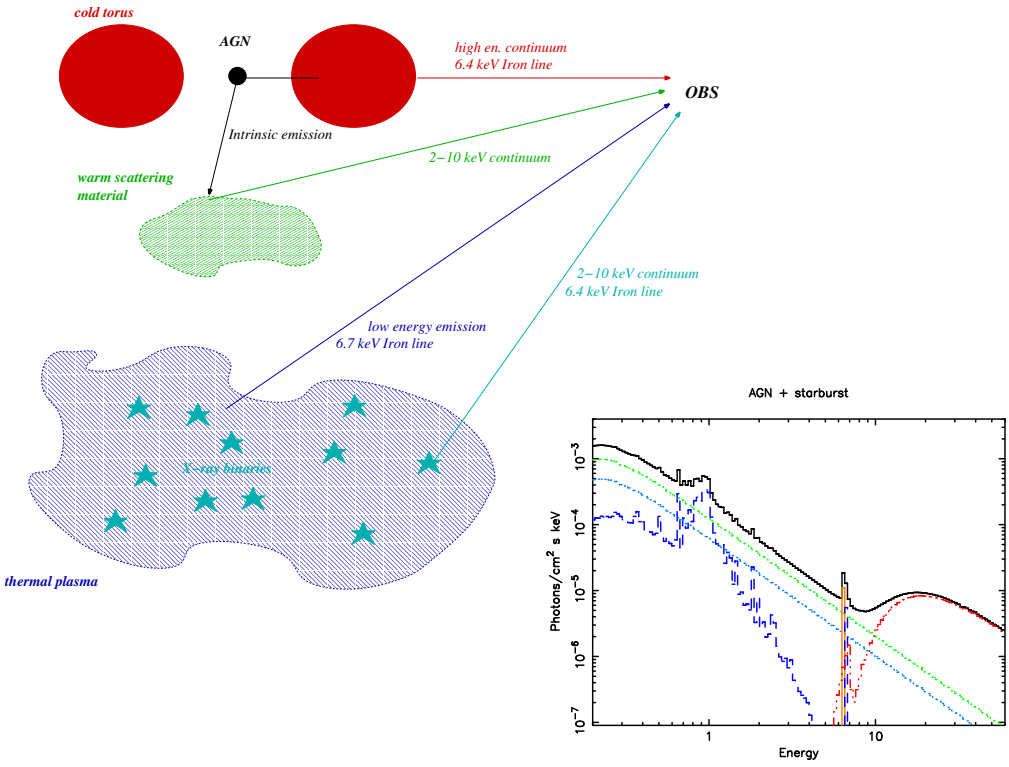

Figure II 6 Sketch of the interplay of AGN and starburst for an highly absorbed nucleus ($N_{\rm H} \gtrsim 10^{24}$ cm^{-2}). The energetic range where the corresponding emission is emitted and the spectral feature expected for each component are marked. The spectra are also shown with the same color code: thermal emission and ionized Fe line from thermal plasma (blue dashed line); $2-10$ keV continuum from X-ray binaries (sky-blue dotted line) and from the warm medium scattering the intrinsic radiation (green dotted line); transmitted high energy continuum (red dot-dot-dashed line); neutral Fe line from the absorbing material and the X-ray binaries (orange continuous line).

man et al. 1999). The far-IR luminosity, $L_{\rm 43\text{-}123\ \mu m} = 2.86 \times 10^{11}\ L_{\odot}$ (derived following the recipes in Helou et al. 1988 and using the *IRAS* Faint Source Catalog Fluxes, Moshir et al. 1990), dominates the bolometric output. Proximity and high luminosity in IR make Arp 299 an ideal candidate to search for phenomena triggered by interaction and able to restart central accretion, as well as to try to quantify its importance in the energetic of this systems. Indeed, in the presence of high-density gas and dust components a nuclear optical-ultraviolet emission will be absorbed and reradiated at lower frequencies: extremely absorbed systems with powerful nuclei are expected to show a very intense IR emission. Moreover, its relative proximity should allow to detect AGN activity even if this component

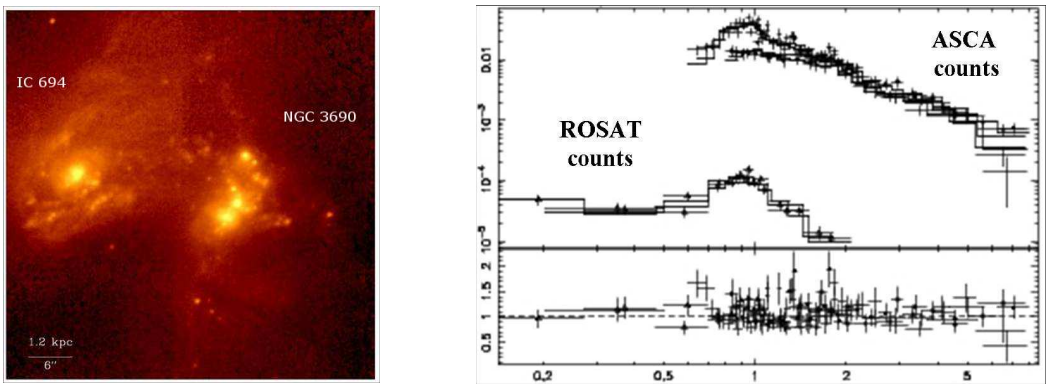

Figure II 7 *Left: HST*-NICMOS near IR observations of IC 694 and NGC 3690 (from Alonso-Herrero et al. 2000). *Right: ROSAT* and *ASCA* X-ray counts of Arp 299 (adapted from Zezas, Georgantopoulos & Ward 1998).

is not dominant.

The system under scrutiny consists of two galaxies in an advanced merging state, NGC 3690 to the west and IC 694 to the east, plus a small compact galaxy to the northwest (Heckman et al. 1999). The centers of the two merging galaxies are separated by $\sim 22''$ (Heckman et al. 1999), corresponding to a projected distance of 4.6 kpc (see Fig. II 7, *left*). For a detailed description of the system and for a summary of previous multiwavelength observations, see Zezas, Georgantopoulos & Ward (1998); Heckman et al. (1999); Hibbard & Yun (1999); Charmandaris, Stacey & Gull (2002). Briefly, in the IR range IC 694 shows a compact site of activity in the central region, while NGC 3690 is resolved into a complex of sources without a distinct central nucleus (Wynn-Williams et al. 1991; Alonso-Herrero et al. 2000). Mid-/far-IR observations ascribe the powerful emission of both the galaxies to starbursting activity (Laurent et al. 2000). Optical spectroscopy presented in Coziol et al. (1998) shows that IC 694 can be classified as a pure starburst galaxy, while NGC 3690, according to its line properties, is borderline between starburst and LINER. Concerning the radio properties, Gehrz, Sramek & Weedman (1983) suggested that the nucleus of IC 694 (and only this one) could host an AGN. Finally, Arp 299 was observed with the *ASCA* and *ROSAT* satellites; in both cases the observed emission was typical of a starbursting system (Zezas, Georgantopoulos & Ward 1998; Heckman et al. 1999). We note however that in the energy range covered by the HRI instrument on board *ROSAT* ($E < 2$ keV, where a starburst emission is important) we do not expect any signature of an obscured AGN. On the other hand, a Fe Kα line (even if intense) could be easily lost in a short *ASCA*

observation (taking into account its low S/N above 5 keV). The X-ray counts from both the observations are shown in Fig. II 7, *right*.

II 2.1 Unveiling the hidden AGN

We observed Arp 299 with *Beppo*SAX on December, 14 - 18, 2001: in what follows a short summary of our main result is reported, while the whole spectral analysis and a detailed discussion on our findings are shown in Della Ceca et al. (2002). The wide energetic coverage provided by the scientific payload of *Beppo*SAX was ideal to search for the features typical of deeply absorbed AGNs [Fe line(s) and intrinsic continuum at $E \gtrsim 10$ keV, see Sect. II 1.1] and to disentangle the starburst activity from the AGN emission, although the spatial resolution of its instruments ($\sim 2'$), was not sufficient to resolve systems such as Arp 299. The spectral analysis reported in Della Ceca et al. (2002) showed that a single-component models[2] do not provide an adequate description of the broad-band ($0.1-40$ keV) spectrum of Arp 299. Fig. II 8, *left*, shows the ratio between *Beppo*SAX data and the best-fit unabsorbed power-law model ($\Gamma \sim 1.9$). Clearly evident are: a bump at ~ 0.8 keV, which is a characteristic signature on the X-ray spectra of all known starburst galaxy (see *e.g.*, Dahlem, Weaver & Heckman 1998); a strong line-like structure at ~ 6.4 keV; a big bump in the $10-40$ keV energy range. Simultaneous occurrence of these last two features is a distinctive spectral signature of an obscured AGN (Matt et al. 2000; see Sect. II 1.1).

We found that an adequate description of the broadband *Beppo*SAX data is provided by model including:

- a soft thermal component[3]
- a "leaky-absorber" model (an absorbed power law[4], representing the "first order" AGN continuum emerging after transmission through an obscuring cold medium, plus an unabsorbed power law with the same photon index Γ, representing the primary AGN

[2] All the models discussed in the following for the whole Arp 299 as well as for IC 694 and NGC 3690 have been filtered through a foreground Galactic absorption of $N_{H,Gal} = 9.92 \times 10^{19}$ cm^{-2} (Dickey & Lockman 1990); all the errors are at 90% confidence level for 1 parameter of interest ($\Delta\chi^2 = 2.71$). The reported line positions refer to the source rest frame; the metallicity of the thermal component(s) used was fixed to the solar value.

[3] Unless otherwise stated, to describe a thermal component we used a MEKAL model in XSPEC, an emission spectrum from hot diffuse gas based on the model calculations by Mewe et al. (1985, 1986) and Kaastra & Mewe (1993), with Fe L calculations by Liedahl et al. (1995); the model includes line emissions from several elements.

[4] Given the high $N_{\rm H}$ expected, it has been modeled in XSPEC using PLCABS, that describes the X-ray transmission of an isotropic source of photons located at the center of a uniform, spherical distribution of matter, correctly taking into account Compton scattering (Yaqoob 1997).

spectrum scattered into the line of sight by a warm, highly ionized gas located outside the absorbing medium)

– a Gaussian emission line at $E \sim 6.4$ keV.

Finally, there are some residuals possibly suggesting the presence of a second emission feature at $E \sim 3.4$ keV, consistent with the Ar XVIII Kα line. This best fit model is shown in Fig. II 8, *right*.

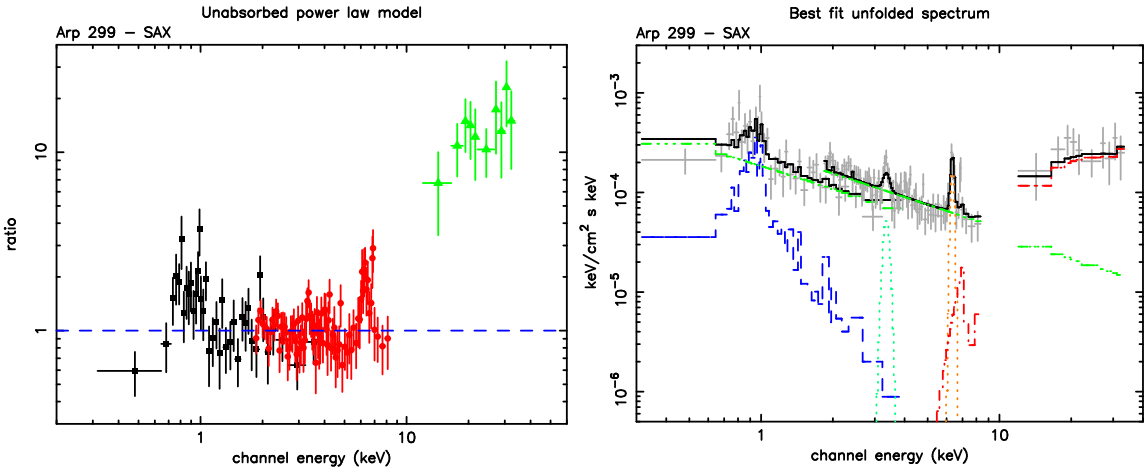

Figure II 8 *Left:* ratio of the unabsorbed power–law model to the *Beppo*SAX data. *Right:* unfolded model (thermal component, leaky-absorber continuum and two Gaussian lines) best fitting the *Beppo*SAX data. From Della Ceca et al. (2002).

Results from *Beppo*SAX observations

The *Beppo*SAX observations clearly unveiled for the first time in this system a strongly absorbed AGN ($N_{\rm H} \simeq 2.5 \times 10^{24}$ cm^{-2}, with an intrinsic luminosity $L_{0.5-100\ \rm keV} \simeq 1.9 \times 10^{43}$ ergs s^{-1}). As discussed in Della Ceca et al. (2002), the Gaussian line at a rest frame energy position of $\simeq 6.42$ keV (observed equivalent width of $\simeq 636$ eV) is consistent with a low ionization Fe Kα line, produced by transmission through the same cold absorbing medium (the putative torus and/or starburst related dust) that affects the primary AGNcontinuum. Indeed, the equivalent width measured with respect to the transmitted component, ~ 7 keV, is consistent with what is expected from transmission (see, *e.g.*, Leahy & Creighton 1993), and in the higher end of the possible equivalent width predicted from the Ghisellini, Haardt & Matt (1994) model using a simple toroidal geometry.

Concerning the starburst component, the best fit soft X-ray thermal model is con-

sistent with that previously obtained by Zezas, Georgantopoulos & Ward (1998), Heckman et al. (1999) using *ROSAT* plus *ASCA* data. It is also similar to that usually found in other well studied starburst galaxies (*e.g.*, Dahlem, Weaver & Heckman 1998). The *Beppo*SAX data cannot rule out that at least part of the observed $2-10$ keV X-ray luminosity is due to this starburst component, more precisely to the emission of X-ray binaries (see Persic & Rephaeli 2002), which may also contribute to the observed Fe Kα emission.

It is worth recalling that with the *Beppo*SAX data resolution the location of the AGN inside the interacting system Arp 299 was still an open question (*i.e.*, it was not solved the association of the AGN with the two nuclei).

II 2.2 Disentangling the X-ray emission of IC 694 and NGC 3690

Arp 299 was the target of both *Chandra* and XMM-*Newton* observations, separated by 2 months, and about 6 months before the *Beppo*SAX observation. Both the satellites have onboard instruments with sufficient resolution to spatially resolve the system (see Figg. II 9 and II 10)

A detailed spectral and spatial analysis of the *Chandra* data has been published in Zezas et al. (2003). In this context it is intersting to note what follow.

- The X-ray spectrum of the source associated with the nucleus of IC 694 is well fitted with an absorbed ($N_{\rm H} \simeq 1.2\times10^{22}$ cm^{-2}) power-law, consistent with either a population of X-ray binaries or an AGN.
- Neither a thermal component nor a strong Fe Kα line are required by the fit for both the nuclei; as noted, the former is probably due to the very small region used in the spectral extraction by Zezas et al. (2003), while the latter is because of the poor photon statistics in the 6 keV region.
- The nucleus of NGC 3690 shows a very hard X-ray spectrum, typical of a heavily obscured AGN.

Archival XMM-*Newton* data: our analysis

The result obtained from our *Beppo*SAX data (*i.e.*, the presence in Arp 299 of a deeply absorbed AGN, that we were not able to localize) induced us to collect the XMM-*Newton* and *Chandra* archival data. The analysis of the archival XMM-*Newton* data, de-

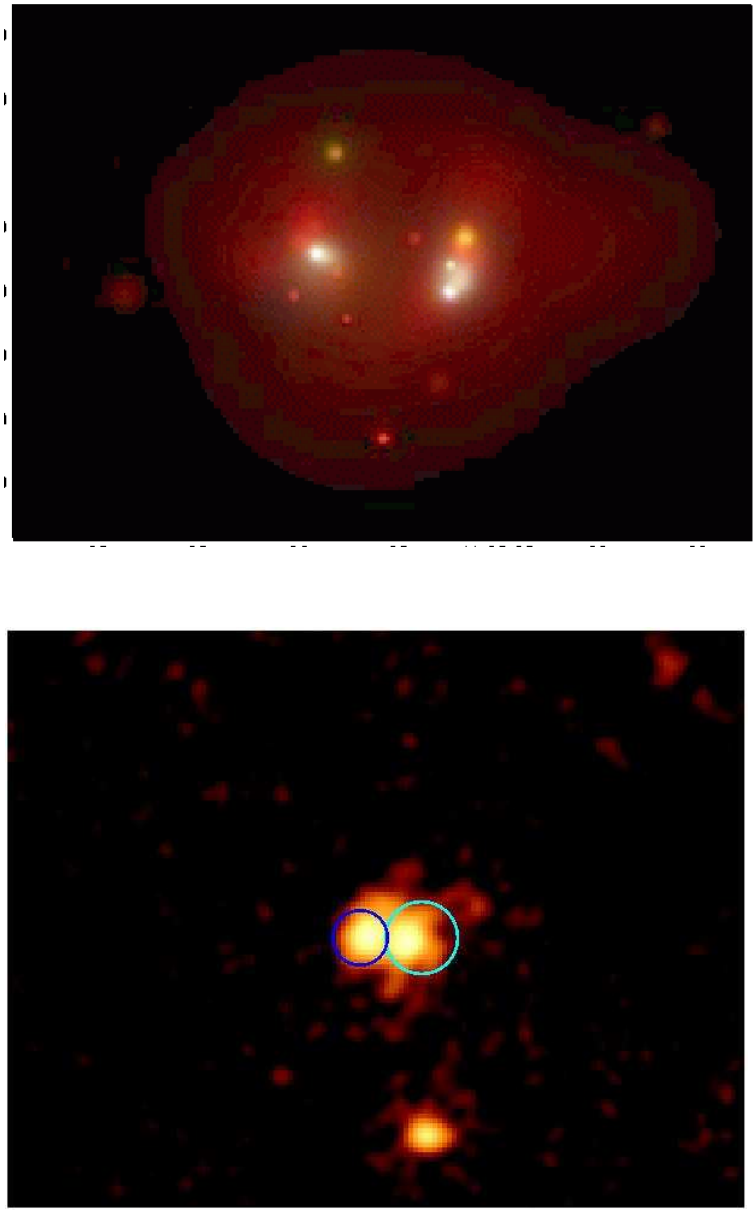

Figure II 9 *Upper panel:* true color X-ray image of Arp 299, from the combined soft (red), medium (green) and hard (blue) band smoothed *Chandra* images (from Zezas et al. 2003). This image clearly shows an important diffuse soft component, as well as a few hard discrete sources, that can be identified with the knots of emission observed at optical and IR wavelength (cf. Fig. II 7, *left*; see also Fig. II 10). *Lower panel:* XMM-*Newton* EPIC-pn $2-10\,\mathrm{keV}$ image of Arp 299; the circles mark the regions considered for the spectral analysis. Both the nuclei are clearly resolved.

tailed in the following, has been presented in Ballo et al. (2004). We exploited the excellent spatial resolution of *Chandra* coupled with the XMM-*Newton* spectral information to assess the origin of the X-ray emission.

Arp 299 was observed by XMM-*Newton* on May 6, 2001 for a total of about 20 ksec, with MOS1, MOS2 and pn observing in full frame mode (*i.e.*, the whole field of view is covered) and with the thin filter applied. In this analysis only EPIC-pn data were used, since the MOS data are of insufficient quality above 6 keV, where the Fe Kα line is expected. The XMM-*Newton* data have been cleaned and processed using the Science Analysis Software (SAS version 5.4), and analysed using standard software packages (FTOOLS version 4.2, XSPEC version 11.2). Event files produced from the standard pipeline processing have been filtered for high-background time intervals and only events corresponding to patterns $0-4$ have been used (see the XMM-*Newton* Users' Handbook; Ehle et al. 2001); the net exposure time after data cleaning is ~ 14 ksec. The latest calibration files released by the EPIC team have been used. The response matrices at the position of the system have been also generated using the SAS tasks `arfgen` and `rmfgen`. No statistically significant source variability has been detected during the XMM-*Newton* observation.

In Fig. II 10 the X-ray contours obtained from the *Chandra* ACIS-I data in three different energy ranges ($0.5-2$ keV, panel a; $2-10$ keV , panel b; $6.3-6.9$ keV, panel c) are superimposed on the *HST* WFPC2 image obtained with the F814W filter ($\lambda_{\rm eff} \simeq 8203$ Å, $\Delta\lambda \simeq 1758.0$ Å). As also shown also by Zezas et al. (2003), the X-ray contours point out the concomitant presence of an extended component and three compact knots of emission, associated with the two galaxies; increasing the energy range from $0.5-2$ keV to $2-10$ keV, the former becomes more concentrated around the knots. It is worth of noting that, when observed in the $6.3-6.9$ keV energy range, the strongest sources are clearly localized in two regions associated with the two merging galaxies; moreover, the north-west knot in NGC 3690 disappears.

The XMM-*Newton* image in the $2-10$ keV energy range shows two sources of comparable brightness corresponding to the two interacting galaxies (see Fig. II 9, *lower panel*). First of all, we analysed the XMM-*Newton* EPIC-pn spectrum of the whole Arp 299 system combined with the *Beppo*SAX data. We fitted the data in the $0.3-40$ keV energy range with the *Beppo*SAX best-fit model described in Sect. II 2.1. The overall model proposed by Della Ceca et al. (2002) well reproduces the XMM-*Newton*+*Beppo*SAX data, upon addition of an extra absorption component in front of the soft thermal component, with a column density of $N_{\rm H,\ soft} \sim 1.5\times10^{21}$ cm^{-2} (consistent with the absorption found for

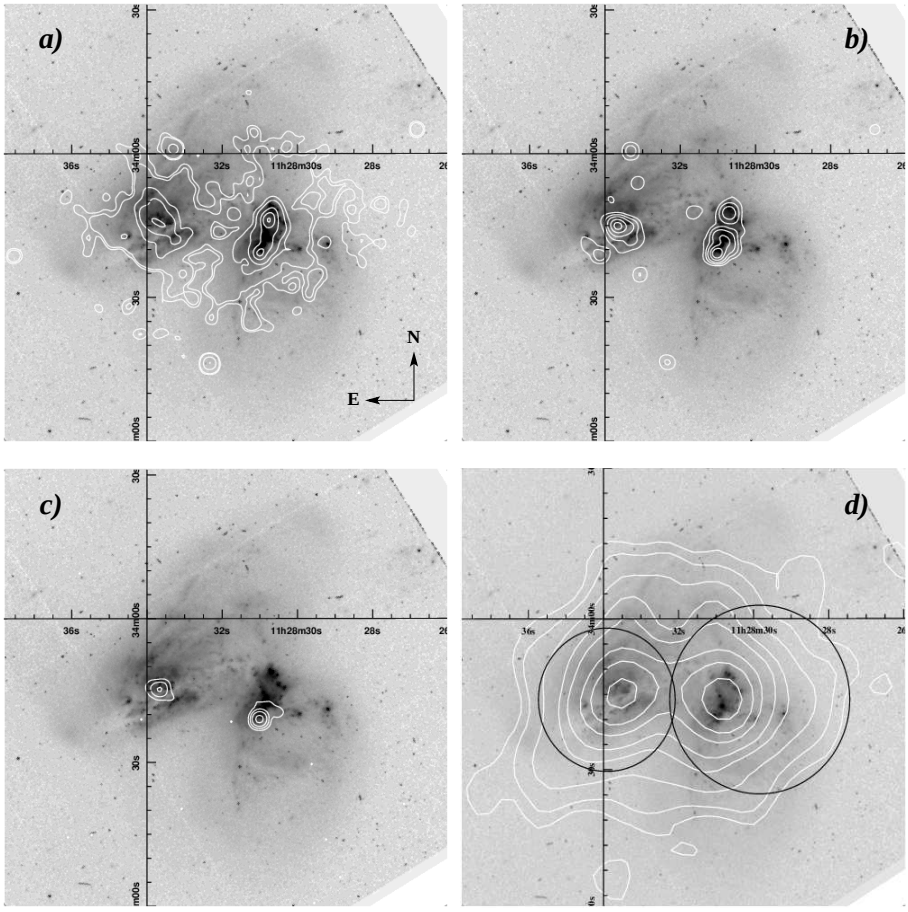

Figure II 10 X-ray contours derived from the *Chandra* ACIS-I data in different energy ranges superimposed on the *HST* WFPC2 image; *panel a*: $0.5 - 2$ keV (contours corresponding to 0.13, 0.32, 0.64, 1.26, 3.15, 4.73 and 6.30 counts/pixel); *panel b*: $2 - 10$ keV (contours corresponding to 0.24, 0.51, 0.96, 1.86 and 2.76 counts/pixel); *panel c*: $6.3 - 6.9$ keV (contours corresponding to 0.04, 0.10, 0.19 and 0.38 counts/pixel). *Panel d*: XMM-*Newton* EPIC-pn contours of Arp 299 in the $0.5 - 10$ keV band, corresponding to 3σ, 5σ, 10σ, 20σ, 30σ, 50σ, 70σ and 100σ, superimposed on the same image; the circles mark the regions considered for the spectral analysis, as in the previous figure.

several Seyfert 2 galaxies with circum-nuclear starbursts, see Levenson, Weaver & Heckman 2001a,b). The values found for the most relevant parameters (intrinsic absorption, $N_{\rm H,\ hard}$; photon index Γ; energy of the thermal component, kT; and centroid of the higher energy line) are in good agreement with the *Beppo*SAX analysis quoted in Della Ceca et al. (2001). This global modelling of Arp 299 is also a good fit of the XMM-*Newton* EPIC-pn data only, with the only exception that the presence of a Gaussian line at 3.4 keV is not required.

The absorbed fluxes and the intrinsic (*i.e.*, unabsorbed) luminosity are consistent with our previous results, confirming our earlier conclusion about the presence of a deeply buried AGN in the system.

Using only the EPIC-pn data we have studied the X-ray emission produced by the two merging galaxies. The spectra were extracted from two circular regions centered at the X-ray centroid positions of the two sources, see Figg. II 9, *lower panel* and II 10, *panel d* (for IC 694 the radius is smaller because of the proximity of the CCDs gap). The background spectra were extracted from two source-free circular regions close to the individual sources. The net count rate ($0.5-10$ keV energy range) of IC 694 (NGC 3690) is 0.1686 ± 0.0044 counts s^{-1} (0.2291 ± 0.0049 counts s^{-1}) and represents about 97.5% (98.3%) of the total counts in the source extraction region. Source counts have been rebinned to have a number of counts greater than 10 in each energy bin.

- Contrary to the *Chandra* data reported by Zezas et al. (2003), the XMM-*Newton* spectra of both the galaxies clearly show the presence of line like emission features at energies between 6.3 keV and 7 keV (see the ratio of the XMM-*Newton* data to a single unabsorbed power law fit in Fig. II 11, *upper panels*).
- At energies lower than 2 keV the dominant contribution is due to the thermal emission associated with the starburst component; the luminosities of these thermal components in IC 694 and NGC 3690 are similar.
- The two galaxies contribute to the observed $2-10$ keV continuum of the whole system Arp 299 with similar intensities.

The emission in the $2-10$ keV energy range (where the contribution from the soft thermal component is negligible) is well described by an absorbed power law + a Gaussian emission line; the results of our analysis are reported in Table II 1 and are shown in Fig. II 11, *central* and *lower panels*. The main difference between the two objects is the position and the equivalent width of the Fe emission lines. In the case of IC 694 the energy of this feature is consistent with He-like Fe Kα, while in the case of NGC 3690 the energy is consistent with Fe Kα from neutral Fe, with an equivalent width consistent with the value derived from the *Beppo*SAX data (with respect to the observed continuum).

Table II 1. Results of the spectral analysis (EPIC-pn $2-10$ keV): partially absorbed power law + narrow Gaussian line.

	Power Law		Line						
	Γ	Norm [a]	E	Norm [b]	EW	$N_{\rm H,\ soft}$ [c]	Flux [d]	Luminosity [e]	χ^2/d.o.f.
	...	...	(keV)	...	(eV)	(10^{21} cm^{-2})	(10^{-13} ergs cm^{-2} s^{-1})	(10^{41} ergs s^{-1})	...
IC 694	1.95 ± 0.20	$1.52^{+0.43}_{-0.32}$	$6.69^{+0.12}_{-0.09}$	$3.02^{+1.40}_{-1.46}$	818^{+380}_{-396}	2.35	4.33	1.02	40.62/45
NGC 3690 [f]	$1.80^{+0.44}_{-0.32}$	$1.29^{+1.46}_{-0.49}$	$6.36^{+0.27}_{-0.14}$	$1.92^{+1.20}_{-1.31}$	422^{+262}_{-288}	5.56	4.37	1.06	50.45/50

Note. — Errors are quoted at the 90% confidence level for 1 parameter of interest ($\Delta\chi^2 = 2.71$). The net count rate in the $2-10$ keV energy range is 0.0363 ± 0.0031 counts s^{-1} for IC 694 and 0.0401 ± 0.0031 counts s^{-1} for NGC 3690 (about 97.6% and 97.3% of the total counts, respectively).

[a] In units of 10^{-4} photons keV^{-1} cm^{-2} s^{-1} @1 keV.

[b] In units of 10^{-6} photons keV^{-1} cm^{-2} s^{-1} in the line.

[c] Column density of neutral hydrogen in addition to $N_{\rm H,\ Gal} = 9.92 \times 10^{19}$ cm^{-2}.

[d] Observed X-ray fluxes.

[e] Observed X-ray luminosities.

[f] The line profile appears marginally broad ($\sigma = 0.32^{+0.64}_{-0.25}$ keV). This can be due to the blending of several lines: if the $2-10$ keV continuum is produced by a "warm mirror" which scatters the primary radiation of the central source, than we would expect emission lines from highly ionized Fe. A second line like feature seem to be present at higher energies ($E \sim 7$ keV) but the present statistics precludes from firm conclusions.

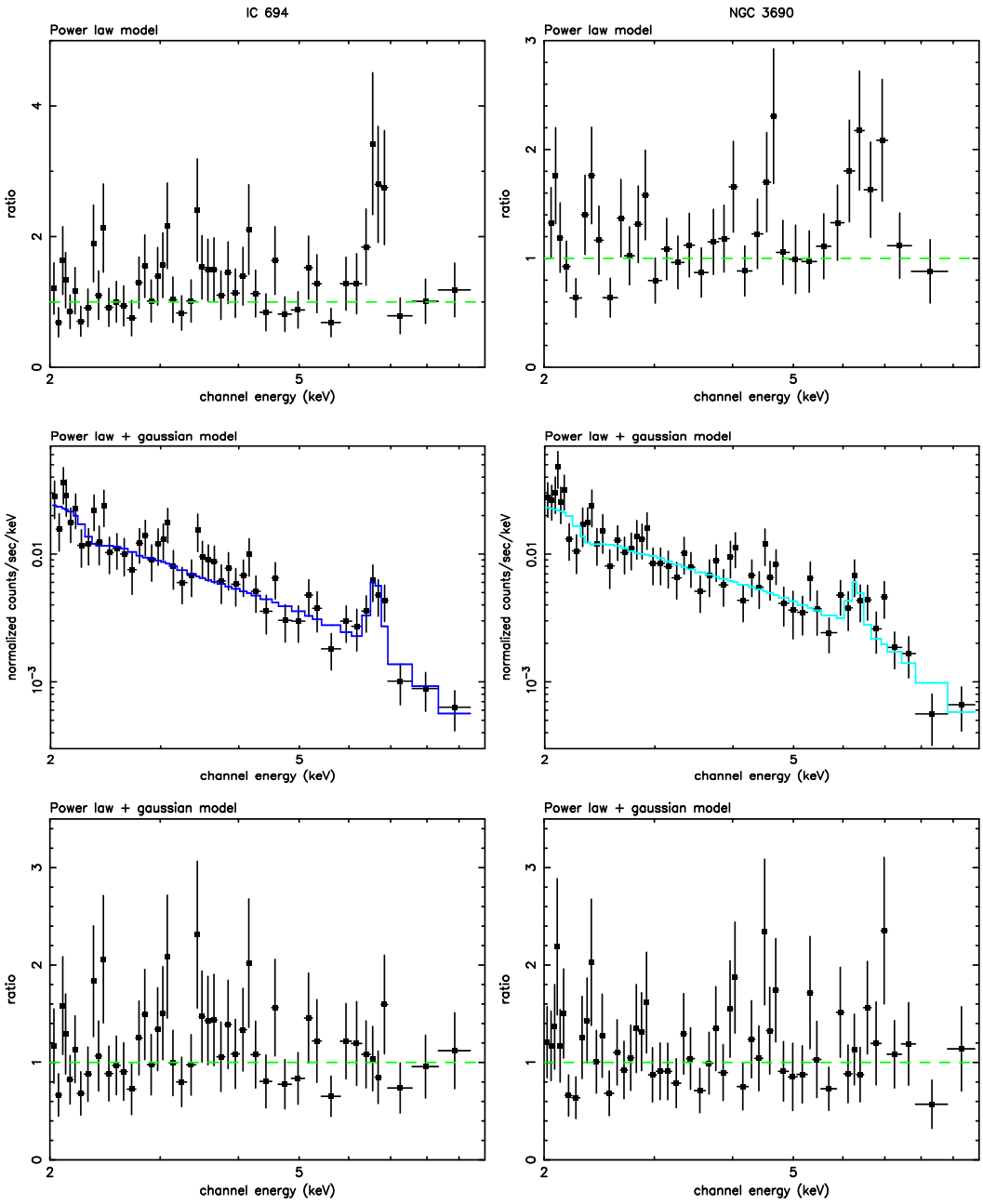

Figure II 11 Results of the XMM-*Newton* EPIC-pn data for IC 694 (*left*) and NGC 3690 (*right*) fitted with different models. *Upper panels*: ratio of a simple power-law model to the data. For demonstration purposes, in this Fig. the data of NGC 3690 were binned to have a number of counts greater than 15 in each energy bin. *Central panels*: data and folded spectra for a fit with a power law component and a Gaussian line. *Lower panels*: ratio of the data to the power law + Gaussian line model.

II 2.3 Discussion

The spectral analysis described above has important implications for the location of the deeply buried AGN in this system.

*Beppo*SAX observations established the presence in Arp 299 of a deeply buried AGN, obscured by neutral material with column density $\sim 2.5 \times 10^{24}$ cm^{-2}, which makes the direct X-ray continuum from the AGN only visible at energies greater than 10 keV. So in the energy range covered by XMM-*Newton* it is completely absorbed; the only observable and clear signature of this AGN is a cold Fe Kα line with high equivalent width, as expected if produced by transmission through the neutral material responsible for the absorption measured by *Beppo*SAX (as schematized in Fig. II 12, *upper panel*) and as evident in *Beppo*SAX data. Such a line is clearly detected in the XMM-*Newton* spectrum of NGC 3690, strongly confirming the presence in this galaxy of the absorbed AGN already revealed with the *Beppo*SAX observation. If this is the case, the continuum observed by XMM-*Newton* in the $2-10$ keV energy range is a small fraction of the intrinsic one. This continuum is probably due to a combination of emission from sources related to the starburst (*e.g.*, X-ray binaries) and/or reprocessed AGN emission (reflection and/or scattering) to our line of sight. The XMM-*Newton* data do not allow us to disentangle these different contributions.

The case of IC 694 is more ambiguous, since the 6.7 keV line from highly ionized Fe could be produced by a high temperature thermal plasma. In fact we were able to reproduce the $2-10$ keV spectrum of IC 694 (continuum + line) using a combination of a cutoff power law model (reproducing the integrated emission of X-ray binaries, see Persic & Rephaeli 2002) and a thermal model with $kT \simeq 5.5$ keV; the two components are linked so as to reproduce the fraction of X-ray emission assigned by *Chandra* to discrete sources (Zezas et al. 2003). During the fit the slope of the cutoff power law model was constrained to vary between 1.3 and 1.5, while we fixed the cutoff energy to $E = 8$ keV (Persic & Rephaeli 2002). The resulting temperature is higher than the values typically found in supernova remnants (SNRs), but consistent with that found, for instance, in the SNR N132D by Behar et al. (2001). Assuming a typical X-ray luminosity of young SNRs of $L_{\rm X} \sim 10^{37}$ ergs s^{-1} and a typical duration of the hot phase of 1000 yr (cfr. Persic & Rephaeli 2002), the measured $2-10$ keV thermal luminosity of IC 694 ($\sim 6.5 \times 10^{40}$ ergs s^{-1}) implies about 6500 SNRs in the nuclear starburst and a supernovae rate of 6.5 yr^{-1}. The latter value is about a factor 10 larger than supernovae rate estimated in the central part of IC 694 ($< 5''$, where the bulk of the $2-10$ keV emission is produced; see Fig. II 10, *panel b*) from radio and near-IR observations (Alonso-Herrero et al. 2000). Leaving the intensity, the slope and the cutoff

energy of the binary cutoff power law model free to vary these numbers do not change in a significant way. Thus, although the data do not definitively rule out the starburst origin of the emission line, this possibility implies rather extreme conditions (number of SNRs and high plasma temperature).

Despite the fact that the luminosity of the Fe Kα emission line might depend on several ambient factors, some information about the expected line intensity can be supplied by a comparison with starburst galaxies showing such a line. We note that, among "pure" starburst galaxies, the He-like Fe line at $E \sim 6.7$ keV with an equivalent width comparable to that of IC 694 is firmly detected only in NGC 253[5]. In order to compare our results with those obtained with *Chandra* for NGC 253 (Weaver et al. 2002) we estimated the central ($\sim 5''$) FIR luminosity of IC 694 using the radio measurement at 1.4 GHz (taken from the FIRST - Faint Images of the Radio Sky at Twenty-centimeters - survey[6]) and the well-known radio/IR correlation for star-forming galaxies (Condon 1992). We have rescaled the Fe line luminosity of NGC 253 reported by Weaver et al. (2002) using the ratio of the FIR luminosities of the two galaxies, and we have found that the starburst emission could account for about 20% of the observed line intensity in IC 694. Note that also NGC 253 may harbor a hidden AGN, as suggested by some authors (see, *e.g.*, Mohan, Anantharamaiah & Goss 2002), in which case the starburst contribution is probably less.

Thus there is a strong possibility that in the nucleus of IC 694 may be present an AGN (as also suggested on the basis of its radio properties, see Gehrz, Sramek & Weedman 1983). In this case, the presence of an He-like Fe Kα emission line suggests that the AGN continuum could be scattered/reflected by a highly ionized gas. A similar emission line (not accompanied by a cold Fe Kα line) has been recently found by XMM-*Newton* in the FRI galaxy NGC 4261 (Sambruna et al. 2003).

We then tried to model the spectrum with a reflected component[7] as described by Ross & Fabian (1993). Since the predicted continuum due to reflection by an ionized slab can be characterized by features at low energies, we considered the full $0.5 - 10$ keV spectrum, adding a MEKAL thermal component at low energies to take into account the starburst contribution. This model describes quite well the entire spectrum and can reproduce the Fe Kα line with physically acceptable values for the main parameters: $kT \sim 0.2$ keV, $\Gamma \sim 2$ and an ionization parameter $\xi = 2.6 \times 10^3$.

[5]The only other starburst galaxy that shows a line from highly ionized Fe is M82, but its equivalent width is significantly lower than that measured here (Cappi et al. 1999; Rephaeli & Gruber 2002).

[6]See `http://sundog.stsci.edu/`

[7]Available in XSPEC as a `table` model file provided by David Ballantyne (Ballantyne et al. 2001), see `http://heasarc.gsfc.nasa.gov/docs/xanadu/xspec/models/iondisc.html`

The absence of a neutral Fe Kα line and the lack of any sign of absorption due to a medium with high column density indicate that the AGN inside IC 694 is not heavily absorbed ($N_{\rm H} \leq 10^{22}$ cm^{-2}). The observed $2-10$ keV radiation is probably the direct emission of the central source, an AGN of low luminosity ($L_{\rm X} \sim 10^{41}$ ergs s^{-1}) surrounded by a cloud of highly ionized gas (as schematized in Fig. II 12, *lower panel*). The most probable reason that prevents us from identifying IC 694 as an AGN from optical spectroscopic observations is the strong circum-nuclear starburst (note that the FIR luminosity is about 3 orders of magnitude greater than the X-ray luminosity of the AGN, see Charmandaris, Stacey & Gull 2002), that could dilute its optical light (see, *e.g.*, Georgantopoulos, Zezas & Ward 2003).

To conclude, although a starburst origin of the X-ray emission observed in IC 694 cannot be ruled out, the most plausible hypothesis to explain the X-ray data presented here seems the existence of an AGN in each merging galaxy, one highly absorbed ($N_{\rm H} \simeq 2.5 \times 10^{24}$ cm^{-2}) and of high luminosity ($L_{0.5-100\ \rm keV} \simeq 1.9 \times 10^{43}$ ergs s^{-1}), the other one less luminous ($L_{2-10\ \rm keV} \simeq 10^{41}$ ergs s^{-1}) and surrounded by highly ionized gas.

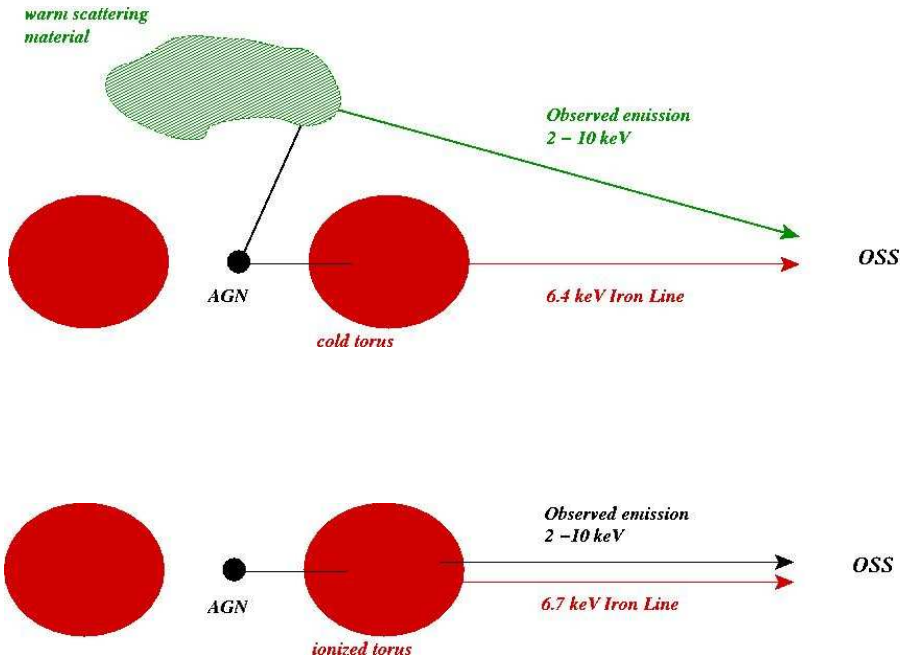

Figure II 12 Schematic cartoons representing the nuclei of NGC 3690 (*upper panel*) and IC 694 (*lower panel*), as required to explain the XMM-*Newton* data if both the galaxies host an AGN.

II 3 Relativistic features in a candidate for deep absorption

The importance of quantifying the frequency of obscured AGNs, and of assessing their energetics, is a topical argument in this thesis. Surveys (such that described in Part I) produce large databases that are ideal goldmines to pick out peculiar objects, suitable for a more in-depth study. An example of this is the case of AX J0447-0627, which attracted our attention due to its hard X-ray colours, suggesting a strong absorption.

AX J0447-0627 is one of the hardest X-ray sources of the *ASCA* Hard Serendipitous Survey (Cagnoni, Della Ceca & Maccacaro 1998; Della Ceca et al. 1999). It was detected with a signal-to-noise ratio (S/N)= 5.40 in the *ASCA* field pointed at NGC 1667 (*ASCA* sequence ID= 71032000) at the nominal *ASCA* position of RA = 04:47:48.6, Dec = −06:27:50.8 (J2000.0). The net *ASCA* GIS2 counts from the source are 54 ± 10 ($2-10$ keV), corresponding to a $f_{2-10\ \mathrm{keV}} \sim 3 \times 10^{-13}$ ergs cm^{-2} s^{-1} (assuming a power-law photon index $\Gamma = 1.7$). Its hardness ratios are indicative of a hard, presumably obscured, X-ray source (see Fig. II 13, where we report its position in the hardness ratio diagrams): HR1= -0.40 ± 0.15 and HR2= 0.32 ± 0.17 (cf. Della Ceca et al. 1999). Here HR1 and HR2 are defined as a comparison of counts between the medium and the soft bands, and the hard and the medium band, respectively: HR1= $(M-S)/(M+S)$ and HR2= $(H-M)/(H+M)$, where $S = [0.7-2$ keV$]$ counts s^{-1}, $M = [2-4$ keV$]$ counts s^{-1} and $H = [4-10$ keV$]$ counts s^{-1}.

II 3.1 XMM-*Newton* observations and optical classification

Starting from the *ASCA* hardness ratios, to clarify the nature of this type 2-candidate, we obtained an XMM-*Newton* observation of AX J0447-0627 performed on 2002, September 8, for a total of about 29 ks. The three EPIC cameras (MOS1, MOS2 and pn) were operating in full frame mode with the thin filter applied. The XMM-*Newton* data have been cleaned and processed using the Science Analysis Software (SAS version 5.4) and analysed using standard software packages (FTOOLS version 4.2, XSPEC version 11.2). Event files have been filtered for high-background time intervals, and only events corresponding to patterns $0-12$ (MOS 1&2) and $0-4$ (pn) have been used (see Ehle et al. 2001); the net exposure times at the source position after data cleaning are ~ 21.4 ks (MOS1, MOS2) and ~ 17.5 ks (pn).

The XMM-*Newton* MOS1, MOS2, and pn images in the $0.5-10$ keV energy range reveal a high S/N (~ 30 and ~ 50 in the MOS and the pn, respectively) point-like source within the *ASCA* 90% positional error circle ($\sim 2'$ radius) of AX J0447-0627. This is the

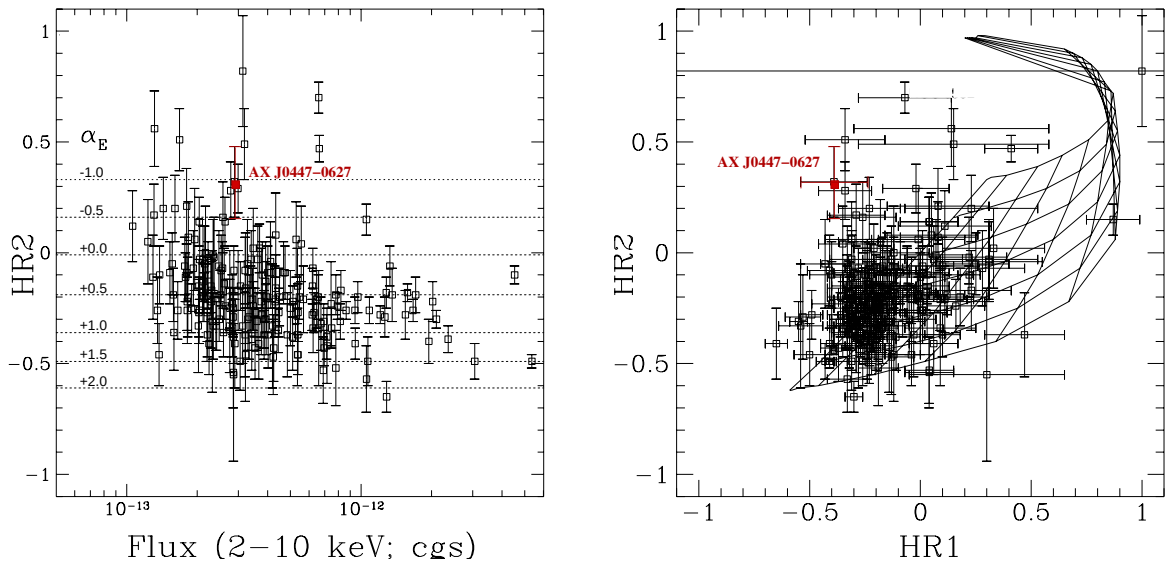

Figure II 13 Diagnostic diagrams for the *ASCA* serendipitous sources; the position of AX J0447-0627 is marked as a red square. *Left panel:* HR2 value versus $2-10$ keV flux compared with what expected from an unabsorbed power law ($F_{\rm X} \propto E^{-\alpha_{\rm E}}$); the "inverted" spectrum presented by AX J0447-0627 seems to be indicative of a very hard or very absorbed source. *Right panel:* position of AX J0447-0627 in the hardness ratio diagram; the solid lines show the loci expected from spectra described by an absorbed power law, with from top to bottom $\alpha_{\rm E} = -1; -0.5; 0.0; +0.5; +1.0; +1.5; +2.0$, and from left to right $\log N_{\rm H} = 21.0; 21.5; 22.0; 22.25; 22.5; 22.75; 23.0; 23.5; 24.0$.

only detected and visible X-ray source in the *ASCA* error circle; the X-ray position derived using the XMM-*Newton* data is RA = 04:47:48.62, decl. = −06:28:12 ($\sim 21''$ away from the nominal *ASCA* position).

The improvement in the knowledge of the X-ray source position allow to identify its optical counterpart. A bright optical source (RA = $04^{\rm h}47^{\rm m}48^{\rm s}.5$, decl. = $-06°28'13''$; APM[8] red magnitude = 17.7) lies about $2''$ from the X-ray position derived using the XMM-*Newton* data. This object was observed spectroscopically at the Telescopio Nazionale Galileo with DOLORES (Device Optimized for the LOw RESolution) on 2002, October 5.

The optical spectrum (shown in Fig. II 14) covers the wavelength range $\sim 3500-$

[8]Magnitude from the Automatic Plate Measuring (APM) catalog, compiled by scanning with the Cambridge APM machine photographic plates taken with the UK Schmidt Telescope, the Palomar Schmidt and the Curtis Schmidt.

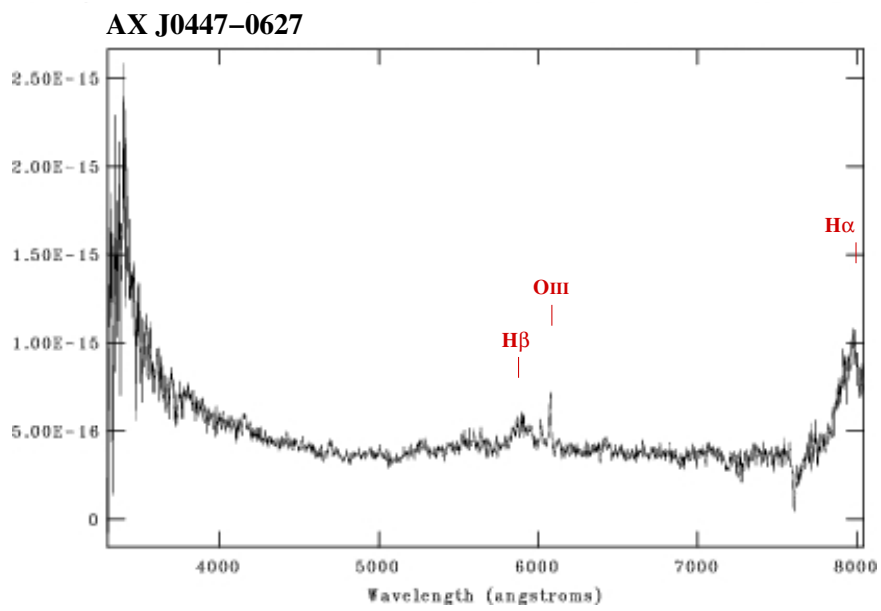

Figure II 14 Optical spectrum of AX J0447-0627 taken at the Telescopio Nazionale Galileo; the principal lines that allow to identify the source as a type 1 AGN are marked.

8000 Å (dispersion of 2.8 Å pixel^{-1}) and clearly shows broad (FWHM > 6000 km s^{-1}) MgII, Hβ, and Hα lines, as well as narrow (FWHM < 1000 km s^{-1}) [O III]$\lambda\lambda 4959, 5007$ Å lines. The optical line properties and position allow us to classify AX J0447-0627 as a classical broad-line AGN at $z = 0.214 \pm 0.001$. AX J0447-0627 also belongs to the *ASCA* Medium Sensitivity Survey, so an independent confirmation of the redshift and the optical spectral classification comes from the work presented in Akiyama et al. (2003).

Thus, the discrepancy between optical classification and hardness ratios derived from the *ASCA* observations suggests that gas absorption and dust obscuration could be different in the source. The X-ray spectral analysis allows to solve the (apparent) mismatch raised by the optical spectroscopy. To perform the analysis, source counts were extracted from a circular region of radius $22.5''$ for the MOS and $17.5''$ for the pn (this smaller radius for the pn is due to the proximity of a CCD gap). Background counts were extracted from a nearby source-free circular region of $\sim 42'' - 50''$ radius; Fig. II 15 shows these regions for the pn. The net count rates ($0.5 - 10$ keV energy range) are 0.051 ± 0.002, 0.054 ± 0.002, and 0.171 ± 0.004 counts s^{-1} for MOS1, MOS2, and pn, respectively; the source counts represents about 85% of the total counts in the source extraction region. We detected no statistically significant source variability during the XMM-*Newton* observation. To improve statistics, we combined together the MOS1 and MOS2 data, and the MOS and pn spectra

were fitted simultaneously, keeping the relative normalization free. Source counts were binned so as to have at least 20 counts in each energy bin. We have also generated our own spectral response matrices at the source position using the SAS tasks `arfgen` and `rmfgen`. All the models discussed here have been filtered through the Galactic absorption column density along the line of sight ($N_{\rm H,\ Gal}= 5.6 \times 10^{20}$ cm^{-2}; Dickey & Lockman 1990). Unless otherwise stated, fit parameters are quoted in the rest-frame of AX J0447-0627, while the figures are in the observer frame.

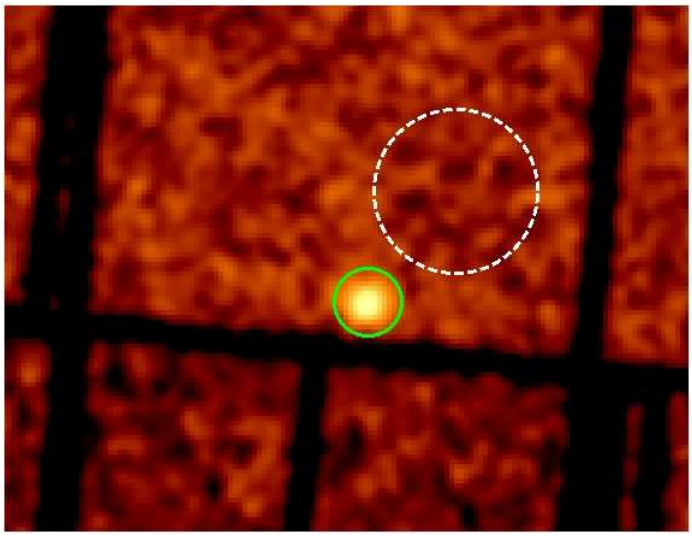

Figure II 15 XMM-*Newton* EPIC-pn $2-10$ keV image; the circles mark the regions considered for the extraction of the source (green continuous line) and background (white dashed line) counts.

II 3.2 Resolving the mismatch between absorption and obscuration

A single absorbed power law model is not a good description of the overall ($0.5-10$ keV) spectrum of AX J0447-0627 ($\Gamma = 2.18 \pm 0.05$; $N_{\rm H}$ consistent with zero; $\chi^2/{\rm dof} = 280.3/250$), since a very large discrepancy is present above 4 keV.

In Fig. II 16, *upper panel*, we show the ratio between the best fit power law model (obtained considering only the line-free region from ~ 0.8 to ~ 3 keV) and the data in the $2-10$ keV energy range. The residuals show the presence of a possible "line like" feature at $E \sim 3.5$ keV (observer frame) and a complex structure (several different lines?) in the energy range between ~ 4.5 and ~ 7 keV (observer frame). Splitting the total observation into two intervals of similar exposure times, we do not find convincing evidence of temporal variability of such structures (see Fig. II 16, *lower panel*).

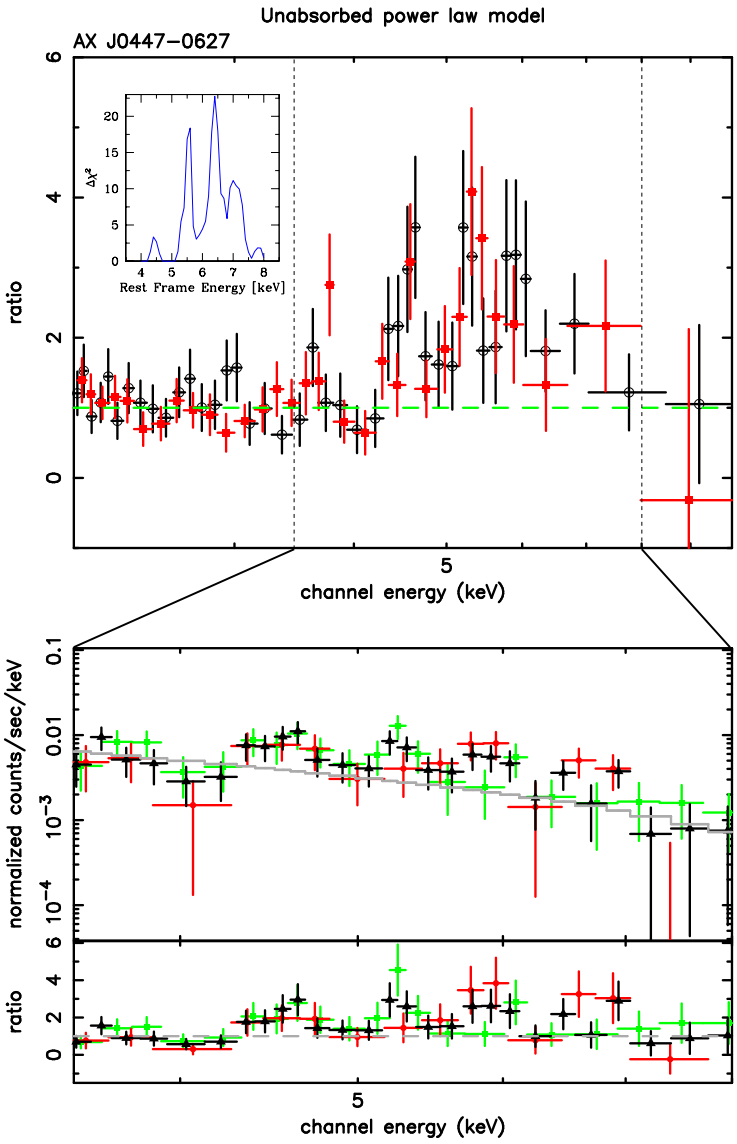

Figure II 16 *Upper panel:* ratio between the $2-10$ keV MOS (*filled squares*) and pn (*open circles*) data and the best-fit power law model (limited to the $\sim 0.8-3$ keV energy range: $\Gamma = 2.24^{+0.21}_{-0.08}$). In the inset we report the change in fit statistic ($\Delta\chi^2$) as a function of the centroid energy position of a narrow Gaussian line model that was stepped across the data; the comparison model is the underlying power-law continuum. *Lower panel:* fit of a simple power law model to the whole observation (black triangles), compared with that to the spectra obtained for two intervals of similar exposure times (9900 s, green squares; 7800 s, red circles), and ratio between data and best fit model; the complex of features around 5 keV appears steady in time.

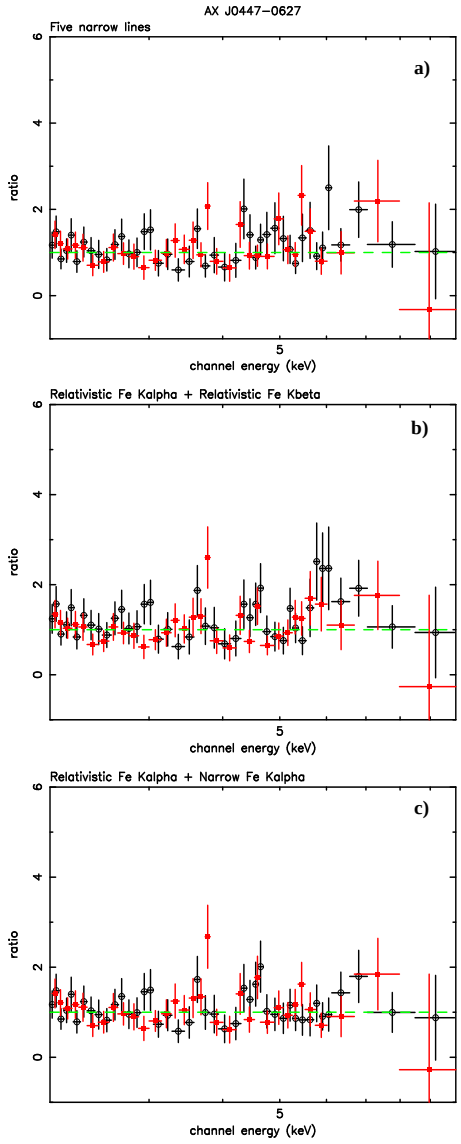

Figure II 17 *(a)*: Ratio between the $2-10$ keV MOS (*filled squares*) and pn (*open circles*) data and the best-fit spectral model composed of a power law ($\Gamma = 2.24^{+0.06}_{-0.05}$) plus five Gaussian lines as detailed in Table II 2. *(b)*: Ratio between the data and the best-fit spectral model composed of the REFSCH model (an e-folded power-law primary spectrum plus its reflected component from a ionized relativistic accretion disk) plus relativistic Fe Kα and Fe Kβ lines, as detailed in Table II 3. *(c)*: Ratio between the data and the best-fit spectral model composed of the REFSCH model plus a narrow Fe Kα line from neutral material and a broad Fe relativistic line from a ionized accretion disk, as detailed in Table II 3.

This complex of lines could have several origins.

Reflection - The data exclude that the origin of the emission is a pure reflection from circumnuclear material, either normal (PEXRAV model[9] in XSPEC; see Magdziarz & Zdziarski 1995) or relativistic (REFSCH model[10]; see Magdziarz & Zdziarski 1995; Fabian, Rees, Stella & White 1989). A pure reflected continuum with associated emission lines from Ca, Cr, Fe, and Ni (see, *e.g.*, the modeling of the Seyfert 2 galaxy NGC 6552 by Reynolds et al. 1994) is also unable to reproduce the observed structure since the relative abundances of the above elements differ from the expected ones. We also note that a pure reflected continuum, more typical of optical type 2 AGNs, is at odds with the optical spectral classification of AX J0447-0627.

Narrow gaussian line(s) - To investigate the presence of line-like features and locate their energy centroid we slid a narrow ($\sigma = 0.1$ keV) Gaussian template across the data between 4 and 8 keV (rest frame), looking for an improvement to the fit with respect to the simple power law model. The results are shown in the inset of Fig. II 16, *upper panel*, where we report the change in fit statistics ($\Delta\chi^2$) as a function of the centroid energy position of the narrow Gaussian line. This analysis points out the presence of a number of possible narrow lines, with rest-frame energy centroids at about 4.5, 5.6, 6.4, 7.0, and 7.9 keV (in the last case, the line centroid is not well constrained). Note that the lines at energies ~ 4.5 and at ~ 7.9 keV are of lower statistical significance with respect to those at ~ 5.6, ~ 6.4 and ~ 7.0 keV. Following these indications, we tried to reproduce the observed spectrum with a power law and five narrow Gaussian lines. The best-fit spectral parameters are reported in Table II 2, while the ratio between the data and this possible best fit-model is shown in Fig. II 17*a*.

– The line at $6.39^{+0.07}_{-0.06}$ keV (equivalent width ~ 700 eV) is positionally consistent with the Fe Kα emission line, while the line at $7.02^{+0.29}_{-0.12}$ keV (equivalent width $\sim$ 600 eV) is positionally consistent with both the Fe Kβ emission line (rest-frame energy $E = 7.058$ keV) and the Fe XXVI Lyα emission line (rest-frame energy $E = 6.96$ keV). However, the association with the Fe Kβ line is unlikely, since the measured equivalent width would imply a flux from this line higher than expected (the flux from Fe Kβ line being at a fixed ratio of ~ 0.11 with the Fe Kα

[9]Exponentially cut off power law spectrum reflected from neutral material.

[10]This model is the sum of an e-folded power-law primary spectrum plus its reflected component from a ionized relativistic accretion disk.

Table II 2. Best-Fit Spectral Analysis ($0.5 - 10.0$ keV in the Observed Frame) Parameters: Power Law plus Five Narrow Gaussian Lines.

Power Law		Lines			
Γ	Norm	$E_{\rm rf}$	Norm	EW	χ^2/dof
...	...	(keV)	...	(eV)	...
(1)	(2)	(3)	(4)	(5)	(6)
$2.24^{+0.06}_{-0.05}$	$2.38^{+0.13}_{-0.06}$	$4.49^{+0.13}_{-0.17}$	$0.92^{+0.71}_{u}$	93^{+72}_{u}	226.3/240
		$5.55^{+0.06}_{-0.05}$	$2.68^{+0.94}_{-1.01}$	436^{+152}_{-164}	
		$6.39^{+0.07}_{-0.06}$	$3.13^{+0.82}_{-1.26}$	700^{+182}_{-290}	
		$7.02^{+0.29}_{-0.12}$	$2.18^{+0.91}_{-1.08}$	602^{+251}_{-299}	
		$7.85^{+0.73}_{-0.76}$	$0.74^{+0.94}_{u}$	263^{+331}_{u}	

Note. — Errors are quoted at the 90% confidence level for one parameter of interest ($\Delta\chi^2 = 2.71$); u: unconstrained parameter.
Col. (1): Power-law photon index.
Col. (2): Normalization of the power law in units of 10^{-4} photons keV^{-1} cm^{-2} s^{-1} at 1 keV.
Col. (3): Rest-frame energy centroid of the narrow Gaussian line.
Col. (4): Normalization in units of 10^{-6} photons $^{-1}$ cm^{-2} s^{-1} in the line.
Col. (5): Equivalent width of the line.
Col. (6): χ^2 and number of degrees of freedom.

emission flux). The association with Fe XXVI Lyα seems to be more plausible given that this line could be very prominent (and sometimes with an equivalent width comparable with the narrow Fe Kα line) in type 1 AGN (see, *e.g.*, the case of the Seyfert 1 galaxy NGC 7314 discussed in Yaqoob et al. 2003).

– The line at $7.85^{+0.73}_{-0.76}$ keV is positionally consistent with the Ni Kα, while for the remaining two lines ($E = 4.49^{+0.13}_{-0.17}$ and $5.55^{+0.06}_{-0.05}$ keV) there are no clear associations with well-known and expected elements. The strongest expected lines in the spallation model are the Cr Kα at 5.4 keV and the Mn Kα at 5.9 keV (Skibo 1997). Both these lines are ruled out by the mismatch with the measured energy lines centroid. So unless an energy shift occurs (but we do not observe any energy shift for the Fe Kα line), the spallation model is an unlikely explanation

of the XMM-*Newton* data.

– We have also evaluated the upper limits for Fe XXV($\tilde{f}$) at $E \sim 6.64$ keV and Fe XXVI($\tilde{r}$) at $E \sim 6.70$ keV, since the strength of these lines, when combined with the strength of other ionized Fe lines, can constrain emission models (cf. Yaqoob & Padmanabhan 2004 and reference therein). These two lines are not required by the current data set and the 90% upper limit on their equivalent width is ~ 400 eV.

Accretion disk - The complex structure detected in the spectrum of AX J0447-0627 could suggest a profile of a Fe line produced by an accretion disk. We explored this interesting possibility using the DISKLINE model (Fabian, Rees, Stella & White 1989), which assumes a non rotating Schwarzschild black hole.[11] The relativistic effects have also been introduced in the description of the reflected continuum, replacing the simple power law model with the XSPEC model REFSCH.

– We started the analysis using a model composed by the REFSCH model plus a Fe Kα disk line, fixing its energy position to 6.4 keV rest frame; since in AX J0447-0627 the observed lines seems to have a significantly larger equivalent width than usual, we have also added the corresponding Fe Kβ disk-line emission, fixing the Fe Kβ/Fe Kα ratio to that expected form the theory (~ 0.11). The best-fit spectral parameters are reported in Table II 3 while the ratio between the data and the best fit model is shown in Fig. II 17*b*. Although the overall fit is statistically acceptable ($\chi^2_\nu = 1.00$), the ratio in Fig. II 17*b* shows a line like residual at an observed energy of ~ 6 keV (~ 7.3 keV rest frame) that we were unable to reduce. We tried to consider disk lines also associated with Ni Kα at ~ 7.5 keV or Fe XXVI Lyα at ~ 6.96 keV emission, and/or allowed the abundance of Fe Kβ, Ni Kα and Fe XXVI Lyα to be a free parameter of the fit, but we were unable to take into account such a line like structure.

– Thus, we tried the same model first used by Weaver et al. (1997) to describe the spectral properties of MCG -5-23-16: a narrow Fe Kα component ($E_{\rm line}$

[11] We have also tried the LAOR model (Laor 1991), in which the black hole is maximally rotating, but because of the limited source count statistics we could not discriminate between the DISKLINE and LAOR models. Since the black hole spin parameter is clearly an over parameterization of the present data set, we report here only the results obtained applying the DISKLINE model. We note, however, that similar results have been obtained using the LAOR model.

fixed at 6.4 keV) plus a broad relativistic line component (DISKLINE model) along with the underlying continuum (REFSCH model). The best-fit spectral parameters are reported in Table II 3, the ratio between the data and the best-fit model is shown in Fig. II 17*c*, while the folded model and the model itself are reported in Fig. II 18. The observed line position ($E = 6.61 \pm 0.11$ keV) of the broad relativistic line is inconsistent with the Fe Kα from neutral material but strongly suggests that it is due to Fe Kα emission from ionized He-like material. Overall, this modeling provide a good description of the broad band spectral properties of AX J0447-0627. We have also tried to add a relativistic emission line from Fe XXVI Lyα to the best-fit model reported in Table II 3; such a line can be accommodated within the present data set (with an equivalent width of ~ 15 eV) but it is not statistically required. The observed flux and the intrinsic luminosity in the $0.5-10$ keV energy range are $(6.5 \pm 0.4) \times 10^{-13}$ ergs cm^{-2} s^{-1} and $(8.9 \pm 0.5) \times 10^{43}$ ergs s^{-1}, the errors reflecting the uncertainties on the best-fit model. We note that the $2-10$ keV flux measured with XMM-*Newton* ($\sim 3.6 \times 10^{-13}$ ergs cm^{-2} s^{-1}) is in very good agreement with the $2-10$ keV flux measured with *ASCA*, thus excluding flux variability on years time scales.

II 3.3 Discussion

In Sect. II 3.2 we have shown that the complex, bright, and prominent set of lines in the $4.5-8.0$ keV energy range (rest frame) revealed in the XMM-*Newton* spectrum of the optically type 1 AGN AX J0447-0627 can be reasonably well reproduced by a physical model comprising a power law, a reflected relativistic continuum, a narrow Fe Kα line from neutral material, and a Fe He-like Kα relativistic line from a ionized accretion disk. Although not well constrained, the best-fit ionization parameter (ξ in Table II 3) is consistent with the Fe ionization state, as deduced from the best-fit line position (cf. Matt, Fabian & Ross 1993). A similar modeling of the Fe line properties (a narrow plus a broad relativistic component) has been found to describe, for example, the spectral properties of the Seyfert 1.9 MCG-5-23-16 (Weaver et al. 1997), the radio-quiet quasar Mrk 205 (Reeves et al. 2001), and of the Seyfert 1 NGC 3516 (Turner et al. 2002); the presence of the Fe relativistic line from a highly ionized accretion disk has been unambiguously reported in the case of Mrk 205. As already discussed by the aforementioned authors, the most likely origin of the narrow 6.4 keV component is from neutral matter distant from the black hole (*e.g.*, the putative

Table II 3. Results of the Spectral Analysis ($0.5 - 10.0$ keV in the Observed Frame) - REFSCH model + Fe Kα Relativistic Line + Fe (Relativistic or Gaussian) Line.

REFSCH [a]								DISKLINE			
								DISKLINE or GAUSSIAN			
Γ	i	$R_{\rm in}$	$R_{\rm out}$	ξ	R	Norm		$E_{\rm rf}$	Norm	EW [b]	χ^2/dof
...	(deg)	...	...	...	...	...	...	(keV)	...	(keV)	...
(1)	(2)	(3)	(4)	(5)	(6)	(7)		(8)	(9)	(10)	(11)
$2.26^{+0.04}_{-0.07}$	$25.0^{+4.4}_{-3.0}$c	$16.2^{u}_{-3.9}$d	$25.2^{+13.5}_{u}$d	1 f	$0.44 - 2.00$	1.55 ± 0.05		6.4 f	$5.3^{+1.6}_{-1.2}$c	$1.3^{+0.4}_{-0.3}$	235.94/246
Relativistic Fe Kβ:								7.06 f	$0.6^{+0.2}_{-0.1}$c	$0.18^{+0.05}_{-0.04}$	
$2.21^{+0.09}_{-0.15}$	$45.1^{+6.8}_{-7.4}$c	$19.5^{u}_{-6.0}$d	$29.5^{+102.1}_{u}$	$576.4^{+956.6}_{u}$c	$1.00^{+1.00}_{-0.95}$	$1.53^{+0.06}_{-0.09}$		$6.61^{+0.11}_{-0.12}$c	$6.2^{+2.1}_{-2.5}$	$1.4^{+0.7}_{-0.4}$	223.2/243
Narrow Fe Kα:								6.4 f	$1.7^{+1.1}_{-1.0}$	$0.4^{+0.2}_{-0.2}$	

Note. — Errors are quoted at the 90% confidence level for one parameter of interest ($\Delta\chi^2 = 2.71$). During the fit, the disk parameters of the different components were tied together; f: fixed parameter; u: unconstrained parameter.

Col. (1): Power-law photon index.

Col. (2): Inclination angle.

Col. (3): Inner disk radius in units of GM/c^2.

Col. (4): Outer disk radius in units of GM/c^2.

Col. (5): Disk ionization parameter in units of erg cm s^{-1}.

Col. (6): Reflection scaling factor.

Col. (7): Photon flux at 1 keV of the cutoff broken power law only (no reflection) in the observed frame in units of 10^{-4} photons keV^{-1} cm^{-2} s^{-1}.

Col. (8): Rest-frame energy centroid of the line.

Col. (9): Normalization in units of 10^{-6} photons cm^{-2} s^{-1} in the line.

Col. (10): Equivalent width of the line.

Col. (11): χ^2 and number of degrees of freedom.

[a]The following parameters have been fixed during all the fits: cutoff energy $E_{\rm c}$= 100 keV; disk temperature $T = 3 \times 10^4$ K; power-law index for reflection emissivity $\beta = -3$.

[b]Equivalent widths are computed with respect to the REFSCH underlying continuum.

[c]Errors were calculated by fixing at the best-fit values $R_{\rm in}$ and $R_{\rm out}$ (inclination of the accretion disk and relativistic line energy); $R_{\rm in}$, $R_{\rm out}$, and Γ (relativistic line normalization); R and Gaussian line normalization (disk ionization parameter).

[d]Errors have been evaluated performing a fit while stepping the value of $R_{\rm in}$ ($R_{\rm out}$) through the range $6.0 - 25.0$ ($20.0 - 200.0$).

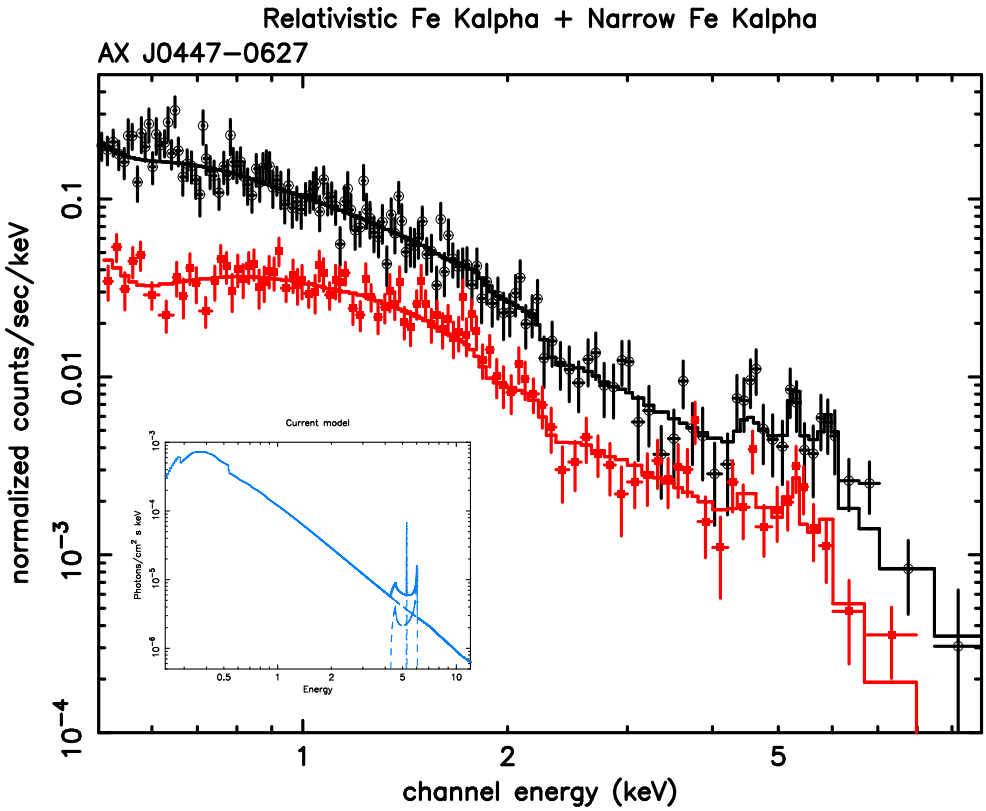

Figure II 18 MOS (*filled squares*) and pn (*open circles*) folded spectra fitted with the REFSCH model plus a narrow Fe Kα line from neutral material and a broad Fe relativistic line from a ionized accretion disk. In the inset we show the best-fit model, as detailed in Table II 3.

molecular torus).

The resulting best fit of the relativistic double-horned profile implies an inclination of the accretion disk of $\sim 45°$, and also that the observed lines should be produced in a narrow region of the disk from $R_{\rm in}\sim 19\ GM/c^2$ to $R_{\rm out}\sim 30\ GM/c^2$. As, for example, in the case of ESO 198-G24 (Guainazzi 2003) and NAB 0205+024 (Gallo et al. 2004), a few alternative possibilities can be conjectured to explain why the inner radius is larger than the last stable orbit. The first possibility is that the disk is highly ionized in the inner part, so most of the Fe is completely stripped off and the production of the Fe lines is suppressed. Second, the accretion disk in AX J0447-0627 could be truncated at $10-15\ GM/c^2$ (see Müller & Camenzind 2004). Finally, the relativistic line can be produced by a localized hot spot on the accretion disk surface (*e.g.*, Dovčiak et al. 2004).

All the properties discussed above have also been observed in other AGNs and

seem to be in agreement with the expectation from accretion disk theory. However, in AX J0447-0627 there is an observed property which is very unusual and makes this object unique: the very large equivalent width observed, which is at least a factor of 5 greater than that usually measured in other type 1 AGNs (see, *e.g.*, Yaqoob & Padmanabhan 2004 and reference therein) or expected from an accretion disk around a Schwarzschild black hole (Matt et al. 1992; Matt, Fabian & Ross 1993). According to the modelling reported in Martocchia & Matt (1996) and Miniutti & Fabian (2004), a high equivalent width could be explained if the primary X-ray source (illuminating both the observer and the accretion disk) is located very close to a central and maximally rotating Kerr black hole. However, such a combination should also imply a very high value of the reflection parameter R and a reflection-dominated source, probably in disagreement with the best fit found here.

A way to solve part of these problems is to assume that the emission features appear much stronger than normal because the continuum is strongly absorbed. We have tested this possibility by adding a partial covering absorption model in front to the underlying continuum. Unless the primary AGN emission is heavily absorbed ($N_{\rm H} \sim 10^{25}$ cm^{-2}) and therefore has signatures falling outside the XMM-*Newton* bandpass (but this is clearly at odd with the optical spectral classification of AX J0447-0627), the best-fit absorbing $N_{\rm H}$ and covering fraction ($\sim 9 \times 10^{21}$ cm^{-2} and ~ 0.2, respectively) imply that absorption effects cannot take into account the strong emission features observed.

With this in mind, and with the caveat that the model proposed here could be not fully appropriate (*e.g.*, we have already pointed out that a phenomenological description of the data can also be obtained by a simple power law model plus five narrow Gaussian lines at rest-frame energies of $4.49^{+0.13}_{-0.17}$, $5.55^{+0.06}_{-0.05}$, $6.39^{+0.07}_{-0.06}$, $7.02^{+0.29}_{-0.12}$, and $7.85^{+0.73}_{-0.76}$ keV), we would like to note that the emission lines in AX J0447-0627 have a total equivalent width of ~ 2 keV. This is an observational result and, as such, is model-independent. These lines deserve further attention and a deeper investigation since any model proposed to describe the X-ray spectral properties of AX J0447-0627 should be able to explain their large equivalent width.

Part III

SUMMARY AND FUTURE PLANS

Observations carried out in the last years have lead to the discovery of supermassive black holes in the nuclei of galaxies at continuously increasing rate. These objects are found to be ubiquitous at the centers of spheroidal galactic structures (Kormendy & Richstone 1995; Richstone et al. 1998). The effects of active accretion on the black holes is an important, but poorly understood ingredient in galaxy evolution. The tight relations between the black hole mass and mass and luminosity of the surrounding spheroid or between the $M_{\rm BH}$ and the velocity dispersion observed in the local Universe (Magorrian et al. 1998; Ferrarese & Merritt 2000; Gebhardt et al. 2000; Merritt & Ferrarese 2001; Tremaine et al. 2002; McLure & Dunlop 2002; Marconi & Hunt 2003) are witnessing for us the strong interplay between galaxies and hosted black holes: the formation and evolution of the host galaxy spheroidal component must proceed in lockstep with the growth of the supermassive monster sitting at its centers (see Ferrarese & Ford 2005 and references therein).

Hence, these objects may be considered literally "black-box" devices where the history of the host galaxy is recorded. Reconstructing their evolutionary history can provide fundamental insight to understand the structure formation in the universe (Kauffmann & Haehnelt 2000; Monaco et al. 2000; Granato et al. 2001; Cattaneo et al. 2001; Cavaliere & Vittorini 2002; Menci et al. 2003, 2004; Granato et al. 2004; Cattaneo et al. 2005; Fontanot et al. 2006a). An important question that has to be addressed is when and how the central black holes were assembled. We expect a direct link between the AGN phenomenon and the supermassive black holes hosted in inactive bulges, grown through accretion during active phases. Indeed, the local mass density in these black holes is sufficient to justify the

powering of the total emission of the AGN population over cosmic time if the accreting material is assumed to radiate with an efficiency near the upper end of the plausible range (Yu & Tremaine 2002; Marconi et al. 2004).

Moreover, deep X-ray surveys have recently established that the AGNs population exhibits so-called *cosmic downsizing*: the space density of AGN with low X-ray luminosities peaks at lower redshift than that of AGN with high X-ray luminosities (Steffen et al. 2003; Ueda et al. 2003). These results indicate that a substantial amount of the total black hole growth has occured more recently than would have been deduced based on optical surveys of powerful quasars (Boyle et al. 2000; Fan et al. 2001). The degeneracy in the origin of this downsizing in luminosity (*i.e.*, a decrease of the accretion rate in Eddington units or in the characteristic mass-scale for the actively growing black holes) has not yet been broken.

Powerful quasars are observed up to very high redshifts and deep surveys allow to study their properties. AGN host galaxy studies have so far focused on relatively luminous QSOs and radio galaxies drawn from various catalogs. These hosts seem to be mostly large ellipticals with only passive evolution detectable up to $z = 1$ (*e.g.*, McLure et al. 2000).

On the other hand, not very much is known about the population of active galactic nuclei at intermediate redshift ($z \lesssim 1$). There is little, if any, observational material documenting the evolution of low–luminosity AGN hosts.

A number of issues is currently still without a convincing answer: are these sources the progeny of high redshift powerful quasars? What does happen to the emission properties of AGNs (and in particular to the accretion mechanism) as time goes by? Several models for the evolution of massive black holes and AGN populations (see, *e.g.*, Haehnelt & Rees 1993; Cattaneo et al. 1999; Haiman & Menou 2000; Kauffmann & Haehnelt 2000; Cavaliere & Vittorini 2000; Hatziminaoglou et al. 2001; Wyithe & Loeb 2003; Volonteri et al. 2003; Granato et al. 2004) have been able to match the AGN optical luminosity function in a large redshift range ($1 \lesssim z \lesssim 6$). At lower redshift ($z \lesssim 1$) some of these models underpredict the faint end of the optical luminosity function. Merloni et al. (2003) and Merloni (2004) have shown that low–redshift AGNs could accrete at low accretion rate and with low radiative efficiency; the assumption of efficient accretion, common to most models, could explain the underabundance of faint AGN. Assuming an evolution of the Eddington ratio as a function of the redshift, the agreement between the shape of the local massive black hole mass function with the mass function derived from a deconvolution of the AGN luminosity function is improved.

To gain insight into these issues, we investigated the properties (in particular the

luminosity of the spheroidal component) of the host galaxies of a sample of X-ray selected AGNs at redshift between 0.4 and 1 and we compared them with the nuclear luminosity; this work is extensively described in Part I. Accordingly to the result of deep X-ray surveys, this is the redshift domain of the major contributors to the cosmic XRB (*i.e.*, the redshift range in which a substantial amount of the total black hole growth has occurred). The imaging capability of *HST* and the large spectral coverage from B to z bands allowed for an accurate separation of the bulge and nuclear luminosity for the 34 objects in our sample. The bolometric luminosity has been computed for each AGN linking with standard templates the intrinsic X-ray luminosity and the nuclear luminosity in the UV and optical bands. We estimated the central black hole mass from the bulge luminosity, under the assumption that their relationship observed in the local Universe is already in place since $z \sim 1$ (see, *e.g.*, Hopkins et al. 2006b and discussion in Sect. I 4.1).

We do not find any significant correlation of X-ray luminosities with either black hole masses or Eddington ratios. As expected, this X-ray selected sample is characterized by a high ratio of X-ray–to–optical nuclear luminosity with respect to the values found for optically selected AGNs: $\langle \alpha_{\rm ox} \rangle \sim -1.1$; we confirm the increase of this ratio with decreasing UV luminosity down to $L_{2500\,\text{Å}} \sim 10^{27}$ ergs s^{-1} Hz^{-1} (Strateva et al. 2005). By comparing the X-ray bolometric corrections in our low–luminosity AGNs with that of bright QSOs, we obtain a trend of decreasing of $k_{\rm X}$ with the luminosity. The bolometric output of these AGNs is rather low, and they are accreting at rather low Eddington ratios λ, about a factor 10 below the values found at higher redshift and luminosity. A comparison with higher luminosity samples suggests that the scatter in Eddington ratios is increasing with decreasing luminosity; this is a consequence of the expected increased probability of low Eddington ratios with decreasing bolometric luminosity. The estimated black hole masses span a wide range of values, $10^6 \lesssim M_{\rm BH} \lesssim 3 \times 10^8\ M_\odot$. Our results strongly suggest that most of the low–luminosity X-ray selected AGNs at $z \lesssim 1$ are powered by rather massive black holes, experiencing a low level accretion in a gas-poor environment.

This could be indicative that the phase of accumulation of the mass in less massive black holes occurred at high redshift ($z > 1$) and that in the sampled redshift range they also are accreting at low rate, and/or that the number density of black holes with $M_{\rm BH} \leq 10^6\ M_\odot$ is low. Another possibility is that at these redshifts they are growing at high Eddington ratios, but with a $M_{\rm BH}$ still very low; in this case the threshold $L_{2\text{-}8\,\rm keV} > 10^{42}$ ergs s^{-1} (imposed to pick out *bona fide* AGNs) prevents us from selecting these sources. In this sense the next natural step is expand the sample in order to study in detail how the black holes

powering low luminosity AGNs populate the $M_{\rm BH}$–λ plan.

This successfully tested approach could be used to investigate the properties of the AGN host galaxies extending at both lower and higher redshifts ($0.2 \lesssim z \lesssim 1.2$), as well as with a lower X-ray luminosity threshold ($L_{\rm 2\text{-}8\,keV} > 10^{41}$ ergs s^{-1}).

– Wider samples allow us to handle a more significant statistics, picking out even rare kinds of AGNs.

– Deeper samples allow us to select "slices" in the past, at increasing redshift ranges, thus investigating also the time evolution of the nuclear activity in comparison with the evolution of the host galaxies.

The availability of a growing number of multiwavelength surveys (from IR to X-ray, coupled with accurate, high S/N optical data) aimed to particular sky regions offers a unique opportunity to gather high quality data on carefully chosen targets. In particular, the ideal target to apply the capabilities of the method extensively tested in the present work is the E-CDF-S: as discussed Sect. 3.2, for this field the scientific community will have optical and near-IR imaging, as well as spectroscopic informations, coupled with full *Chandra* and *Spitzer* coverage, deep XMM-*Newton* pointings and an overlapping with GEMS (Rix et al. 2004) and COMBO-17 (Wolf et al. 2001) wide field coverage. It is worth noting that the *HST* images available thanks to the GEMS program are in two filters, F555W and F850LP, that are among the most efficient for ACS, and are excellent to perform this kind of morphological analysis, since the three model components (bulge, disk and nucleus) have different weight in these bands.

Moreover, the simultaneous availability of hard X-ray data of very good spatial (*Chandra*) and spectral (XMM-*Newton*) resolutions, coupled with the IR information (the best approach to identify AGNs embedded by a dusty torus), will allow to distinguish real AGNs from starburst–dominated galaxies (this is required in order to relax the X-ray luminosity threshold imposed in the present work) and to examine the nuclear properties also in connection with obscuration occuring in the nuclear region.

Finally, another logical step would be to increase the spectroscopic coverage in order to be able to exploit also the virial theorem to estimate the black hole mass. Under the assumption of isotropy for the BLR (and denoting their velocity and size with $v_{\rm BLR}$ and $R_{\rm BLR}$ respectively), the virial theorem reads $M_{\rm BH} \propto R_{\rm BLR} v^2_{\rm BLR}$ $[M_\odot]$. The velocity could be inferred from the width of the broad line in the optical spectra, while the size of the BLR

has been observed to correlate with the continuum luminosity (see, *e.g.*, Kaspi et al. 2000; Peterson et al. 2000; Vestergaard 2002). The technical feasibility of performing velocity dispersion estimates in these objects as well as of using [O III]$\lambda\lambda$5007, 4959 Å narrow lines of AGNs instead of the velocity dispersion (see, *e.g.*, Nelson 2000) must be evaluated.

The derivation of black hole masses, bolometric luminosities and Eddington ratios for a large sample of objects in several redshift bins could provide observational suitable data to put strong constraints to evolutionary models. Among the questions we could address are, a better understanding of the duty cycle of the quasars (*i.e.*, fraction of active black holes to their total number), and the distinct behaviour of supermassive black holes in the near and far Universe; related to this topic, why and how the luminous AGNs switched off. The small number of low mass black holes, $M_{\rm BH} \leq 10^6\ M_{\odot}$, if confirmed and statistically quantified, will be extremely informative on AGN formation and evolution, and on their demography.

In Part II we focused on two individual objects, selected to gain more hints on the topic outlined in the previous part: re-ignition, connection with star formation and nuclear obscuration. We explored the capability of specific X-ray observations to reach inside the most internal regions of AGNs. In both the analysed sources, these observations provided new important results, but at the same time they raised new questions that need to be addressed.

Hard X-ray observations with high resolution provide a completely new vision of Arp 299, a powerful IR system composed by two galaxies, NGC 3690 and IC 694, in a merging phase. Unlike the results obtained in all others energy bands, *Beppo*SAX first and then *Chandra* and XMM-*Newton* clearly revealed the presence of an obscured powerful AGN in the system, identifying the galaxy hosting the active nucleus (NGC 3690). At the same time, the analysis of the XMM-*Newton* data revealed a strong He-like Fe Kα line emission also in IC 694. The quality of the present data was insufficient to clarify whether this feature has a thermal origin or if it is indicative of the presence of a second AGN. In both cases the physical situation of Arp 299 is extremely peculiar, as discussed in detail in Sect. II 2.

In order to establish the AGN activity in Arp 299, hard ($>$ 10 keV) X-ray observations with angular resolution sufficient to disentangle the X-ray emission from the two galaxies would be needed. This goal will be feasible in the next years, with the planned launch of two new X-ray satellites, *Constellation-X* and *XEUS* (see below). Their technical characteristics will make these observatories ideal for getting to the bottom of the problem,

and more in general for extending the studies on the interplay between AGN and starburst also in systems with not extremely large IR emission.

At the moment, such observations are rather far in the future; to solve this ambiguity we need longer and/or repeated X-ray observations, in order to study the variability of the observed flux: if found, this would be a clearcut support favouring an AGN emission component in IC 694. As a by-product, such observations would also improve our assessment of the line properties in both the spectra. For IC 694 a better definition of the line profile could help in distinguishing between emission due either to reflection from ionized slab or due to a high temperature thermal plasma. The feature observed in NGC 3690, even if clearly associated to the absorbed AGN, seems to be marginally broad. Part of this broadening could be due to the wings of a second line-like feature present at higher energies ($E \sim 7$ keV), difficult to identify with the present statistics. If real, this line could be associated with the diffuse component resolved by *Chandra* and related to the starburst located just north of the nucleus or due to scattered/reflection of the AGN by highly ionized gas. A clear assessment on the Fe line properties, in conjunction with its $2-10$ keV continuum, could be effectively used to investigate the torus geometry and the optical depth of the central AGN.

Anyway, the results presented here are an encouragement for carrying on the search for accretion activity in merging systems. Indeed, finding active (binary?) black holes in merging systems is of paramount importance for understanding the formation and evolution of AGNs and the formation of elliptical galaxies via mergers. The cases of Arp 299 and NGC 6240 (two powerful IR merging systems, each hosting two actives black holes; the *Chandra* observations revealing the binary black hole in NGC 6240 are reported in Komossa et al. 2003) emphasize once again the importance of X-ray observations.

The case of Arp 299 can be regarded as a clear piece of evidence supporting the evolutionary scenarios presenting merger events as trigger of both intense episodes of star formation and gas inflow towards the central regions (see the discussion in Sect. 2). A model as in Hopkins et al. (2006a) implies that a static geometry such as the torus model in the classical unified view (Antonucci 1993; see Sect. 1.1) could be substituted by a more evolving configuration, where the heavily obscured phase is just one period in the AGN lifetime. Hence, the search for buried AGNs is extremely important to validate (or disclaim) such a model. On the other hand, in the framework devised by Vittorini et al. (2005) and Hopkins et al. (2006a), as the Universe evolves the number of mergers of gas rich galaxies decreases, and the activity observed in more evolved, nearby objects

must be necessarily fueled through alternative mechanisms, maybe steady accretion at low Eddington ratios probably due to minor mergers, as we found out in the Part I. Hence, our deep investigation of Arp 299 provides the touchstone to compare nuclear activity in two different accretion regimes, a required step for any fruitful confrontation between theory and observations.

Recent works have suggested the L-band spectroscopy as a new way to study the nature of powerful IR galaxies. Imanishi & Dudley (2000) discussed the physics of the emission/absorption features in the $\sim 3-4$ μm interval, and showed that low–resolution spectra of the brightest ULIRGs provide efficient diagnostics in order to disentangle the AGN and starburst contributions to the observed emission. New two-dimensional diagnostic diagrams where starbursts and AGNs are completely separated have been tested (and their origin physically discussed) by Risaliti et al. (2006a); a successful result of this technique, the detection of the double AGN in NGC 6240, is reported by Risaliti et al. (2006b). These findings illustrate how the L-band and the hard X-ray range are the best spectral regions in order to investigate the origin of the energy in powerful IR sources, also in a merging phase. During the last phases of writing of this thesis, Imanishi & Nakanishi (2006) have presented their result on K-band and L-band spectroscopy of Arp 299. On the basis of these data, the authors confirmed the identification of NGC 3690 as host of the powerful absorbed AGN revealed by *Beppo*SAX; concerning IC 694, they found no explicit evidence for an AGN.

The second peculiar object studied in Part II is AX J0447-0627. The XMM-*Newton* observations of this source revealed the presence of a bright and prominent set of lines in the $4-8$ keV rest frame energy range. This result resolved the contrast between optical classification (AX J0447-0627 is a type 1 AGN) and hard X-ray colors, due to unresolved spectral features rather than to absorption effects. The present XMM-*Newton* data could be explained with a physical model comprising a power law continuum, a narrow Fe Kα line from neutral material and a He-like Fe Kα relativistic line from a ionized accretion disk, though we cannot exclude the possibility of two relativistic emission lines (Fe Kα and Fe Kβ) and no narrow component. From a statistical point of view a phenomenological model involving the presence of five narrow emission lines produced by a medium far from the central source was adequate to describe the X-ray spectrum of AX J0447-0627; however, for two of these emission lines there are no clear associations with well known and expected elements.

Similar modeling of the Fe line properties (a narrow plus a broad relativistic com-

ponent) have been already found in a (relatively small) number of type 1 AGNs and discussed in the literature. However, the very large total equivalent width ($\sim$ 2 keV) of the observed complex makes this object unique, being the type 1 AGN with the highest equivalent width found. This observed (model independent) property in AX J0447-0627 deserves further attention and must be explained by all physical model aiming to describe the X-ray spectral properties of this source.

The present XMM-*Newton* data quality (and duration) is insufficient to strongly constrain the state and dynamics of this source in terms of ionization state and localization of the region where these emission lines are produced. To clarify these points and to establish the cause of the observed large equivalent width (*i.e.*, a particularly low state of the source, with the direct continuum suppressed, or a peculiar geometrical effect), we obtained in the last Announcement of Opportunity of XMM-*Newton* a longer observation (75 ksec, planned for the end of August 2006). This deep exposure will allow a time resolved spectral analysis of these features on different timescales, both splitting the new observation, and comparing them with the old one. In turn, this will allow to investigate a possible response of the flux of the line complex with respect to the continuum level of the source. Assuming the possible model comprising both a relativistic and a narrow Fe emission line, a constancy in flux and energy of the narrow component would confirm the origin of this line in neutral matter distant from the black hole. This would allow to estimate the inclination of the accretion disk, the inner and outer radii of the emitting region and the ionization state, via a study of line profiles.

It is worth to recall that the observed *ASCA* hardness ratios were indicative of a hard, presumably obscured, X-ray source, while optical classification indicates an unobscured AGN. There have been many claims in recent years about a substantial fraction ($\sim$ 10%) of X-ray–absorbed, optically classified type 1 AGNs (based mainly on poor-quality X-ray data (see Willott et al. 2004). On the contrary, a number of these sources, thought to be X-ray–absorbed type 1 AGNs on the basis of their hardness ratios, could instead be X-ray unabsorbed AGNs with substantial and complex X-ray line emission (see also Maccacaro et al. 2004), possibly produced very near the black hole. In other words, this result provides a way to identify (*e.g.*, in large databases produced by estended survey) sources suitable for studying the physics of these central regions. This field of research will benefit in the next future of observations from two X-ray satellites with throughout and high energy resolution (see below).

Future X-ray missions In the next years the launch of two X-ray observatory of "new generation", Nasa's *Constellation-X* and ESA's *XEUS* is planned. The energy range and spatial resolution expected are $0.2-40$ keV and $6''$, and $0.05-30$ keV and $2''$, respectively. Both the observatories will provide a very powerful combination of large effective area and high spectral resolution. These characteristics make *Constellation-X* and *XEUS* ideal tools for detailed study of variability, as well as for spectroscopy of high redshift AGNs. The first will allow to perform studies of "reverberation mapping": an accurate determination of the delay between variation in the continuum and response from a Fe line from accretion disk could allow to measure the distance between the latter and the corona (*i.e.*, the regions where the two spectral components are produced). Moreover, detailed analysis of its profile will enable to estimate some fundamental parameters, such as the mass of the central black hole and its spin. High-quality data in the Fe line band with simultaneous hard X-ray observations of the Compton reflection continuum and good angular resolution, as will be provided by *Constellation-X* and *XEUS*, are a fundamental tool to identify deeply obscured sources, and to investigate their intrinsic properties.

Bibliography

Akiyama, M., Ueda, Y., Ohta, K., Takahashi, T., & Yamada, T. 2003, ApJS, 148, 275

Akiyama, M. 2005, ApJ, 629, 72

Alexander, D. M., et al. 2003, AJ, 126, 539

Alonso-Herrero, A., Rieke, G. H., Rieke, M. J., & Scoville, N. Z. 2000, ApJ, 532, 845

Antonucci, R. 1993, ARA&A, 31, 473

Anderson, S. F., & Margon, B. 1987, ApJ, 314, 111

Arnouts, S., et al. 2001, A&A, 379, 740

Ballantyne, D. R., Iwasawa, K., & Fabian, A. C. 2001, MNRAS, 323, 506

Ballo, L., Braito, V., Della Ceca, R., Maraschi, L., Tavecchio, F., & Dadina, M. 2004, ApJ, 600, 634

Barger, A. J., Cowie, L. L., Brandt, W. N., Capak, P., Garmire, G. P., Hornschemeier, A. E., Steffen, A. T., & Wehner, E. H. 2002, AJ, 124, 1839

Barger, A. J., et al. 2003, AJ, 126, 632

Barger, A. J., Cowie, L. L., Mushotzky, R. F., Yang, Y., Wang, W.-H., Steffen, A. T., & Capak, P. 2005, AJ, 129, 578

Bauer, F. E., Alexander, D. M., Brandt, W. N., Schneider, D. P., Treister, E., Hornschemeier, A. E., & Garmire, G. P. 2004, AJ, 128, 2048

Behar, E., Rasmussen, A. P., Griffiths, R. G., Dennerl, K., Audard, M., Aschenbach, B., & Brinkman, A. C. 2001, A&A, 365, L242

Bender, R., Burstein, D., & Faber, S. M. 1992, ApJ, 399, 462

Bergvall, N., Laurikainen, E., & Aalto, S. 2003, A&A, 405, 31

Bianchi, S., Matt, G., Balestra, I., Guainazzi, M., & Perola, G. C. 2004, A&A, 422, 65

Blandford, R. D., Netzer, H., Woltjer, L., Courvoisier, T. J.-L., & Mayor, M. 1990, Saas-Fee Advanced Course 20. Lecture Notes 1990. Swiss Society for Astrophysics and Astronomy, XII, 280 pp. 97 figs.. Springer-Verlag Berlin Heidelberg New York

Boyle, B. J., Shanks, T., Croom, S. M., Smith, R. J., Miller, L., Loaring, N., & Heymans, C. 2000, MNRAS, 317, 1014

Boldt, E. 1987, Phys. Rep., 146, 215

Brand, K., NDWFS, t., & XBoötes teams 2005, ArXiv Astrophysics e-prints, arXiv:astro-ph/0509479

Brandt, W. N., et al. 2001, AJ, 122, 2810

Brandt, W. N., & Hasinger, G. 2005, ARA&A, 43, 827

Brusa, M., et al. 2003, A&A, 409, 65

Brusa, M., et al. 2005, A&A, 432, 69

Byun, Y. I., & Freeman, K. C. 1995, ApJ, 448, 563

Cagnoni, I., Della Ceca, R., & Maccacaro, T. 1998, ApJ, 493, 54

Capak, P., et al. 2004, AJ, 127, 180

Cappi, M. et al. 1999, A&A, 350, 777

Cattaneo, A., Haehnelt, M. G., & Rees, M. J. 1999, MNRAS, 308, 77

Cattaneo, A. 2001, MNRAS, 324, 128

Cattaneo, A., Blaizot, J., Devriendt, J., & Guiderdoni, B. 2005, MNRAS, 364, 407

Cavaliere, A., & Vittorini, V. 2000, ApJ, 543, 599

Cavaliere, A., & Vittorini, V. 2002, ApJ, 570, 114

Charmandaris, V., Stacey, G. J., & Gull, G. 2002, ApJ, 571, 282

Chary, R., et al. 2006, in preparation

Christian, D. J., & Swank, J. H. 1997, ApJS, 109, 177

Cirasuolo, M., Celotti, A., Magliocchetti, M., & Danese, L. 2003, MNRAS, 346, 447

Citterio, O., Conti, G., Mattaini, E., Sacco, B., & Santambrogio, E. 1985, SPIE, 597, 102

Comastri, A., et al. 2002, ApJ, 571, 771

Comastri, A., Gilli, R., & Hasinger, G. 2006, ArXiv Astrophysics e-prints, arXiv:astro-ph/0604523

Combes, F. 2001, *Advanced Lectures on the Starburst-AGN*, ed. Itziar Aretxaga, Daniel Kunth, and Ral Mjica, p.223, ArXiv Astrophysics e-prints, arXiv:astro-ph/0010570

Condon, J. J. 1992, ARA&A, 30, 575

Coziol, R., Torres, C. A. O., Quast, G. R., Contini, T., & Davoust, E. 1998, ApJS, 119, 239.

Cristiani, S., & Vio, R. 1990, A&A, 227, 385

Cristiani, S., et al. 2004, ApJ, 600, L119

Dahlem, M., Parmar, A., Oosterbroek, T., Orr, A., Weaver, K. A., & Heckman, T. M. 2000, ApJ, 538, 555

Dahlem, M., Weaver, K. A., & Heckman, T. M. 1998, ApJS, 118, 401

Della Ceca, R., Castelli, G., Braito, V., Cagnoni, I., & Maccacaro, T. 1999, ApJ, 524, 674

Della Ceca, R., Braito, V., Cagnoni, I., & Maccacaro, T. 2001, Memorie della Societa Astronomica Italiana, 72, 841

Della Ceca, R. et al. 2002, ApJ, 581, L9

Della Ceca, R., Ballo, L., Braito, V., & Maccacaro, T. 2005, ApJ, 627, 706

De Luca, A., & Molendi, S. 2004, A&A, 419, 837

Dickey, J. M., & Lockman, F. J. 1990, ARA&A, 28, 215

Dickinson, M., Giavalisco, M., & The Goods Team 2003, The Mass of Galaxies at Low and High Redshift, 324

Dickinson, M., et al. 2006, in preparation

Di Matteo, T., Croft, R. A. C., Springel, V., & Hernquist, L. 2003, ApJ, 593, 56

Di Matteo, T., Springel, V., & Hernquist, L. 2005, Nature, 433, 604

Dovčiak, M., Bianchi, S., Guainazzi, M., Karas, V., & Matt, G. 2004, MNRAS, 350, 745

Ehle, M. et al. 2001,*XMM*-Newton*Users' Handbook* (`http://xmm.vilspa.esa.es/external/xmm_user_support/documentation/uhb_2.0/index.html`)

Elvis, M., Green, R. F., Bechtold, J., Schmidt, M., Neugebauer, G., Soifer, B. T., Matthews, K., & Fabbiano, G. 1986, ApJ, 310, 291

Elvis, M., et al. 1994, ApJS, 95, 1

Fabian, A. C., Rees, M. J., Stella, L., & White, N. E. 1989, MNRAS, 238, 729

Fabian, A. C., & Iwasawa, K. 1999, MNRAS, 303, L34

Fabian, A. C., Iwasawa, K., Reynolds, C. S., & Young, A. J. 2000, PASP, 112, 1145

Fabian, A. C. 2004, Coevolution of Black Holes and Galaxies, 447

Fan, X., et al. 2001, AJ, 121, 54

Fasano, G., Cristiani, S., Arnouts, S., & Filippi, M. 1998, AJ, 115, 1400

Fasano, G., Bettoni, D., D'Onofrio, M., Kjærgaard, P., & Moles, M. 2002, A&A, 387, 26

Ferrarese, L., & Merritt, D. 2000, ApJ, 539, L9

Ferrarese, L. 2002, ApJ, 578, 90

Ferrarese, L., & Ford, H. 2005, Space Science Reviews, 116, 523

Ferrarese, L., et al. 2006, ApJ, 644, L21

Fiore, F., Guainazzi, M., & Grandi, P. 1999, *Cookbook for* Beppo*SAX NFI Spectral Analysis* (`ftp://sax.sdc.asi.it/pub/sax/doc/software_docs/saxabc_v1.2.ps.gz`)

Fontanot, F., Monaco, P., Cristiani, S., & Tozzi, P. 2006, ArXiv Astrophysics e-prints, arXiv:astro-ph/0609823

Fontanot, F., et al. 2006, in preparation

Franceschini, A., et al. 2003, MNRAS, 343, 1181

Francis, P. J., Hewett, P. C., Foltz, C. B., Chaffee, F. H., Weymann, R. J., & Morris, S. L. 1991, ApJ, 373, 465

Francis, P. J., Hooper, E. J., & Impey, C. D. 1993, AJ, 106, 417

Gallo, L. C., Boller, T., Brandt, W. N., Fabian, A. C., & Vaughan, S. 2004, MNRAS, 355, 330

Gawiser, E., et al. 2006, ApJS, 162, 1

Gebhardt, K., et al. 2000, ApJ, 539, L13

Gehrz, R. D., Sramek, R. A., & Weedman, D. W. 1983, ApJ, 267, 551

George, I. M., & Fabian, A. C. 1991, MNRAS, 249, 352

Georgantopoulos, I., Zezas, A., & Ward, M. J. 2003, ApJ, 584, 129

Ghisellini, G., Haardt, F., & Matt, G. 1994, MNRAS, 267, 743

Giacconi, R., Gursky, H., Paolini, F. R., & Rossi, B. B. 1962, Phys. Rev. Lett., 9, 439

Giacconi, R., et al. 2002, ApJS, 139, 369

Giavalisco, M., et al. 2004, ApJ, 600, L93

Gilli, R., et al. 2003, ApJ, 592, 721

Gilli, R., et al. 2005, A&A, 430, 811

Graham, A. W., Erwin, P., Caon, N., & Trujillo, I. 2001, ApJ, 563, L11

Granato, G. L., Zitelli, V., Bonoli, F., Danese, L., Bonoli, C., & Delpino, F. 1993, ApJS, 89, 35

Granato, G. L., & Danese, L. 1994, MNRAS, 268, 235

Granato, G. L., Silva, L., Monaco, P., Panuzzo, P., Salucci, P., De Zotti, G., & Danese, L. 2001, MNRAS, 324, 757

Granato, G. L., De Zotti, G., Silva, L., Bressan, A., & Danese, L. 2004, ApJ, 600, 580

Grazian, A., et al. 2006, A&A, 449, 951

Grogin, N. A., et al. 2005, ApJ, 627, L97

Guainazzi, M., Matt, G., Brandt, W. N., Antonelli, L. A., Barr, P., & Bassani, L. 2000, A&A, 356, 463

Guainazzi, M. 2003, A&A, 401, 903

Haehnelt, M. G., & Rees, M. J. 1993, MNRAS, 263, 168

Haiman, Z., & Menou, K. 2000, ApJ, 531, 42

Hasinger, G., Burg, R., Giacconi, R., Schmidt, M., Trumper, J., & Zamorani, G. 1998, A&A, 329, 482

Hasinger, G., et al. 2001, A&A, 365, L45

Hatziminaoglou, E., Siemiginowska, A., & Elvis, M. 2001, ApJ, 547, 90

Häring, N., & Rix, H.-W. 2004, ApJ, 604, L89

Heckman, T. M., Armus, L., Weaver, K. A., & Wang, J. 1999, ApJ, 517, 130

Helou, G., Khan, I. R., Malek, L., & Boehmer, L. 1988, ApJS, 68, 151

Hibbard, J. E., & Yun, M. S. 1999, AJ, 118, 162

Holt, S. S., Neff, S. G., & Urry, C. M. 1992, American Institute of Physics Conference Series, 254,

Hopkins, P. F., Hernquist, L., Cox, T. J., Di Matteo, T., Martini, P., Robertson, B., & Springel, V. 2005, ApJ, 630, 705

Hopkins, P.E., Hernquist, L., Cox, T.J., Di Matteo, T., Robertson, B., Springel, V. 2006a, ApJS, 163, 1

Hopkins, P. F., Robertson, B., Krause, E., Hernquist, L., & Cox, T. J. 2006b, ArXiv Astrophysics e-prints, arXiv:astro-ph/0608091

Imanishi, M., & Dudley, C. C. 2000, ApJ, 545, 701

Imanishi, M., & Nakanishi, K. 2006, ArXiv Astrophysics e-prints, arXiv:astro-ph/0608309

Ishisaki, Y., Ueda, Y., Yamashita, A., Ohashi, T., Lehmann, I., & Hasinger, G. 2001, PASJ, 53, 445

Jogee, S. 2004, in AGN Physics on All Scales, LNP Volume, eds. D. Alloin, R. Johnson & P. Lira (Springer: Berlin), Ch.6, in press, ArXiv Astrophysics e-prints, arXiv:astro-ph/0408383

Kaastra, J. S., & Mewe, R. 1993, A&AS, 97, 443

Kaspi, S., Smith, P. S., Netzer, H., Maoz, D., Jannuzi, B. T., & Giveon, U. 2000, ApJ, 533, 631

Kauffmann, G., & Haehnelt, M. 2000, MNRAS, 311, 576

Keel, W. C. 1983, ApJ, 269, 466

Kellermann, K. I., Sramek, R., Schmidt, M., Shaffer, D. B., & Green, R. 1989, AJ, 98, 1195

Kollmeier, J. A., et al. 2006, ApJ, in press, ArXiv Astrophysics e-prints, arXiv:astro-ph/0508657

Komossa, S., Burwitz, V., Hasinger, G., Predehl, P., Kaastra, J. S., & Ikebe, Y. 2003, ApJ, 582, L15

Kormendy, J., & Richstone, D. 1995, ARA&A, 33, 581

Kormendy, J., & Gebhardt, K. 2001, AIP Conf. Proc. 586: 20th Texas Symposium on relativistic astrophysics, 586, 363

Kuraszkiewicz, J. K., et al. 2003, ApJ, 590, 128

Laor, A. 1991, ApJ, 376, 90

Laurent, O., Mirabel, I. F., Charmandaris, V., Gallais, P., Madden, S. C., Sauvage, M., Vigroux, L., & Cesarsky, C. 2000, A&A, 359, 887

Lawrence, C. R., Zucker, J. R., Readhead, A. C. S., Unwin, S. C., Pearson, T. J., & Xu, W. 1996, ApJS, 107, 541

Leahy, D. A., & Creighton, J. 1993, MNRAS, 263, 314

Lehmer, B. D., et al. 2005, ApJS, 161, 21

Levenson, N. A., Weaver, K. A., & Heckman, T. M. 2001a, ApJS, 133, 269

Levenson, N. A., Weaver, K. A., & Heckman, T. M. 2001b, ApJ, 550, 230

Liedahl, D. A., Osterheld, A. L., & Goldstein, W. H. 1995, ApJ, 438, L115

Lynden-Bell, D. 1969, Nature, 223, 690

Maccacaro, T., Braito, V., Della Ceca, R., Severgnini, P., & Caccianiga, A. 2004, ApJ, 617, L33

McKernan, B., & Yaqoob, T. 2004, ApJ, 608, 157

McLure, R. J., Dunlop, J. S., & Kukula, M. J. 2000, MNRAS, 318, 693

McLure, R. J., & Dunlop, J. S. 2002, MNRAS, 331, 795

McLure, R. J., & Dunlop, J. S. 2004, MNRAS, 352, 1390

Magdziarz, P., & Zdziarski, A. A. 1995, MNRAS, 273, 837

Magorrian, J., et al. 1998, AJ, 115, 2285

Mainieri, V., et al. 2005, A&A, 437, 805

Maraschi, L., & Tavecchio, F. 2003, ApJ, 593, 667

Maraschi, L., & Tavecchio, F. 2005, Growing Black Holes: Accretion in a Cosmological Context, 377

Marconi, A., & Hunt, L. K. 2003, ApJ, 589, L21

Marconi, A., Risaliti, G., Gilli, R., Hunt, L. K., Maiolino, R., & Salvati, M. 2004, MNRAS, 351, 169

Marshall, F. E., Boldt, E. A., Holt, S. S., Miller, R. B., Mushotzky, R. F., Rose, L. A., Rothschild, R. E., & Serlemitsos, P. J. 1980, ApJ, 235, 4

Martocchia, A., & Matt, G. 1996, MNRAS, 282, L53

Mather, J. C., et al. 1994, ApJ, 420, 439

Mathur, S., & Grupe, D. 2004, IAU Symposium, 222, 501

Matt, G., Perola, G. C., & Piro, L. 1991, A&A, 247, 25

Matt, G., Perola, G. C., Piro, L., & Stella, L. 1992, A&A, 263, 453

Matt, G., Fabian, A. C., & Ross, R. R. 1993, MNRAS, 262, 179

Matt, G., Brandt, W. N., & Fabian, A. C. 1996, MNRAS, 280, 823

Matt, G., Fabian, A. C., Guainazzi, M., Iwasawa, K., Bassani, L., & Malaguti, G. 2000, MNRAS, 318, 173

Menci, N., Cavaliere, A., Fontana, A., Giallongo, E., Poli, F., & Vittorini, V. 2003, ApJ, 587, L63

Menci, N., Fiore, F., Perola, G. C., & Cavaliere, A. 2004, ApJ, 606, 58

Merloni, A., Heinz, S., & di Matteo, T. 2003, MNRAS, 345, 1057

Merloni, A. 2004, MNRAS, 353, 1035

Merloni, A., Rudnick, G., & Di Matteo, T. 2004, MNRAS, 354, L37

Merritt, D., & Ferrarese, L. 2001, MNRAS, 320, L30

Mewe, R., Gronenschild, E. H. B. M., & van den Oord, G. H. J. 1985, A&AS, 62, 197

Mewe, R., Lemen, J. R., & van den Oord, G. H. J. 1986, A&AS, 65, 511

Miller, L., Turner, T. J., Reeves, J. N., George, I. M., Porquet, D., Nandra, K., & Dovciak, M. 2006, A&A, 453, L13

Miniutti, G., & Fabian, A. C. 2004, MNRAS, 349, 1435

Mohan, N. R., Anantharamaiah, K. R., & Goss, W. M. 2002, ApJ, 574, 701

Monaco, P., Salucci, P., & Danese, L. 2000, MNRAS, 311, 279

Monaco, P., & Fontanot, F. 2005, MNRAS, 359, 283

Moran, E. C., Lehnert, M. D., & Helfand, D. J. 1999, ApJ, 526, 649

Moshir, M. et al. 1990, IRAS Faint Source Catalogue, version 2.0 (1990)

Moy, E., Barmby, P., Rigopoulou, D., Huang, J.-S., Willner, S. P., & Fazio, G. G. 2003, A&A, 403, 493

Müller, A., & Camenzind, M. 2004, A&A, 413, 861

Nandra, K., George, I. M., Mushotzky, R. F., Turner, T. J., & Yaqoob, T. 1997, ApJ, 477, 602

Nelson, C. H. 2000, ApJ, 544, L91

Netzer, H. 1990, Saas-Fee Advanced Course 20. Lecture Notes 1990. Swiss Society for Astrophysics and Astronomy, XII, 280 pp. 57 figs.. Springer-Verlag Berlin Heidelberg New York

O'Dowd, M., Urry, C. M., & Scarpa, R. 2002, ApJ, 580, 96

Peng, C. Y., Ho, L. C., Impey, C. D., & Rix, H. 2002, AJ, 124, 266

Peng, C. Y., Impey, C. D., Ho, L. C., Barton, E. J., & Rix, H.-W. 2006, ApJ, 640, 114

Persic, M., et al. 1998, A&A, 339, L33

Persic, M., & Rephaeli, Y. 2002, A&A, 382, 843

Peterson, B. M. 1997, *An introduction to active galactic nuclei*, Publisher: Cambridge, New York Cambridge University Press, 1997 Physical description xvi, 238 p. ISBN 0521473489

Peterson, B. M., et al. 2000, ApJ, 542, 161

Pietsch, W., et al. 2001, A&A, 365, L174

Porquet, D., Reeves, J. N., Uttley, P., & Turner, T. J. 2004, A&A, 427, 101

Press, W. H., Teukolsky, S. A., Vetterling, W. T., & Flannery, B. P. 1997, Numerical Recipes in C (Cambridge: Cambridge Univ. Press)

Rees, M. J. 1984, ARA&A, 22, 471

Rees, M. J., Phinney, E. S., Begelman, M. C., & Blandford, R. D. 1982, Nature, 295, 17

Reeves, J. N., Turner, M. J. L., Pounds, K. A., O'Brien, P. T., Boller, T., Ferrando, P., Kendziorra, E., & Vercellone, S. 2001, A&A, 365, L134

Rephaeli, Y., & Gruber, D. 2002, A&A, 389, 752

Reynolds, C. S., Fabian, A. C., Makishima, K., Fukazawa, Y., & Tamura, T. 1994, MNRAS, 268, L55

Reynolds, C. S. 1996, *X-ray Emission and Absorption in Active Galaxies*, PhD thesis, University of Cambridge (`http://www.astro.umd.edu/~chris/publications/thesis/thesis.html`)

Reynolds, C. S., & Nowak, M. A. 2003, Phys. Rep., 377, 389

Richstone, D., et al. 1998, Nature, 395, A14

Risaliti, G., & Elvis, M. 2004, ASSL Vol. 308: Supermassive Black Holes in the Distant Universe, 187

Risaliti, G., et al. 2006a, MNRAS, 365, 303

Risaliti, G., et al. 2006b, ApJ, 637, L17

Rix, H. -., Falco, E., Impey, C., Kochanek, C., Lehar, J., McLeod, B., Munoz, J., & Peng, C. 1999, ArXiv Astrophysics e-prints, arXiv:astro-ph/9910190

Rix, H.-W., et al. 2004, ApJS, 152, 163

Rosati, P., et al. 2002, ApJ, 566, 667

Ross, R. R., & Fabian, A. C. 1993, MNRAS, 261, 74

Ross, R. R., Fabian, A. C., & Young, A. J. 1999, MNRAS, 306, 461

Salucci, P., Szuszkiewicz, E., Monaco, P., & Danese, L. 1999, MNRAS, 307, 637

Sambruna, R. M., Maraschi, L., & Urry, C. M. 1996, ApJ, 463, 444

Sambruna, R. M., Gliozzi, M., Eracleous, M., Brandt, W. N., & Mushotzky, R. 2003, ApJ, 586, L37

Sanders, D. B., Phinney, E. S., Neugebauer, G., Soifer, B. T., & Matthews, K. 1989, ApJ, 347, 29

Setti, G., & Woltjer, L. 1989, A&A, 224, L21

Severgnini, P., et al. 2003, A&A, 406, 483

Shakura, N. I., & Sunyaev, R. A. 1973, A&A, 24, 337

Shankar, F., Salucci, P., Granato, G. L., De Zotti, G., & Danese, L. 2004, MNRAS, 354, 1020

Shankar, F., Salucci, P., Granato, G. L., de Zotti, G., & Danese, L. 2005, Growing Black Holes: Accretion in a Cosmological Context, 470

Shields, G. A., Gebhardt, K., Salviander, S., Wills, B. J., Xie, B., Brotherton, M. S., Yuan, J., & Dietrich, M. 2003, ApJ, 583, 124

Silk, J., & Rees, M. J. 1998, A&A, 331, L1

Silva, L., Granato, G. L., Bressan, A., & Danese, L. 1998, ApJ, 509, 103

Simard, L., et al. 2002, ApJS, 142, 1

Simmons, B., et al. 2006, in preparation

Skibo, J. G. 1997, ApJ, 478, 522

Steffen, A. T., Barger, A. J., Cowie, L. L., Mushotzky, R. F., & Yang, Y. 2003, ApJ, 596, L23

Stevens, I. R., Read, A. M., & Bravo-Guerrero, J. 2003, MNRAS, 343, L47

Strateva, I. V., Brandt, W. N., Schneider, D. P., Vanden Berk, D. G., & Vignali, C. 2005, AJ, 130, 387

Strickland, D. K., Heckman, T. M., Weaver, K. A., & Dahlem, M. 2000, AJ, 120, 2965

Szokoly, G. P., et al. 2004, ApJS, 155, 271

Tananbaum, H., Avni, Y., Green, R. F., Schmidt, M., & Zamorani, G. 1986, ApJ, 305, 57

Tozzi, P., and the CDF-S Team. 2001, Proc for "Where's the Matter?", eds. L. Tresse & M. Treyer, ArXiv Astrophysics e-prints, arXiv:astro-ph/0111036

Tozzi, P., et al. 2006, A&A, 451, 457

Tran, K.-V. H. 2000, GIM2D *Cookbook* (`http://www.hia-iha.nrc-cnrc.gc.ca/STAFF/lsd/gim2d/vycbook/gim2d-notes.ps`)

Tremaine, S., et al. 2002, ApJ, 574, 740

Turner, T. J., et al. 2002, ApJ, 574, L123

Turner, T. J., Kraemer, S. B., & Reeves, J. N. 2004, ApJ, 603, 62

Turner, T. J., Kraemer, S. B., George, I. M., Reeves, J. N., & Bottorff, M. C. 2004, ApJ, 618, 155.

Ueda, Y., et al. 1999, ApJ, 518, 656

Ueda, Y., et al. 1998, Nature, 391, 866

Ueda, Y., Akiyama, M., Ohta, K., & Miyaji, T. 2003, ApJ, 598, 886

Urry, C. M., & Padovani, P. 1995, PASP, 107, 803

Vandame, B., et al. 2001, A&A submitted, ArXiv Astrophysics e-prints, arXiv:astro-ph/0102300

Vanzella, E., et al. 2005, A&A, 434, 53

Vecchi, A., Molendi, S., Guainazzi, M., Fiore, F., & Parmar, A. N. 1999, A&A, 349, L73

Vestergaard, M. 2002, ApJ, 571, 733

Vestergaard, M. 2004, ApJ, 601, 676

Vestergaard, M., & Peterson, B. M. 2006, ApJ, 641, 689

Vignali, C., Brandt, W. N., & Schneider, D. P. 2003, AJ, 125, 433

Vignati, P. et al. 1999, A&A, 349, L57

Virani, S. N., De Robertis, M. M., & VanDalfsen, M. L. 2000, AJ, 120, 1739

Virani, S. N., Treister, E., Urry, C. M., & Gawiser, E. 2006, AJ, 131, 2373

Vittorini, V., Shankar, F., & Cavaliere, A. 2005, MNRAS, 363, 1376

Volonteri, M., Haardt, F., & Madau, P. 2003, ApJ, 582, 559

Volonteri, M., Salvaterra, R., & Haardt, F. 2006, ArXiv Astrophysics e-prints, arXiv:astro-ph/0606675

Wadadekar, Y., Robbason, B., & Kembhavi, A. 1999, AJ, 117, 1219

Warner, C., Hamann, F., & Dietrich, M. 2004, ApJ, 608, 136

Waskett, T. J., Eales, S. A., Gear, W. K., McCracken, H. J., Lilly, S., & Brodwin, M. 2005, MNRAS, 363, 801

Weaver, K. A., Yaqoob, T., Mushotzky, R. F., Nousek, J., Hayashi, I., & Koyama, K. 1997, ApJ, 474, 675

Weaver, K. A., Heckman, T. M., & Dahlem, M. 2000, ApJ, 534, 684

Weaver, K. A., Heckman, T. M., Strickland, D. K., & Dahlem, M. 2002, ApJ, 576, L19

Weisskopf, M. C., Brinkman, B., Canizares, C., Garmire, G., Murray, S., & Van Speybroeck, L. P. 2002, PASP, 114, 1

White, N. E., Swank, J. H., & Holt, S. S. 1983, ApJ, 270, 711

Willott, C. J., et al. 2004, ApJ, 610, 140

Wolf, C., Meisenheimer, K., Röser, H.-J. 2001, A&A, 365, 660

Woo, J.-H., & Urry, C. M. 2002, ApJ, 579, 530

Woo, J.-H., Urry, C. M., Lira, P., van der Marel, R. P., & Maza, J. 2004, ApJ, 617, 903

Woo, J.-H., Treu, T., Malkan, M. A., & Blandford, R. D. 2006, ApJ, 645, 900

Worsley, M. A., et al. 2005, MNRAS, 357, 1281

Wright, E. L., et al. 1994, ApJ, 420, 450

Wyithe, J. S. B., & Loeb, A. 2003, ApJ, 595, 614

Wynn-Williams, C. G., Hodapp, K.-W., Joseph, R. D., Eales, S. A., Becklin, E. E., McLean, I. S., Simons, D. A., & Wright, G. S. 1991, ApJ, 377, 426

Xilouris, E. M., & Papadakis, I. E. 2002, A&A, 387, 441

Yaqoob, T. 1997, ApJ, 479, 184

Yaqoob, T., George, I. M., Kallman, T. R., Padmanabhan, U., Weaver, K. A., & Turner, T. J. 2003, ApJ, 596, 85

Yaqoob, T., & Padmanabhan, U. 2004, ApJ, 604, 63

Yu, Q., & Tremaine, S. 2002, MNRAS, 335, 965

Zamorani, G., et al. 1981, ApJ, 245, 357

Zdziarski, A. A., Fabian, A. C., Nandra, K., Celotti, A., Rees, M. J., Done, C., Coppi, P. S., & Madejski, G. M. 1994, MNRAS, 269, L55

Zezas, A. L., Georgantopoulos, I., & Ward, M. J. 1998, MNRAS, 301, 915

Zezas, A., Fabbiano, G., Rots, A. H., & Murray, S. S. 2002, ApJS, 142, 239

Zezas, A., Ward, M. J., & Murray, S. S. 2003, ApJ, 594, L31

Zheng, W., et al. 2004, ApJS, 155, 73

Acronyms

ACS	Advanced Camera for Surveys
ACIS	Advanced CCD Imaging Spectrometer
AGN	Active Galactic Nucleus
ALMA	Atacama Large Millimeter Array
APM	Automatic Plate Measuring
ASCA	Advanced Satellite for Cosmology and Astrophysics
BL LAC	BL LACertae
BLR	Broad Line Region
BLRG	Broad Line Radio Galaxy
CCD	Charged Coupled Device
CDF-N	*Chandra* Deep Field North
CDF-S	*Chandra* Deep Field South
COBE	COsmic Background Explorer
COMBO-17	Classifying Objects by Medium-Band Observations
DOLORES	Device Optimized for the LOw RESolution
E-CDF-S	Extended *Chandra* Deep Field South
EIS	ESO Imaging Survey
ERO	Extremely Red Object
EPIC	European Photon Imaging Camera
FIR	Far InfraRed
FIRST	Faint Images of the Radio Sky at Twenty-centimeters
FRI	Faranoff Riley I
FRII	Faranoff Riley II
FSRQ	Flat Spectrum Radio Quasar
GEMS	Galaxy Evolution From Morphology And SEDs

GOODS	Great Observatories Origins Deep Survey
GMOS	Gemini Multi-Object Spectrograph
HDF-N	Hubble Deep Field North
HETG	High Energy Transmission Gratings
HEW	Half Energy Width
HMXB	High-Mass X-Ray Binary
HR	Hardness Ratio
HRC	High Resolution Camera
HRI	High Resolution Imager
HRMA	High Resolution Mirror Assembly
HST	Hubble Space Telescope
IMACS	Inamori Magellan Areal Camera and Spectrograph
IR	InfraRed
IRAC	InfraRed Array Camera
IRAS	InfraRed Astronomical Satellite
ISAAC	Infrared Spectrometer And Array Camera
LETG	Low Energy Transmission Gratings
MIPS	Multiband Imaging Photometer for *Spitzer*
MOS	Metal Oxide Semiconductor
MUSYC	MUltiwavelength Survey by Yale/Chile
NELG	Narrow Emission Line X-ray Galaxy
NICMOS	Near Infrared Camera and Multi-Object Spectrometer
NIR	Near InfraRed
NLR	Narrow Line Region
NLRG	Narrow Line Radio Galaxy
NTT	New Technology Telescope
PG QSO	Palomar Green Quasi-Stellar Object
PSF	Point Spread Function
QUIRC	QUick InfRared Camera
QSO	Quasi-Stellar Object
RGS	Reflection Grating Spectrometers
ROSAT	RÖntengen SATellite
SAS	Science Analisys Software
SB	Surface Brightness

SDSS	Sloan Digital Sky Survey
SED	Spectral Energy Distribution
SNR	SuperNova Remnant
SOFI	Son OF Isaac
SSP	Single Stellar Population
SSRQ	Steep Spectrum Radio Quasar
Sy 1	Seyfert 1 galaxies
Sy 2	Seyfert 2 galaxies
ULIRG	Ultra Luminous InfraRed Galaxy
UV	UltraViolet
VIMOS	VIsible MultiObject Spectrograph
VLT	Very Large Telescope
WFI	Wide Field Imager
WFPC2	Wide Field Planetary Camera 2
XBONG	X-ray Bright Optically Inactive Galaxies
XEUS	X-ray Evolving Universe Spectrometer
XIS	X-ray Imaging Spectrometer
XMM-*Newton*	X-ray Multi-mirror Mission
XRB	X-ray Background